SLOVAK UNIVERSITY OF TECHNOLOGY IN BRATISLAVA
Faculty of Electrical Engineering and Information Technology

Reg. No.: FEI-104354-70029

Development of a methodology and platform for the measurement of low-frequency magnetic field biological effects

Dissertation Thesis

Study program Measurement Technology
Field of study: Electrical and Electronics Engineering
Training workplace: Institute of Measurement Science of the Slovak Academy of Science
Supervisor: Mgr. Michal Teplan, PhD.
Consultant: Ing. Ľubomír Kremnický, PhD.

2025 **Ing. Hoang Vu Viet**

Vyhradená strana

pre

VLOŽENIE ZADANIE

ANNOTATION

SLOVAK UNIVERSITY OF TECHNOLOGY IN BRATISLAVA
Faculty of Electrical Engineering and Information Technology
Institute of Electrical Engineering

Study Curriculum:	**Measurement Technology**
Author:	**Hoang Vu Viet**
Title of dissertation thesis:	**Development of a methodology and platform for the measurement of low-frequency magnetic field biological effects**
Supervisor:	Mgr. Michal Teplan, PhD.
Consultant:	Ing. Ľubomír Kremnický, PhD.
Year of the submission:	September 2025

The dissertation aims to broaden knowledge about the impact of weak external low-frequency electromagnetic fields on the functioning of selected biological objects that could be the basis for novel diagnostic and therapeutic methods for the treatment of civilization diseases.

The primary aim of this work is to finalize a new experimental platform and procedures enabling efficient scanning of the electromagnetic field parameters which lead to specific biological responses. Part of the dissertation will include the design and implementation of hardware and software interfaces as well as control of individual modules of the experimental platform enabling the quantitative characterization of the biological response of the cells. The scientific problems within the dissertation will be concentrated on the development of impedance measurement methods used for the characterization of living cells and the dynamics of cell growth.

Keywords: Magnetic Field, Biological Respond, Cell Growth, Cell Concentration

Affidavit

I hereby declare that I have authored this thesis independently, that I have not used other than the declared sources and resources, and that I have explicitly indicated all material that has been quoted either literally or by content from the sources used.

.....

Signature

in Bratislava, ...

List of Symbols

Symbol	Unit	Description
B	H	Magnetic Flux Density
C	F	Capacitance
C_m	F	Membrane Capacitance
d	m	The thickness of the Shell
E_2	-	Biomass Estimator
f	Hz	Frequency
f_c	Hz	Characteristic Frequency
G_m	S	Membrane Conductance
I	A	Current
N_c	-	Cell Concentration
P	-	Volume fraction
R	Ω	Resistance
r	m	The radius of the Shell-sphere
t	s	Time
U_i	V	Induced Electromotive Voltage
V	V	Voltage
Z	Ω	Impedance
Z_0	Ω	Low-Frequency Impedance
Z_∞	Ω	High-Frequency Impedance
α	-	Dispersion of the Cell Sizes and Shapes
ε	F/m	Relative Permittivity
ε_0	$8.85\ 10^{-12}$ F/m	Permittivity of Vacuum
ε_h	F/m	Relative Permittivity at High-frequency limit

κ	S/m	Relative Conductivity
κ_l	S/m	Relative Conductivity at Low-frequency limit
ε_a, κ_a	F/m, S/m	Relative Permittivity and Conductivity of the Medium
ε_i, κ_i	F/m, S/m	Relative Permittivity and Conductivity to the Cytoplasm
ε_m, κ_m	F/m, S/m	Relative Permittivity and Conductivity to the Membrane
σ_e	S/m	Extracellular Conductivity
σ_i	S/m	Intracellular Conductivity
ϕ	Wb	Magnetic Flux

List of Abbreviations

AO	Acridine Orange
BAL	Biological Autoluminescence
C	Counter
CHO	Chinese Hamster Ovary
EMF	Electromagnetic Field
DNA	Deoxyribonucleic acid
DCR	Direct Current Resistance
HeLa	Immortalized Cell Line named after Henrietta Lacks
HF	High Frequency or High-frequency
HIV	Human immunodeficiency viruses
IPR	Ion Parametric Resonance
LF	Low Frequency or Low-frequency
Log	Logarithmic
MF	Magnetic Field
PBMC	Peripheral Blood Mononuclear Cell
PCR	Polymerase Chain Reaction
PD	Photodiodes
PEF	Pulse Electric Field
PI	Propidium Iodide
PID	Proportional-Integral-Derivative
PMT	Photomultiplier Tubes
R	Reference
RNA	Ribonucleic acid
RPM	Revolution per minute
SAL	Sterility Assurance Level
SD	Standard Deviation
RSD	Relative Standard Deviation
THP-1	Human Monocytic Cell Line
UV	Ultraviolet
W	Work
WS	Working Sense
YPD	Yeast Extract Peptone Dextrose

Contents

List of Symbols 5
List of Abbreviations 7
Contents 8
1 Introduction 10
2 Previous Research 13
3 Biological and Physical Properties of Cells 18
3.1 Cell Cycle 18
3.2 Cell Growth Curve 19
3.3 Biological Model 20
3.4 Effects of Electromagnetic Field on Biological Structures 21
4 Cell Concentration Counting Methods 24
4.1 Hemocytometer 24
4.2 Turbidimetry 26
4.3 Flow Cytometry ..... **Error! Bookmark not defined.**
4.4 Image Analysis ..... **Error! Bookmark not defined.**
4.5 Electrical Impedance 26
5 Development of Measurement Platform 31
5.1 The Experimental Workflow 31
5.2 Helmholtz Coils 32
5.3 System for Magnetic Field Generation 37
5.4 Homogeneity of Magnetic Field 40
5.5 Temperature Regulation in Cultivation Chamber 43
5.6 In-situ Temperature Monitoring of Samples 46
5.7 Completed Experimental Platform 48
6 Cell Concentration Monitoring Based on Impedance Spectroscopy 50
6.1 Interference of Mechanical Vibration with Impedance Measurement 54
6.2 Improvement of the Measurement Conditions Using Bioreactor 55
6.3 Challenges in Impedance-Based Real-Time Concentration Monitoring 59
7 Static Cultivation with Turbidimetry-Based Concentration Measurement 65
7.1 Optimal Starting Microbial Concentration 66
7.2 Modelling of Optimal Duration of Biological Experiment 67
7.3 Verifying Pair Experimental Design 70
8 Effect of 50 Hz Magnetic Field on Saccharomyces Cerevisiae Growth 75
9 Pulsed Electric Field Effect on Yeast Cells Measured by Autoluminescence and Impedance Measurements 83
10 Conclusions and Main Contributions 90
Author's Publications 93

References 96
Appendix A - Experimental procedure..... 102
Appendix B - Impedance Spectroscopy Analyzer..... 105
Appendix C - Helmholtz Coil's Parameters 108
Appendix E – Supplement Figures..... 110
Appendix F – Supplement Programing Codes 112

1 Introduction

Low-frequency magnetic fields (LF MFs), typically in the range of Hz to kHz, are ubiquitous in modern environments due to power lines, household appliances, and industrial equipment. The biological effects of these anthropogenic fields—especially at network frequencies of 50 Hz and 60 Hz—have attracted considerable scientific interest. Although numerous studies suggest that LF MFs can elicit biological effects, the mechanisms of interaction and their implications for human health and biotechnology remain poorly understood.

A wide range of studies report both beneficial and detrimental effects of LF MF exposure. Biological responses span diverse domains, including ion channel activity, cytoskeletal dynamics, gene expression, protein synthesis, cellular signaling pathways [1], and reactive oxygen species (ROS) production. Experimental findings suggest that LF MFs may influence cell proliferation [2]–[6], affect gene expression [7], and modulate oxidative stress [8]. Several studies indicated the potential connection between LF MFs exposure and cancer [9], [10], or cardiovascular diseases [11]. Some of these effects have been explored for their therapeutic potential in regenerative medicine [12], wound healing [13], cancer therapy [14], cardiovascular modulation [15], neuroprotection [16], even tumor inhibition [17], and tumor-specific frequencies with anti-proliferative effects was also introduced [18]. At the same time, epidemiological studies have reported associations between LF MF exposure and increased risks of childhood leukemia [19], neurodegenerative diseases [20], [21], and disruptions to reproductive and cardiovascular system [22]. The coexistence of beneficial and harmful effects underlines the need for systematic and well-controlled research. In addition to biomedical effects, the potential of LF MFs to improve microbial and plant biotechnological processes has also been explored, which would contribute to advances in food production, medicine, and environmental sustainability [23], [24].

Cellular-level studies further indicate varied effects across different systems. For example, decreased proliferation was seen in human dermal fibroblasts [4], whereas enhanced growth and S-phase progression were noted in human epidermal stem cells [3]. Studies using *Saccharomyces cerevisiae* also revealed inhibitory effects on viability [25]. In contrast, other reports suggest protective effects against cell death [8], or selective inhibition in cancer cell lines [14]. The diversity of responses indicates a high dependence on cell type, field parameters, and environmental conditions. At the physiological level, the nervous

system appears particularly susceptible to LF MFs, with some reports of altered brain activity, cognition, and behavior [16], although results remain inconsistent. Adey's study opens a question whether biological systems can exhibit resonances during interaction with external electromagnetic fields, and whether the concept of Adey's frequency and amplitude windows accurately describes their selective responses [26]. Physical mechanisms of biological LF MF interaction, such as ion cyclotron resonance [27], ion parametric resonance (IPR) [28], [29], or radical pair mechanism were also proposed [30], [31], [32]. Their experimental verification is still largely absent, due to the fact, that most experimental studies focus only on a small set of frequencies [33], [34].

Despite the breadth of findings, many studies suffer from methodological limitations. Inconsistencies between experimental setups, lack of temperature control, insufficient shielding from background magnetic noise, and poorly characterized exposure systems all reduce reproducibility and credibility [35], [36]. The 2020 ICNIRP report and follow-up studies [37]–[39] have called for more rigorous and standardized experimental frameworks to resolve these issues.

Our group has contributed to addressing these gaps by developing novel measurement and evaluation techniques. We previously demonstrated that LF MF exposure alters biological autoluminescence (BAL), indicating a potential impact on cellular redox processes [40]. However, the BAL system lacked capability to track growth dynamics, leading to the introduction of impedance spectroscopy for real-time cell concentration monitoring [41]. We also developed automated microscopic image analysis methods for quantifying yeast populations [42] and used BAL to monitor membrane electroporation dynamics under pulsed electric field exposure [43].

Based on these insights and limitations observed in the literature particularly the insufficient treatment of thermal control in 50/60 Hz MF studies [2]–[4], [8], [14], [25], [45] this thesis focuses on developing a robust experimental platform with precise environmental control and standardized biological assessment.

In this work, we present a newly developed and validated platform capable of generating well-defined low-frequency magnetic fields and enabling real-time monitoring of biological responses. Special emphasis was placed on temperature stability, magnetic field homogeneity, parallel test-control configurations, and reproducible cultivation conditions. This platform was used to evaluate the effects of LF MFs on the growth of *Saccharomyces*

cerevisiae, a model organism for cell biology and biotechnology research. The experimental design ensures improved accuracy, reproducibility, and interpretability of results, aiming to contribute toward resolving the current uncertainties in the field and enabling applications in both fundamental science and biotechnology.

2 Previous Research

The influence of LF MFs on biological systems remains an active area of research with both promising applications and unresolved controversies. Numerous in vitro studies have explored how magnetic field parameters such as frequency, flux density, and exposure duration affect various cellular outcomes [46]. Tab. 1 summarizes nine representative studies investigating the impact of LF MF exposure on different cell types, ranging from *Saccharomyces cerevisiae* to human dermal fibroblasts, microglial cells, and several cancer and stem cell lines. The experimental protocols and outcomes vary widely, with reported results including enhanced proliferation, apoptosis induction, DNA synthesis disruption, or complete absence of measurable effects. This variability underscores the complexity of LF MF interactions with cellular systems and highlights the importance of methodological rigor in the design of exposure experiments.

Notably, some studies report frequency or magnetic flux density dependent effects. Zhang et al. (2013) [3] observed enhanced proliferation in human epidermal stem cells at 50 Hz, while Radil et al. (2020) [48] reported frequency-dependent inhibition of *Saccharomyces cerevisiae* proliferation in the range of 0.4–1.6 kHz. Meanwhile, Song et al. (2018) [45] found that a 60 Hz, 6 mT field promoted proliferation in HeLa and fibroblast cells, attributing this to reduced reactive oxygen species. Conversely, Xu et al. (2020) [14] demonstrated that similar LF MF exposure triggered apoptosis in breast cancer cells while sparing non-cancerous lines. These opposing results raise the question of cell type specificity, exposure parameter tuning, and whether some cellular systems are more prone to LF MF influence than others.

However, deeper examination of experimental design (Tab. 2) reveals significant disparities in how environmental and exposure conditions were managed. Temperature control, in particular, emerges as a recurring methodological shortcoming. Only a few studies, Lee et al. (2015) [2], An et al. (2015) [44], and Pasi et al. (2016) [4] explicitly monitored and reported temperature during exposure, and even these lacked complete thermal profiles across both control and test groups. Most studies simply assumed incubator stability or relied on coarse temperature settings. Given that cellular processes are highly temperature-sensitive, even minor fluctuations could confound the biological effects attributed to LF MF exposure.

Another underutilized design element in these studies is rigorous exposure symmetry. Ideally, experiments should involve not only test versus control comparisons but also control/control (C/C) and test/test (T/T) replications to confirm baseline consistency and assess intrinsic variability. Yet, few studies incorporated such redundancy, and none applied a complete cross-over design, in which the exposure conditions are alternated between test and control groups. This omission is significant because cross-over designs enable direct comparison within the same system while accounting for spatial biases or coil asymmetries factors that may otherwise produce misleading biological differences.

Further emphasizing this gap is the absence of ΔT (T–C) data information about any temperature differential between test and control samples during exposure. As shown in Tab. 2, none of the reviewed experiments systematically measured or reported this parameter. ΔT tracking is essential for separating thermal from non-thermal magnetic field effects, particularly in long-term culture experiments where even minor deviations can lead to cumulative physiological differences. The combination of incomplete thermal control, lack of internal validation (via C/C or T/T comparisons), and the absence of cross-over studies indicate a widespread need for more stringent and transparent experimental protocols in LF MF research.

In summary, while many studies report intriguing biological effects of LF MFs, the existing literature suffers from significant methodological heterogeneity. Improvements in experimental standardization, especially in temperature monitoring, exposure symmetry, and control design are urgently needed to reach more definitive conclusions. Future work should integrate robust environmental controls and leverage real-time monitoring technologies to reduce confounding variability. Until then, the inconsistency across studies will likely persist, complicating efforts to determine whether LF MFs hold genuine biological relevance or therapeutic potential.

In response to these methodological gaps, our objective has been to develop a modular and well-controlled experimental platform that overcomes the limitations observed in prior studies. The platform includes precise temperature regulation using active thermal feedback and dual sensor monitoring for both test and control samples. Environmental stability is maintained not only within incubators but also across spatial compartments to reduce differential heating or electromagnetic interference. Moreover, the design supports parallel and interchangeable exposure channels, enabling flexible implementation of control/control

(C/C), test/test (T/T), and cross-over (T/C ↔ C/T) experiments. This feature ensures the elimination of systematic biases related to coil asymmetry or chamber placement. Such a system is intended to support high-quality, reproducible studies that provide clearer insight into the biological relevance of LF MF exposure and create a foundation for future investigations into therapeutic or biotechnological applications.

Tab. 1: Summary of experimental parameters and biological responses to LF MF exposure. This table compares LF MF exposure conditions across selected studies, including magnetic field frequency and intensity, exposure duration, biological models, temperature settings, measurement methods, and observed cellular responses. Results show a wide variability in both experimental design and biological outcomes, underscoring the complexity of LF MF interactions and the need for standardized protocols.

Reference	MF		Exposure duration	Biological Model	T [°C]	Measurement Method	Result
	Frequency [Hz]	Flux density [mT]					
Novak, 2006	60	10	60min	S. cerevisiae	24-26	optical density	inhibiting effects
Zhang, 2013	50	5	30m/d, 7d	hESC	37	flow cytometry	cells increased during the S phase
Lee, 20015	60	0.01~1	4h~16h	MCF10A,NIH3T3	20-30	hemocytometer	decreased viability, DNA synthesis
An, 2015	50	2.3	2h/d,5d/w	KYSE150, C6	37	hemocytometer	no change in cell morphology
Pasi, 2016	5&50	0.25~1.6	1.5h	fibroblasts	37	hemocytometer	no changes in cell viability
Duong, 2016	10/50/100	0.01~1	4h	HMO6	37	hemocytometer	cell death detected
Song, 2018	60	6	1h/d, 3d	HaCaT, PC12, NIH-3T3	37	flow cytometry	promoted cell proliferation
Xu, 2020	50-275	1	6h~36h	MCF-7, ZR-75-1, T47D	n/a	flow cytometry	inhibiting effects via apoptosis
Radil, 2020	0.4~1.6k	2.33~2.45	72h	S. cerevisiae	27	Petri- Counter	inhibiting effects

Tab. 2: Evaluation of experimental design quality and environmental control in LF-MF studies. This table analyses methodological rigor in selected LF-MF experiments based on criteria such as repetition, use of pair controls, temperature monitoring, and experimental symmetry. Key factors like ΔT (temperature difference between test and control), C/C and T/T pair experiment, and cross-over design are largely missing, indicating common limitations in reproducibility and environmental consistency.

Reference	Repetition Number	Pair Experiment	Climated Room	Temperature Monitoring	ΔT reported (T-C)	C/C; T/T tests	Cross-over design
Novak, 2006	10, 4	Yes, 2 different places, 1 coil	No	No, room temperature	No	No	No
Zhang, 2013	3-4	Yes, 2 incubators	No	Incubator set to 37.0 °C ± 0.5; no further monitoring	No	No	No
Lee, 20015	>=3	Yes	No	Yes; both T and C monitored and maintained at 37 ± 3 °C	No	No	No
An, 2015	>=3	Yes, 1 incubator	No	Incubator's temperature is monitored, but not temperature of both samples	No	No	No
Pasi, 2016	3	Yes, 2 different places, 1 coil	No	Yes; temperature stability kept within 1 °C; no further details	No	No	No
Duong, 2016	9.12	Yes, 1 incubator	No	No	No	No	No
Song, 2018	3	Yes, 1 coil	No	No	No	No	No
Xu, 2020	>=3	Yes, 2 incubator	No	No	No	No	No
Radil, 2020	>=3	Yes, 2 incubators, 2 coils	No	Yes; both incubators kept at 27 °C, confirmed by thermometer	No	No	No

3 Biological and Physical Properties of Cells

The cell is the basic structural and functional unit of life forms. Every cell consists of a cytoplasm enclosed within a membrane and contains many biomolecules such as proteins, Deoxyribonucleic acid (DNA), and Ribonucleic acid (RNA), as well as many small molecules of nutrients and metabolites.

3.1 Cell Cycle

The cell cycle, or cell-division cycle, is a series of events that take place in a cell that causes it to divide into two daughter cells. These events include the duplication of its Deoxyribonucleic acid (DNA) or its replication and some of its organelles, and subsequently the partitioning of its cytoplasm and other components into two daughter cells in a cell division process.

In cells with nuclei (eukaryotes, i.e., animal, plant, fungal, and protist cells), the cell cycle is divided into two main stages: interphase and the mitotic (M) phase (including mitosis and cytokinesis). During interphase, the cell grows, accumulating nutrients needed for mitosis, and replicating its DNA and some of its organelles. During the mitotic phase, the replicated chromosomes, organelles, and cytoplasm separate into two new daughter cells. To ensure the proper replication of cellular components and division, there are control mechanisms known as cell cycle checkpoints after each of the key steps of the cycle that determine if the cell can progress to the next phase [49].

In cells without nuclei (prokaryotes, i.e., bacteria and archaea), the cell cycle is divided into the B, C, and D periods. The B period extends from the end of cell division to the beginning of DNA replication. DNA replication occurs during the C period. The D period refers to the stage between the end of DNA replication and the splitting of the bacterial cell into two daughter cells.

As in **Error! Reference source not found.** and Tab. 3, the eukaryotic cell cycle consists of four distinct phases: G1 phase, S phase (synthesis), G2 phase (collectively known as interphase), and M phase (mitosis and cytokinesis). M phase is composed of two tightly coupled processes: mitosis, in which the cell's nucleus divides, and cytokinesis, in which the cell's cytoplasm divides forming two daughter cells. Activation of each phase is dependent

on the proper progression and completion of the previous one. Cells that have temporarily or reversibly stopped dividing are said to have entered a state of quiescence called G0 phase.

After cell division, each of the daughter cells begins the interphase of a new cycle. Although the various stages of interphase are not usually morphologically distinguishable, each phase of the cell cycle has a distinct set of specialized biochemical processes that prepare the cell for the initiation of cell division.

Tab. 3: States and Phases of a Eukaryotic Cell Cycle

State	Phase	Abbreviation	Description
Resting	Gap 0	G0	The phase where the cell has left the cycle and has stopped dividing.
Interphase	Gap 1	G1	Cell growth. The G1 checkpoint ensures that everything is ready for DNA synthesis.
	Synthesis	S	DNA replication.
	Gap 2	G2	Growth and preparation for mitosis. The G2 checkpoint ensures that everything is ready to enter the M (mitosis) phase and divide.
Cell division	Mitosis	M	Cell division occurs. The Metaphase Checkpoint ensures that the cell is ready to complete cell division.

3.2 Cell Growth Curve

It is important to know and record the growth characteristics of the cell line in use before planning any experiments including cell viability and proliferation rates. An alteration in cellular growth can indicate a significant problem within the cell line and if undetected, can have detrimental effects on experimental results [51].

A typical growth curve for cultured cells displays a sigmoid pattern of proliferation. The growth phases associated with normal cells are defined in (Fig. 1):

1. Lag Phase – at this stage the cells do not divide. During this period the cells adapt to the culture conditions, and the length of this phase will depend upon

the growth phase of the cell line at the time of subculture and the seeding density.

2. Logarithmic Growth Phase – cells actively proliferate and an exponential increase in cell density arises. The cell population is considered to be the most viable at this phase; therefore, it is recommended to assess cellular function at this stage. Each cell line will show different cell proliferation kinetics during the log phase, and it is therefore the optimal phase for determining the population doubling time. Cells are also generally dying at the late log phase. Cells dying too late can lead to overcrowding, apoptosis, and senescence.

3. Plateau (or Stationary) Phase – cellular proliferation slows down due to the cell population becoming confluent. At this stage the number of cells in the active cell cycle drops to 0-10% and the cells are most susceptible to injury.

4. Decline Phase – cell death predominates in this phase and there is a reduction in the number of viable cells. Cell death is not due to the reduction in nutrients but to the natural progression of the cellular cycle.

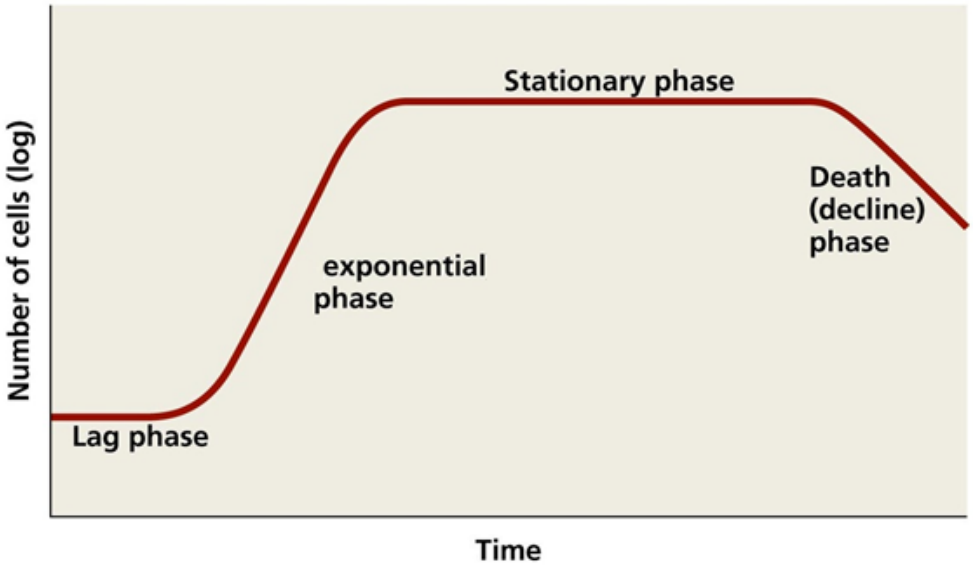

Fig. 1: Typical yeast growth curve. *Saccharomyces cerevisiae* growth at 30°C [51].

3.3 Biological Model

Yeasts *Saccharomyces cerevisiae* is one of the most studied eukaryotic model organisms in molecular and cellular biology [52]. They have several outstanding properties which predestine them for biomedical applications. They involve:

1. Yeasts are simple eukaryotic cells, the closest to complex mammalian cells.
2. Their metabolic pathways are a milestone in biology.
3. Their waste output is CO_2.
4. They need only a simple cultural medium
   (pure water and nutrients such as sugar).

Due to their relative simplicity and ease of manipulation, they are widely used to elucidate fundamental aspects of cellular processes, such as cell signalling, cell cycle, and metabolism, as well as to study some human diseases, such as cancer, neurodegenerative diseases, and metabolic disorders [53], [54]. Two typical strains BY-4741, and CRY-2887 provided by the Institute of Photonics and Electronics of the Czech Academy of Sciences are the main biological models of our research.

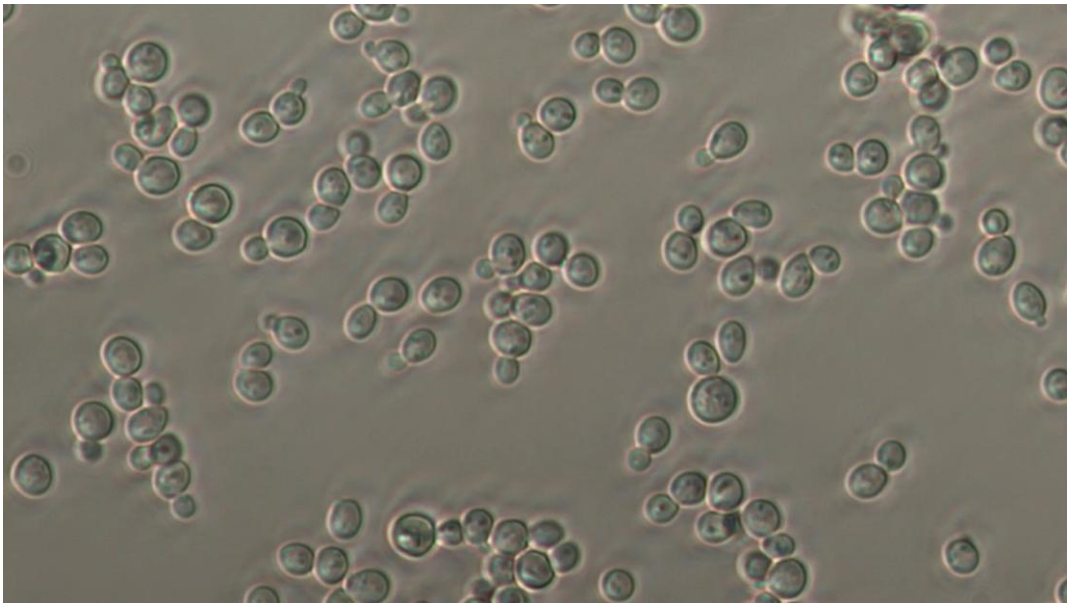

Fig. 2 Yeast *Saccharomyces cerevisiae* under electron micrograph.

3.4 Effects of Electromagnetic Field on Biological Structures

The ratio of the signal amplitude to the thermal noise is essentially linked to the issue of the susceptibility of live cells and tissues to external EMF. Therefore, the applied EMF must be compatible with the exposed system's dielectric characteristics for the anticipated bioeffect to take place.

LF EMF may cause a wide range of biologically significant modifications that can only be understood in terms of non-thermal effects mechanisms. The effect has been seen in

numerous studies at various levels of the structure of living systems: protein phosphorylation, cell proliferation, free radical production, ATP synthesis, changes in membrane structure and function, and subcellular structures like proteins and nucleic acids [57].

From a physical point of view, the non-thermal effects of LF EMF can be divided into:

- electric field effects,
- magnetic field effects.

Selected Effects of Electric Field:

The electric field has a strong effect on both charged and electrical neutral molecules or cellular structures of living organisms. These forces can cause charged particle motion, cellular structure orientation or deformation, dipolar molecule orientation, or voltages across cell membranes.

In substances, binding forces hold bound charges in place, restricting their ability to move. An induced electric dipole is created by applying an electric field, which causes the forces to pull on the positive and negative charges to change direction and separate the charges. The creation of such a dipole by charge separation in the form of induced polarization is a specific characteristic of dielectric materials.

Permanent dipoles, which are randomly oriented in materials, tend to orient themselves according to the direction of the electric intensity vector when an electric field is applied. As the field changes its polarity, the molecules try to rotate to maintain the minimum energy configuration. The resulting arrangement of dipoles produces new fields [57].

Selected Effects of Magnetic Field:

While the ability of the electric field to penetrate tissues is limited and it is necessary to consider several parameters (e.g., frequency, wavelength, the conductivity of the material, etc.), the penetration of the magnetic field through the walls of buildings or human skin takes place practically without attenuation. Conversely, magnetic field shielding is problematic. For this reason, much attention is paid to the possible effects of the magnetic field on human health.

Theories of the possible impact of LF EMF on biological systems include the ability of magnetic induction to induce electric current on cell membranes and in tissue fluids. The current circulates in closed loops that always lie in a plane perpendicular to the applied magnetic field.

An exact calculation of the induced current in the human body is possible only with the use of numerical simulations, but in the situation of a place on the body with homogeneous and isotropic conductivity and homogeneous vector field B, it is possible to approximately express the distribution of currents analytically. In this simplified case, the current density can be derived from Faraday's law of electromagnetic induction:

$$U_i = \frac{d\phi}{dt} \qquad \text{Eq.3.1}$$

where U_i denotes the induced electromotive voltage and ϕ is the magnetic flux.

If the properties of the biological system do not change with time, the induced current is directly proportional to the frequency of the applied field. However, the currents at the interfaces of individual layers of a heterogeneous object are usually different from those predicted analytically according to the relation Eq.3.1.

As can be noticed, a large part of the presented processes takes place on the cellular, or subcellular level, which explains the reason to focus on the mechanisms of LF EMF influence on cells and their structures [57].

4 Cell Concentration Counting Methods

Cell counting and viability determination are critical for almost all microbiological research applications, however, there are many pitfalls in the process of cell counting. In order to address these issues, there have been advances in cell counting over the last decades, enabling the process to become highly automated.

Tab. 4: Different Cell Concentration Counting Methods [58].

	Hemocytometer	Electrical Impedance	Flow Cytometry	Image Analysis
Throughput	Low-throughput,	Very High-throughput	Very High-throughput	Very High-throughput
Reproducibility	Low	High	High	High
Upfront Cost	Inexpensive	Expensive	Expensive	Cost-Effective
Cost/Sample	Inexpensive	Cost-Effective	Higher	Higher
Maintenance	Not Required	Required	Required	Rarely Required
Label Requirement	Trypan Blue Methylene Blue	None	None for scatter, label needed for absorption and fluorescence	Yes,
Sample Concentration (cells/mL)	$2x10^5$ to $2.5x10^6$	$2x10^3$ to $1x10^6$	$1x10^3$ to $1x10^6$	$1x10^4$ to $1x10^7$
Training Requirement	Simple- basic training	Required	Required	Simple training

4.1 Hemocytometer

Despite technical advances, the hemacytometer remains the Gold Standard for many laboratories performing cell-based research. Originally, the hemacytometer was invented to enumerate blood cells, however, this method can be applied to enumerate cells within a diverse array of sample types including blood, cell cultures, urine, and water samples.

Typically, a viability dye such as Trypan Blue is used to distinguish live from dead cells before loading the sample onto the hemacytometer.

At its core, a hemacytometer (Fig. 3) is a specimen slide characterized by an etched grid that generates a 9-square indentation outlining a 1mm x 1mm area, with each square then intersected into cross sections to create the smallest subdivision of 0.00025 mm^2. When covered with a coverslip, it forms a chamber of the height of 0.1 mm and therefore creates a space of a known volume.

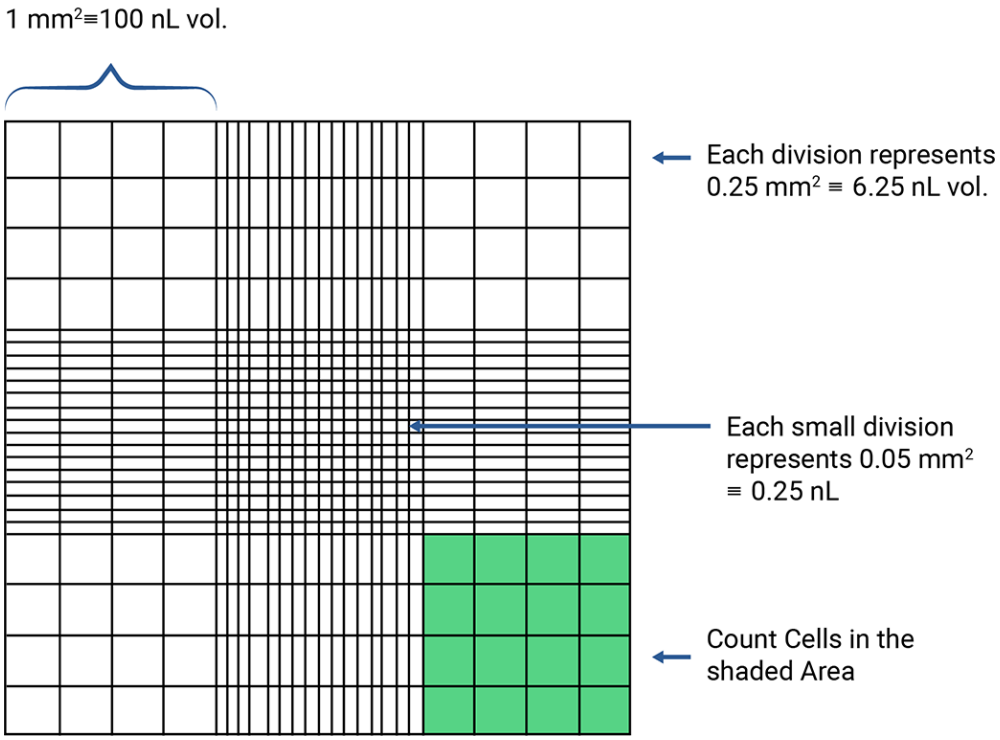

Fig. 3: A closer look at a hemacytometer and its parameters [59].

Typically, cells are counted using a 4x or 10x objective lens over each of the four corners 1mm x 1mm squares and the average is calculated. From this, the cell concentration is determined based on:

Concentration = Average Cell Number x 10^4 x dilution factor

For statistical robustness, the goal is to have roughly 100-200 cells per square, - in some instances, the cell density may not be high enough to achieve this, whereas in others a dilution step may be required, in which case the selected dilution factor may be critical.

The accuracy of cell counting using this method is influenced by several factors principally around human variability in mixing, pipetting, and handling, as well as

instrumentational and material variations between labs and users. Variations between dilution factors may be >55%, and variations between operators have been reported as high as 52% [60]. In order to overcome these high coefficients of variation, multiple counts of the same sample are recommended.

4.2 Turbidimetry

Turbidimetry (the name derived from turbidity) is the process of measuring the loss of intensity of transmitted light due to the scattering effect of particles suspended in it. Light is passed through a filter creating light of a known wavelength which is then passed through a cuvette containing a solution. A photoelectric cell collects the light which passes through the cuvette. A measurement is then given for the amount of absorbed light [61].

Turbidimetry can be used in biology to find the number of cells in a suspension. Turbidity is an expression of the optical look of a suspension caused by radiation to the scattered and absorbed wavelength. Scattering of light is elastic so both incidents and scattered radiation have the same wavelength. A turbidimeter measures the amount of radiation that passes through a fluid in the forward direction, analogous to absorption spectrophotometry.

4.3 Electrical Impedance

Low-frequency electrical impedance measurements can provide insight into the structure and viability of living cells. An idealized circuit model for living tissue is shown in Fig. 4. The capacitive nature of cell membranes accounts for the frequency dependence of cell impedance. If the measurement frequency is high enough, the reactance of the cell membrane capacitance is low. Conversely, low-frequency measurements will have a large reactive component and result in greater impedances with larger phase angles. In human physiology, relationships between quality and the electrical properties of cells have been shown that low-frequency electrical conductivity and capacitance of muscle cells are related to water-holding capacity[63].

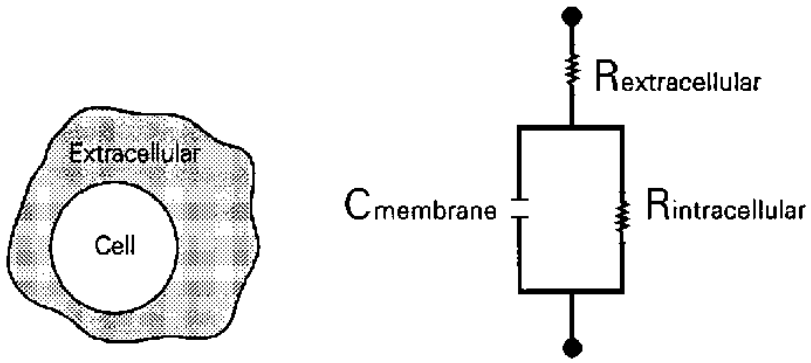

Fig. 4: Idealized equivalent circuit for a living cell [63].

Approach I:

This concentration estimation approach by K. Asami & T. Yonezawa is based on the analysis of the dielectric dispersion. This dielectric technique has been proven to be useful for monitoring cell concentration [64].

Yeast cells are represented by a simple electrical model, referred to as the single-shell model, that is a conducting sphere (of conductivity κ_i) covered with a less conducting and thin shell (of relative permittivity ε_m and conductivity κ_m) (Fig. 5). The relative permittivity ε and conductivity κ of a dilute suspension of the shell-spheres in a continuous medium (of relative permittivity ε_a and conductivity κ_a) are given by Pauly-Schwan's equation [65]. The thickness d of the shell (corresponds to the cell membrane) is much smaller than the radius of the shell-sphere r, i.e., $d/r << 1$. In cell culture, the volume fraction P which is the relative volume of cells occupied in the suspension is usually much smaller than unity, i.e., $P << 1$. Using these assumptions, the frequency dependence of the ε and κ of the cell suspension is approximately expressed as:

$$\varepsilon = \varepsilon_h + \frac{\Delta\varepsilon}{1 + (f/f_c)^2} \qquad \text{Eq. 4.1}$$

$$\kappa = \kappa_l + \frac{\Delta\kappa (f/f_c)^2}{1 + (f/f_c)^2} \qquad \text{Eq. 4.2}$$

where f is the applied ac frequency, f_c the characteristic frequency, $\Delta\varepsilon$ the amplitude of the dielectric dispersion, $\Delta\kappa = 2\pi f_c \varepsilon_0 \Delta\varepsilon$, ε_0 the permittivity of vacuum (ε_0 = 0.08854 pF/cm), ε_h the high-frequency limit of ε and κ_l the low-frequency limit of κ.

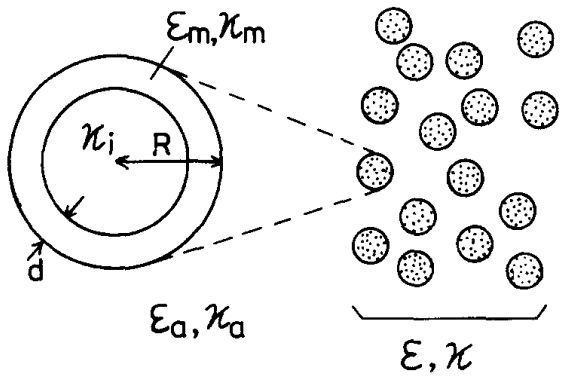

Fig. 5: An electrical model of yeast cells. A sphere of conductivity κ_i (corresponds to the cytoplasm) that is covered with a shell of relative permittivity ε_m and conductivity κ_m (corresponds to the plasma membrane) is suspended in a continuous medium of relative permittivity ε_a and conductivity κ_a. r is the radius of the shell-sphere and d is the thickness of the shell. ε and κ are the relative permittivity and conductivity of the suspension of the shell spheres [64].

The dielectric parameters (ε_h, κ_l, f_c, $\Delta\varepsilon$) are given by

$$\varepsilon_h = \varepsilon_a \qquad \text{Eq. 4.3}$$

$$\kappa_l = \kappa_a \qquad \text{Eq. 4.4}$$

$$f_c \approx \frac{1}{2\pi r C_m}\left[rG_m + \left(\frac{1}{\kappa_l} + \frac{1}{2\kappa_a}\right)^{-1}\right] \qquad \text{Eq. 4.5}$$

$$\Delta\varepsilon \approx \frac{9PrC_m}{4\varepsilon_0}\left[1 + rG_m\left(\frac{1}{\kappa_l} + \frac{1}{2\kappa_a}\right)\right]^{-2} \qquad \text{Eq. 4.6}$$

where C_m is the membrane capacitance given by $C_m = \varepsilon_m\varepsilon_0/d$ and G_m the membrane conductance given by $G_m = \kappa_m/d$. Since viable cells hold for the assumption that $rG_m << \kappa_a$, κ_i, Eq. 4.5 and Eq. 4.6 are simplified as:

$$f_c \approx \frac{1}{2\pi r C_m}\left(\frac{1}{\kappa_l} + \frac{1}{2\kappa_a}\right)^{-1} = \frac{\kappa_a}{\pi r C_m}\left(\frac{\kappa_l/\kappa_a}{2 + \kappa_l/\kappa_a}\right) \qquad \text{Eq. 4.7}$$

$$\Delta\varepsilon \approx \frac{9PrC_m}{4\varepsilon_0} = \frac{3\pi r^4 C_m}{\varepsilon_0} N_c \qquad \text{Eq. 4.8}$$

$$N_c = \frac{\varepsilon_0}{3\pi r^4 C_m}\Delta\varepsilon \qquad \text{Eq. 4.9}$$

where N_c is the cell concentration (the number of cells per unit volume), and P is given by $P = 4\pi r^3 N_c/3$. Eq. 4.9 indicates that a plot of $\Delta\varepsilon$ against N_c gives a straight line, whose slope is proportional to the fourth power of the cell radius because the membrane capacitance C_m is regarded as a constant (about 1 μF/cm^2).

Approach II:

Approach III:

Another approach by Soley et al. [66] is based on the relative variation between electrical impedance at high frequency and low frequency. This method is also another potentially applicable method of impedance spectroscopy application to estimate cell concentration.

The most direct measurement which can be calculated from the voltage (V) and current (I) measurements is the electrical impedance (Z) which is the ratio between V and I. At low frequencies the impedance of a cell suspension is maximum because cell membranes isolate the intracellular space, thus decreasing the conductor volume. As frequency increases, the displacement current across membranes becomes higher, membranes no longer isolate intracellular space, and the impedance of the suspension decreases towards its minimum value (Fig. 6). This behavior, known as impedance relaxation, can be characterized by three parameters: the low frequency (Z_0) and the high frequency (Z_∞) impedance values, and the central relaxation frequency (f_c). f_c is related to cell size, the smaller the cells, the higher f_c. Impedance values at frequencies much lower or much higher than f_c are related to the conductivity of intra and extracellular milieu, and the ratio between intra and extracellular volumes. This behavior can be modeled Eq. 4.10 adapting the Cole-Cole model for the complex permittivity of dielectric materials [67] to the electrical impedance of cell suspensions. The α parameter describes the dispersion of the cell sizes and shapes and is zero for equally sized spherical cells [49].

$$Z(f) = Z_\infty + \frac{Z_0 - Z_\infty}{1 + \left(j\frac{f}{f_c}\right)^{1-\alpha}} \qquad \text{Eq. 4.10}$$

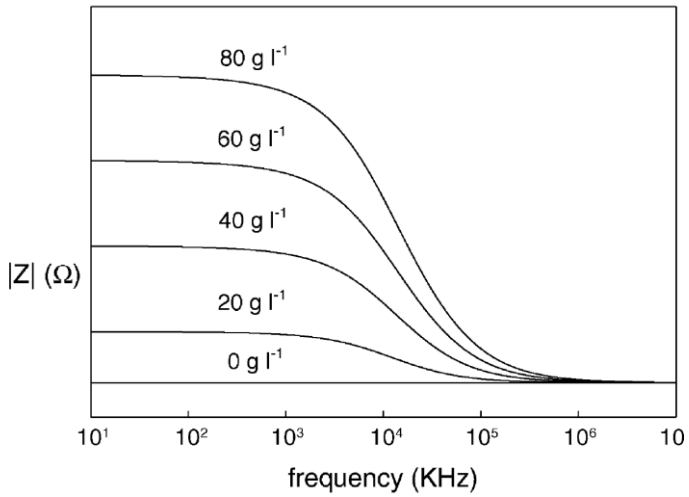

Fig. 6: Effect of the yeast cell volume fraction on the impedance module. Cell volume fractions are expressed as cell concentrations (in g l−1). Impedance relaxations are shown between 10 kHz and 10 MHz.

A single frequency measurement made at low frequency could provide a good *P* estimation of *P*. However, this value is strongly influenced by conductivity changes due to temperature or ionic concentration variations. Because of this, estimators based on relative variations of impedance are expected to show a better performance. The biomass density estimator used in the present work is labeled E_2 and is defined as the relative variation between the low frequency (LF) and high frequency (HF) values of impedance magnitude with respect to the LF value Eq. 4.11.

$$E_2 = 100\left(1 - \frac{|Z(HF)|}{|Z(LF)|}\right)(\%) \qquad \text{Eq. 4.11}$$

where E_2 is the biomass estimator, $|Z(LF)|$ the impedance magnitude at $f \ll f_c$ and $|Z(HF)|$ is the impedance magnitude at $f \gg f_c$.

The biomass estimator, E_2, is a function of the cell size (*R*), membrane capacitance (C_m), volume fraction (*P*), and intra and extracellular conductivities (σ_i and σ_e). Assuming that $P < 0.2$ (v/v) and that the intra and extracellular conductivities are similar, it can be demonstrated that E_2 is linearly dependent on *P* and that does not depend on the other parameters [68]. In practical conditions, *R*, C_m, and σ_i are constants for a given microorganism but σ_e can present variations.

5 Development of Measurement Platform

Design and development of an experimental platform is the first and most vital step of our research. Measuring instruments of the platform must be chosen appropriately in order to be compatible with each other while maintaining their required functionality. Development of the platform started during the previous VEGA projects. From the constructed foundation of the platform, many modifications and improvements have been and are being applied.

5.1 The Experimental Workflow

A key component of the design of the experimental platform is the use of pair experiments, where two cultivation chambers are operated in parallel under controlled and nearly identical environmental conditions. Depending on the goal of the experiments, the pairing could involve a test vs. control, test vs. test, or control vs. control configurations. This flexible setup enables both differential exposure studies and internal validation of environmental symmetry. By comparing biological outcomes from pair samples within the same run, the approach minimizes external variability and improves statistical robustness.

The proposed workflow of the experiments is schematically illustrated in the diagram in Fig. 7. It outlines the design of a pair experiment suitable for investigating LF MF effects on microbial cultures. The workflow starts with a yeast strain from The Culture Collection of Yeasts (CCY) (Institute of Chemistry, Slovak Academy of Sciences, Slovakia) which is maintained on a solid medium in a Petri dish and used as an inoculum for pre-cultivation phase.

After completing the pre-cultivation process, the yeast culture is appropriately diluted, distributed into vials, and placed into cultivation chambers. These chambers are equipped with active temperature regulation and independent monitoring systems to ensure that both chambers remain within tightly controlled thermal limits. The integrated magnetic exposure system allows both channels to be independently configured in either exposure or control mode, enabling precise control over LF MF application. After completion of the cultivation process, measurements of cell concentration are performed, followed by structured data

analysis including data filtering and verification. Subsequently, only validated datasets are used in the final phase of statistical evaluation.

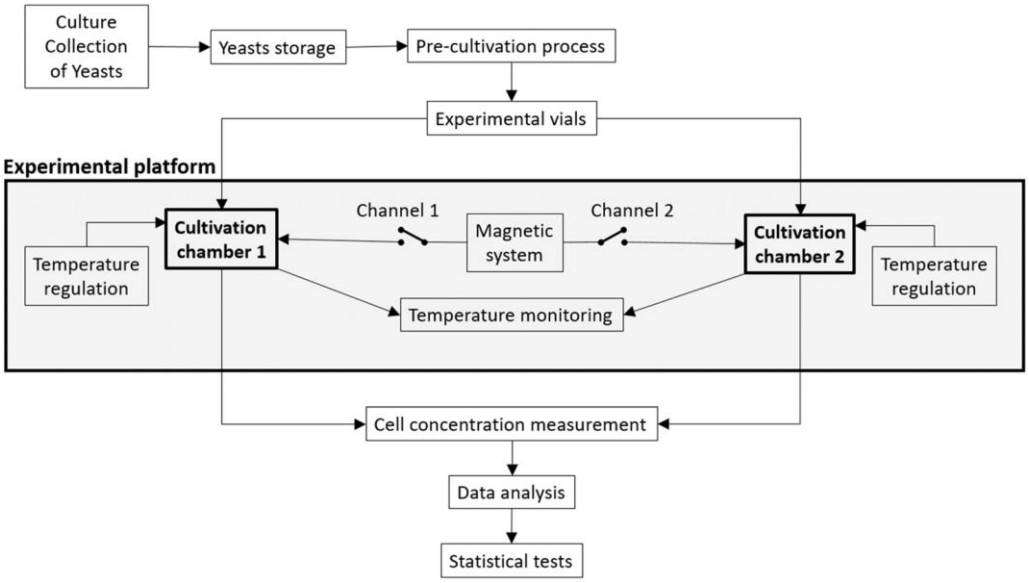

Fig. 7: Schematic of the experimental workflow for low-frequency magnetic field exposure studies. The platform integrates two temperature-controlled cultivation chambers connected to a dual channel magnetic field generation system, implemented with temperature monitoring ensures thermal consistency.

The experimental platform is composed of four main components: two almost identical custom-designed cultivation chambers, a precision temperature control system, an MF generation unit, and a central unit for system control and data acquisition. In addition, an optical microscope (Kern OCL-2, Kern & Sohn,) equipped with a digital camera (FLC 1600H, Do3thing) is used for cell counting and microbiological purity assessment of the samples.

5.2 Helmholtz Coils

A fundamental requirement for the proper realization of experiments investigating the effects of magnetic fields on cell cultures is the generation of a homogeneous magnetic field in the region where the cells are located. Since the cultures are typically placed on a flat substrate, a two-dimensional approximation can be adopted, where ensuring uniformity of the magnetic field within the plane of the cells is sufficient for experimental reliability. This condition is crucial for avoiding spatial variability in field intensity that could otherwise confound biological interpretations.

Such a homogeneous alternating magnetic field can be technically achieved using two air-core coils, wound from copper wire and mounted on spools in the well-known Helmholtz

configuration. This arrangement allows for a uniform magnetic field to be produced in space between the coils, particularly in the central region where biological samples are positioned. Because of its field uniformity and relative simplicity, the Helmholtz setup is a standard choice for bioelectromagnetic research, especially when evaluating low-frequency magnetic field exposure effects under controlled conditions.

To ensure the validity of experiments designed to investigate the influence of magnetic fields on cell cultures, it is essential that the magnetic field be homogeneous within the region occupied by the cells. Given that the cultures are positioned on a planar substrate, it is reasonable to adopt a two-dimensional approximation, where homogeneity of the magnetic field within the plane of the cells is considered sufficient for experimental accuracy. Such a homogeneous alternating magnetic field can be technically achieved using coils arranged in a Helmholtz configuration. Such a homogeneous alternating magnetic field can be technically achieved using two air-core coils wound from wire onto spools and arranged in a Helmholtz configuration.

The Helmholtz coil configuration is illustrated in Fig. 8a. It consists of two identical circular coils placed symmetrically along a common z-axis and separated by a distance equal to their radius R. Both coils carry an equal current I flowing in the same direction, generating a magnetic field that is uniform in the central region between the coils. This spatial arrangement is designed to minimize the second derivative of the magnetic field at the midpoint, thus ensuring its homogeneity, which is critical for sensitive biological or physical experiments. The corresponding graph in Fig. 8b demonstrates the variation in magnetic flux density B between the coils along the z-axis. Among the plotted curves, the one corresponding to the Helmholtz condition (equal spacing and radius) shows the flattest region in the center, confirming the effectiveness of this configuration in producing a uniform field over the sample volume. This property makes Helmholtz coils particularly suitable for studies requiring controlled magnetic environments, such as low-frequency magnetic field exposure in biological systems [69].

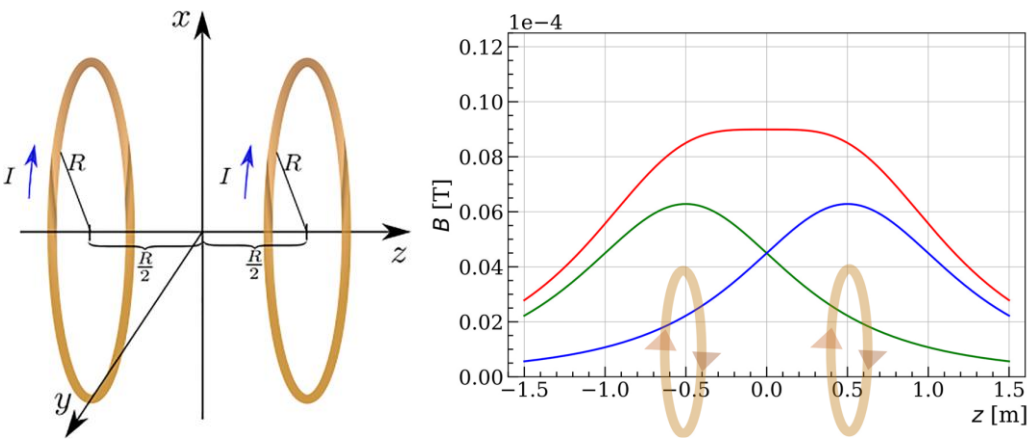

(a) (b)

Fig. 8: (a) Schematic representation of a Helmholtz coil pair with radius *R*, carrying current *I* in the same direction to generate a uniform magnetic field at the center. (b) Magnetic flux density *B* as a function of position *z* along the central axis, showing the field distribution for different coil configurations [69].

The parameters of coils (coil diameter, wire diameter, number of turns, and number of wire layers) were optimized within the target magnetic field for frequency range (Hz–kHz) while constraining the internal heat generation of the coils below 2 W. The optimization aimed to maximize the magnetic flux density at the center of the Helmholtz coil configuration while maintaining homogeneous magnetic field density in x-y plane. The magnetic field was calculated using a multilayer-corrected formula based on the classical Helmholtz expression [69], [70]:

$$B_{max} = \sqrt{2}.\left(\frac{8}{5\sqrt{5}}.\mu_0.I_{max}.N_0.\sum_{i=1}^{k}\frac{1}{r_i}\right) \qquad \text{Eq. 5.1}$$

Where B_{max} refers to the maximum magnetic flux density that can be generated by the coil system given its specific parameters. It represents the strongest possible field achievable in the center of the Helmholtz coil setup, considering the limitations of current, number of turns, geometry, and heating constraints. In other words, B_{max} is the peak field strength at the midpoint between the coils, where the field is also the most homogeneous. μ_0 is the permeability of free space, N_0 is the number of turns per layer, and r_i represents the radius of each *k* winding layer. The factor $\sqrt{2}$ accounts for the constructive superposition of the fields from the two coils spaced one radius apart.

Importantly, the maximum current I_{max} allowed through the coils was dynamically limited by the smallest of three constraints:

$$I_{max} = min\left(I_{amp}, \frac{U_{amp}}{Z}, \sqrt{\frac{P_{heat}}{R}}\right) \quad \text{Eq. 5.2}$$

where I_{amp} and U_{amp} are the amplifier's maximum current and voltage, Z is the total circuit impedance, and P_{heat} is the thermal power dissipation limit (2 W). We have implemented the optimization procedure in MATLAB (see Appendix F – Supplement Programing Codes) (Fig. 9).

Simulated maximum magnetic flux density as a function of the number of wires-turns on the spool of 120 mm of coil inner diameter, 2.2 mm of wire diameter, and approximately 387 µH of the simulated coil inductance, is shown in Fig. 11. From the simulation, as the number of turn increases, both resistance and inductive reactance rise, reducing current at given voltage and in turn limiting the magnetic flux density. This interaction results in a non-monotonic field profile as shown in Fig. 9, where the increase in coil turns eventually leads to a drop in field due to heat and voltage limits.

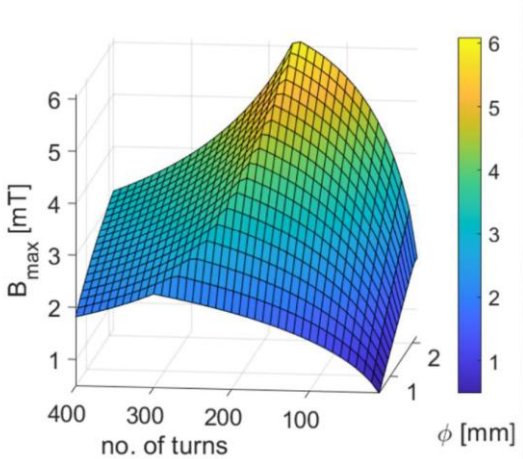

Fig. 9: Modelling of the maximum magnetic flux density as a function of the number of coil turns and the wire diameter.

The modeling led to the final construction resulted in two identical air-core circular coils designed according to the Helmholtz configuration. Each coil consists of 50 turns of 2.2 mm copper wire, arranged in 5 layers with 10 turns per layer.

The windings were implemented on 3D-printed cylindrical spools with a base diameter of 110 mm and a wall thickness of 3 mm. The resulting coils had an inner diameter of 116 mm and an outer diameter of 125.84 mm, yielding an average coil diameter of approximately 121 mm (Fig. 10). The coils were mounted facing each other with a center-to-center separation of 60 mm, which corresponds to half of the average coil diameter,

calculated as the mean of the inner and outer coil radii. This specific spacing is critical to satisfying the Helmholtz condition, which ensures that the magnetic field remains homogeneous across the central region between the coils.

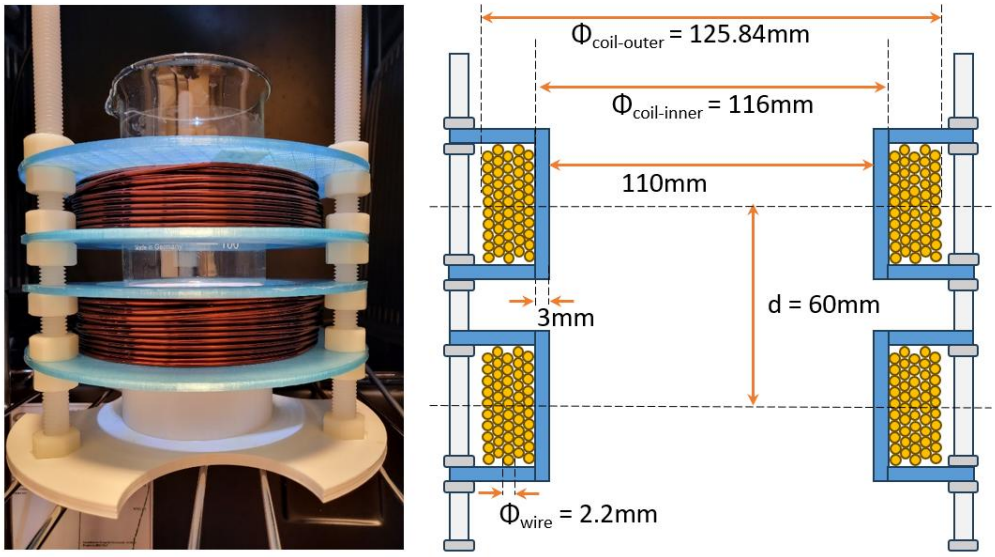

(a) (b)

Fig. 10: (a) Realized Helmholtz coil assembly inside the cultivation chamber. (b) Technical schematic of the coil dimensions

The electrical resistance of the Helmholtz coil pair was estimated based on design parameters, using the standard formula (Appendix C), the calculated resistance of both coils in series was approximately 0.152 Ω for the wire length of 34.5 m used in coils.

The Direct Current Resistance (DCR) was measured usinsg a Keithley 2000 Multimeter in Kelvin 4-wire configuration (Appendix C), yielding a result of 0.1851 Ω ± 0.00008 Ω and 0.1968 Ω ± 0.00008 Ω, which is consistent with expectations due to additional resistance from solder joints, connector terminals, and measurement tolerance.

The calculated theoretical inductance of one coil using Wheeler's formulas [71] is approximately 443 µH, yielding 886 µH for two coils in series (Appendix C).

The inductance of the Helmholtz coils was measured using the Agilent 4284A LCR meter in a Kelvin 4-wire configuration at four distinct frequencies: 50 Hz, 1 kHz, 10 kHz, and 100 kHz. Measured series resistance R_s and inductance L_s of the coils of series equivalent circuit mode are summarized in Tab. 5.

Tab. 5: measurement of the coil's inductance at different frequency.

Frequency	Coil 1		Coil 2	
	Ls [mH]	Rs [Ω]	Ls [mH]	Rs [Ω]
50Hz	1.01555	0.17917	1.03872	0.17827
1 kHz	1.00066	0.23515	1.00269	0.24685
10 kHz	0.962195	2.38468	0.999790	2.54109
100 kHz	0.944739	10.4233	0.983496	14.0448

*Details of the uncertainty calculation are provided in (Appendix C)

As observed, the inductance of both coils remains consistently close to 1 mH across the tested frequency range, showing only minor frequency-dependent variation. For Coil 1, the inductance deviation from 1 mH is approximately +1.56% at 50 Hz, +0.07% at 1 kHz, –3.78% at 10 kHz, and –5.53% at 100 kHz. For Coil 2, the deviation is approximately +3.87% at 50 Hz, +0.27% at 1 kHz, –0.02% at 10 kHz, and –1.65% at 100 kHz. These variations reflect the expected parasitic effects such as wire proximity and skin effects, which become more pronounced at higher AC frequencies. The small difference between Coil 1 and Coil 2, generally under 3%, suggests a high level of symmetry and consistency in the winding and construction.

It has to be noted that the measured inductance L_s in the series equivalent model decreases with increasing frequency. This behavior is attributed to parasitic effects within the coil structure, specifically, the presence of unintended (parasitic) capacitance between adjacent windings. More precise coil's equivalent circuit includes also an unknown (and distributed) parasitic capacitance C_p in parallel to the RL, forming an RLC network that distorts the measurements especially at higher frequencies. This effect artificially reduces the measured inductance even though the physical coil properties remain unchanged. This multi-frequency analysis allowed us to assess the frequency-dependent behavior of the inductance and confirm the stability and consistency of the coil design across the target application range.

5.3 System for Magnetic Field Generation

The magnetic system consists of a pair of Helmholtz coils, signal generator Owon XDG3102, and an electronic power amplifier Behringer NX3000D. The frequency and amplitude of generated MF by Helmholtz coils are adjustable using an arbitrary waveform

generator. The power amplifier provides AC currents up to 8 A (rms) for the coils in the frequency range 0-2 kHz, generating magnetic flux density up to 5 mT. The magnetic system can be that operated in two configurations: dual mode and bridge mode.

In Bridge Mode (Fig. 11a), the two generator channels are internally combined into a single high-power output by the amplifier, which is used to drive one coil. To ensure compatibility with the amplifier's output requirements, a potentiometer is connected in series with the coil. This allows fine-tuning of the total load impedance, taking into account the coil's inherent properties and cable resistance. An oscilloscope is connected across the coil to monitor the waveform characteristics such as amplitude and shape, ensuring that the signal remains stable and within required parameters throughout the experiment.

In Dual Mode (Fig. 11b), each channel of the waveform generator operates independently and is routed to separate amplifier inputs. This enables simultaneous operation of two coils each located in its own cultivation chamber. Each coil is connected in series with a variable load resistor and an ammeter to enable current monitoring and precise adjustment of the operating conditions. This setup allows for the parallel application of magnetic fields, supporting comparative or symmetric testing scenarios across both chambers.

In pair experiments, the magnetic field generated inside two cultivation chambers should be identical. Measured magnetic flux densities generated inside two chambers at 800 Hz (X_L = 5.027 Ω) for different excitation voltages are compared in Tab. 4. The resulting ratio of two magnetic flux densities is close to 1.01, the difference is below 2 percent.

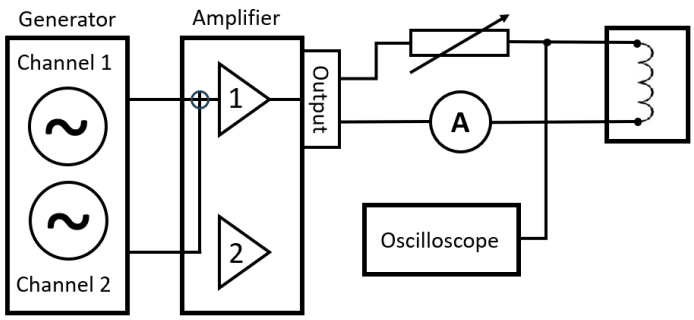

(a) Bridge Mode

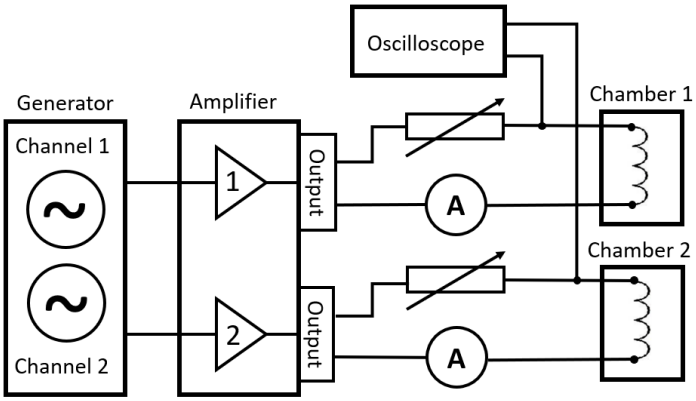

(b) Dual Mode

Fig. 11: Schematics of the magnetic field exposure system. (a) Bridge Mode: both generator channels are combined and used to power a single coil through one amplifier output. (b) Dual Mode: each generator channel is independently amplified and used to drive separate coils in parallel. Potentiometers are included to adjust the output impedance load to match amplifier requirements

Tab. 6: Comparison of the magnetic flux density of the two coils at frequency 800Hz (X_L = 5.027 Ω).

Coil I				Coil II				B1/B2
Ch1 [Vpp]	Ch2 [Vpp]	I_{rms} [A]	B1 [mT]	Ch1 [Vpp]	Ch2 [Vpp]	I_{rms} [A]	B2 [mT]	
Setup		Meas.	Meas.	Setup		Meas.	Meas.	
0.016	0.016	0.0146	0.0052	0.016	0.016	0.0142	0.0051	1.01
0.138	0.138	0.1556	0.0469	0.138	0.138	0.1517	0.0460	1.02
1.380	1.380	1.5814	0.9391	1.380	1.380	1.5532	0.9291	1.01
2.750	2.750	3.1493	1.8904	2.750	2.750	3.0932	1.8681	1.01
4.170	4.170	4.7717	2.9113	4.170	4.170	4.6880	2.8768	1.01
5.550	5.550	6.3520	4.6967	5.550	5.550	6.2440	4.6720	1.01
7.050	7.050	8.0690	5.9774	7.050	7.050	7.9300	5.9281	1.01

5.4 Homogeneity of Magnetic Field

To verify the homogeneity of the magnetic field generated by the designed Helmholtz coils, the magnetic flux density was measured inside a low-form 250 ml beaker with an inner diameter of 76.50 mm. The beaker was positioned in the center of the coils, with its outer wall placed 18.80 mm away from the coil edge (Fig. 12). A total of 15 measurement points were defined within the beaker, distributed across three horizontal planes from bottom to top: the bottom layer (orange) closest to the base, the middle layer (blue) placed 6.00 mm above it, and the top layer (green) 12.00 mm above the bottom. Each plane consists of five measurement points forming a square plus one central point, as illustrated in Fig. 12. A magnetic flux density probe was inserted vertically into the beaker, aligned with the magnetic field direction for axial flux density readings.

All dimensional measurements were performed using a SOMET INOX vernier caliper with a resolution of 0.02 mm, providing a high degree of precision for spatial positioning within the experimental setup. Accordingly, the uncertainty in all length measurements is estimated to be ±0.01 mm.

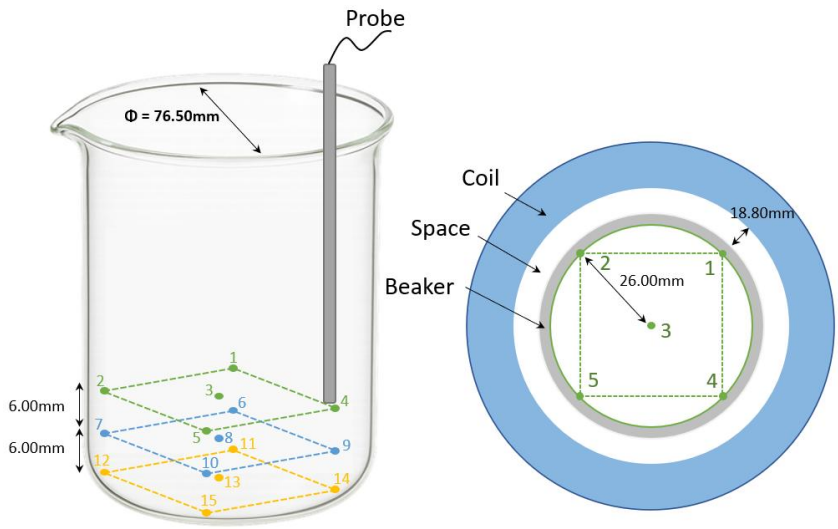

Fig. 12: Magnetic flux density of MF measuring locations inside the beaker.

Multiple measurements were conducted under different excitation conditions. The waveform generator was set to output sinusoidal signals from both channels (e.g., 3.5 V peak-to-peak at 1 kHz), which were merged in bridge mode via the amplifier to power the Helmholtz coils. The output was monitored using an oscilloscope, while the current entering the coil was measured using an ammeter. Magnetic flux density values at each of the 15

locations. The results are summarized in Table 4, showing the spatial distribution of the magnetic field at various driving conditions and confirming the field's homogeneity within the measured volume.

Magnetic flux density measurements were carried out using a SYPRIS Model 7010 Gauss/Tesla meter, which offers reliable sensitivity and precision. According to the instrument's specifications, the accuracy in AC mode is ±1% of the selected range. Accordingly, the uncertainty in the measured magnetic flux density is ±0.03 mT when using the 3 mT range, and ±0.3 mT when using the 30 mT range.

To evaluate the spatial variation of the magnetic field, the relative standard deviation (RSD) was calculated for each case using the following formula:

$$RSD = \left|\frac{Standard\ deviation\ (B)}{mean\ (B)}\right| * 100\% \qquad \text{Eq. 5.3}$$

This metric quantifies the spread of the measured values across the volume as a percentage of the mean field strength. It allows direct comparison of homogeneity regardless of the absolute field magnitude.

Across all tested conditions, no extreme outliers or abrupt spatial drops in field strength were observed. The results confirm that the Helmholtz coil configuration provides a reasonably homogeneous magnetic field within the targeted central volume of the beaker. The highest uniformity was found at moderate operating levels (1000 Hz), while slight increases in deviation occurred at both higher and lower input powers, likely due to nonlinearities in current distribution or external influences.

While some variation in homogeneity is observed, it is important to note that magnetic flux density uniformity tends to decrease as the distance from the central axis of the Helmholtz coil increases. However, in this setup, a narrow low-form beaker was used centrally aligned within the coils. The working volume of experiment involving active stirring is intentionally kept under 100 ml to confine the experimental subject within the most homogeneous region of the field. Experiments without stirring, where sedimentation causes the cells or materials to settle at the bottom of the beaker, which is also the highly uniform field zone. This effectively minimizes the influence of edge discrepancies on the results

Tab. 7: Magnetic flux density measurements at 15 defined points inside the beaker for different excitation input signal frequencies (800 Hz, 1 kHz, and 2 kHz). The table includes input signal settings, measured output voltages and current. Magnetic flux density values at each position. Summary statistics (mean, min, max, standard deviation, and relative standard deviation) are provided to evaluate the spatial homogeneity of the field.

Input Signal Setting			
Freq [Hz]	800	1000	2000
Vpp [V]	4.17	3.50	10.00

Measured Output Signals			
Vpp [V]	80.80	37.60	143.00
Vrms[V]	27.35	13.1	48.20
Irms [A]	4.81	1.49	3.67

Measured B [mT]			
1	2.96	1.12	0.197
2	2.99	1.10	0.203
3	2.92	1.12	0.192
4	3.00	1.12	0.204
5	3.02	1.12	0.205
6	3.05	1.13	0.196
7	2.96	1.10	0.202
8	2.86	1.15	0.193
9	2.95	1.15	0.199
10	2.98	1.13	0.203
11	3.06	1.12	0.194
12	3.00	1.09	0.204
13	2.81	1.15	0.190
14	2.95	1.14	0.198
15	3.00	1.13	0.205

Mean	2.96	1.12	0.199
Min	2.81	1.09	0.190
Max	3.06	1.15	0.205
SD	0.0661	0.0185	0.0051
RSD	2.23%	1.64%	2.57%

Overall, the measured RSD ranging between 1.64% and 2.57% demonstrate that the system provides sufficiently homogeneous conditions for experiments that are not sensitive to sub-millitesla spatial fluctuations, such as magnetic field exposure studies on cells, small sensors, or materials.

5.5 Temperature Regulation in Cultivation Chamber

Customized thermal boxes (based on glass door refrigerator unit, Candy CCV 150 EU) were heated using heating foils placed on both side walls of the. Temperature regulation was provided by a PID temperature regulator (Rex C100V Pt100, rKc Instrument), equipped with a sensor submerged in the water bath holding the experimental vials. Additionally, a temperature monitoring system was implemented using a microcontroller board (Arduino UNO Rev3) with three digital temperature sensors (DS18B20, Analog Devices, Inc.,) and a sampling period of 10 s.

Before implementing the PID regulation system, an initial setup was using a simpler on-off temperature controller. Temperature measurements were logged using a temperature data logger (Voltcraft, PL-125-T4) equipped with a K-type thermocouple sensor. The recorded temperature profile, shown in Fig. 13, represents the temperature variation measured directly in the sample. Although the system eventually reached a stable oscillatory regime, the temperature fluctuated between a minimum of 30.7 °C and a maximum of 33.7 °C resulting in a total spread of 3.0 °C and standard deviation of 0.54 °C. This level of variation was considered insufficient for our experimental requirements, particularly for yeast cultures sensitive to even minor thermal deviations. The limitations with the on-off control approach motivated the transition to a more advanced and stable regulation system, which enabled tighter temperature control and improved experimental reliability.

To address this issue, a PID temperature controller (Rex C100) was implemented to regulate the heating foils lining the inner walls of the cultivation chambers (Fig. 14). The PID parameters proportional (P), integral (I), and derivative (D) were automatically tuned using the PID training regime built into the controller itself. This auto-tuning process adapted the control loop to the specific thermal dynamics of the system, including the heat delivery characteristics of the foil heaters. The finalized PID settings were P = 1.8, I = 3600, and D = 900, which offered markedly improved thermal stability across long-term operation. With this configuration, the typical temperature variation was reduced to within ±0.3 °C,

with worst-case deviations not exceeding ±0.5 °C—representing a significant improvement and a solid step forward in enhancing the reliability of the experimental platform.

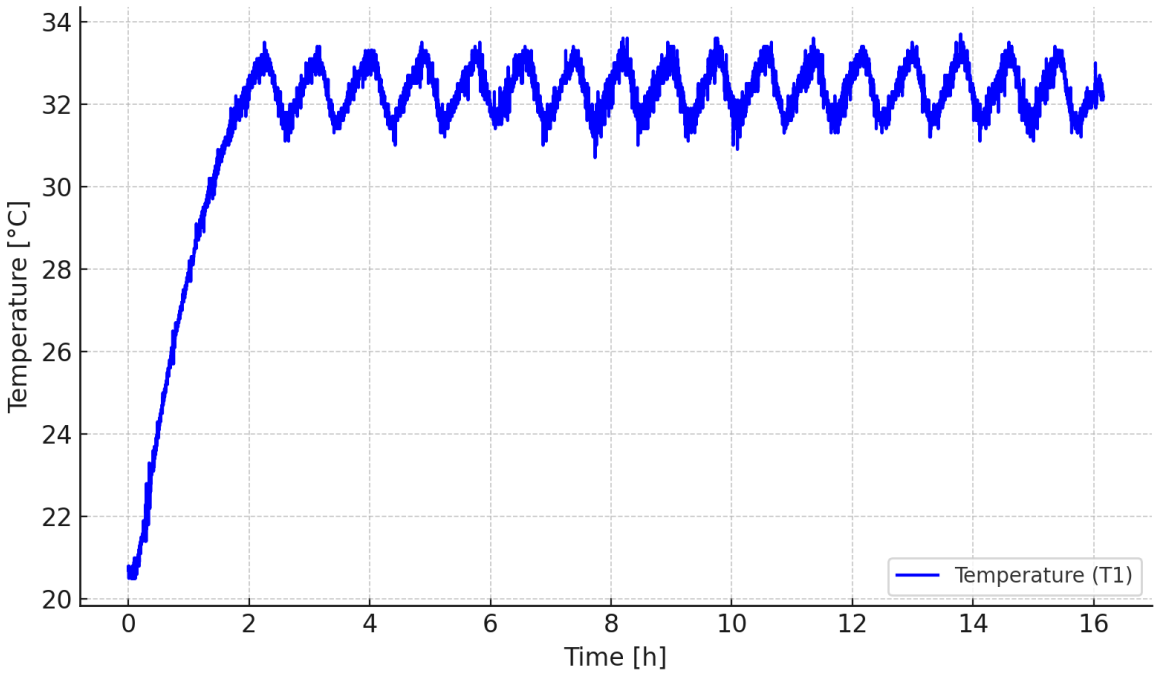

Fig. 13: Temperature profile recorded using an on-off temperature controller and K-type thermocouple sensor. After initial stabilization, the temperature oscillated between approximately 30.7 °C and 33.7 °C, resulting in a fluctuation of 3.0 °C. This level of variability was found to be insufficient for sensitive biological experiments, prompting the adoption of a more precise PID-based regulation system.

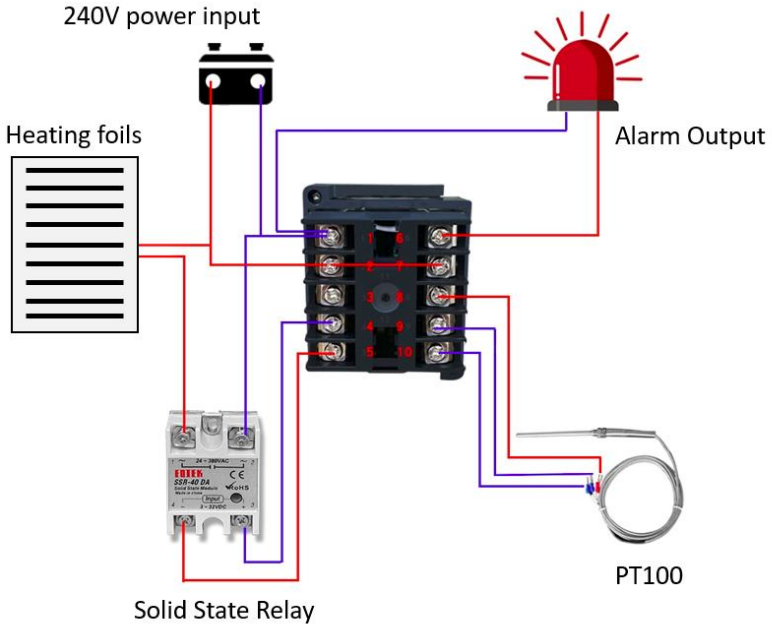

Fig. 14: PID temperature controller connection diagram.

In addition to improved temperature control system, a 3D-printed structural stand was designed and implemented to provide precise and fixed positioning of the Helmholtz coil within the cultivation chamber. This mechanical upgrade significantly improved the thermal performance of the system. In earlier designs, the coil assembly was placed loosely in the chamber's original tray, which introduced uncontrolled variability in positioning and airflow, affecting temperature distribution inside the chamber also the temperature difference between each experiment. The upgraded 3D stand provided consistent alignment and vertical spacing between coil elements and the sample vials, thereby enhancing the overall symmetry and thermal stability within the chamber. This design refinement further contributed to the system's improved temperature regulation and experimental reproducibility.

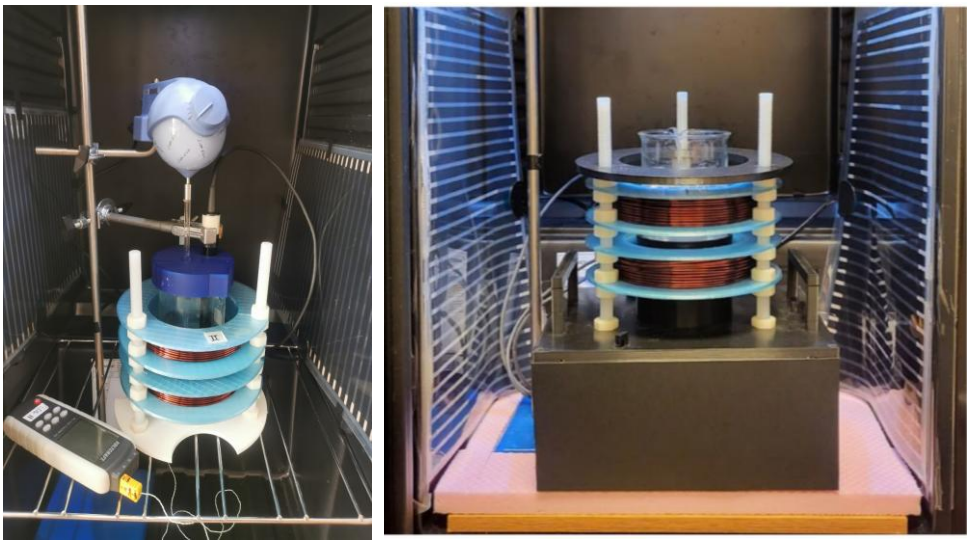

(a) (b)

Fig. 15: (a) Previous version of the Helmholtz coil setup, placed loosely inside the original chamber tray without fixed positioning or thermal optimization, along with temperature monitoring using a K-type sensor connected to a digital logger (b) Updated configuration with a custom 3D-printed stand enabling precise, stable placement of the coil and sample vial,

After the PID parameters were established, a series of temperature distribution tests was carried out inside the chamber, using multiple sensors placed at different locations simultaneously. Here, we illustrate one such test performed with the regulator set to 35 °C: one sensor was submerged in the water bath containing vials with water, while two other sensors were positioned at different heights within the chamber (Fig. 16a right). Although temperature discrepancies of more than 5 °C were detected among the sensors, the submerged sensor in the water bath consistently recorded stable temperatures (Fig. 16b). The scenario depicted in Fig. 16 was more demanding because the coils were switched on,

serving as an additional heat source; nevertheless, the set temperature of 35 °C was maintained, mirroring conditions observed when the coils were switched off.

Based on these tests, the final placement of the sensors was as follows: one sensor was submerged in the water bath in each cultivation chamber to directly monitor the temperature of the yeast samples, while the third sensor measured the ambient room temperature at a height of approximately 1 m above the floor.

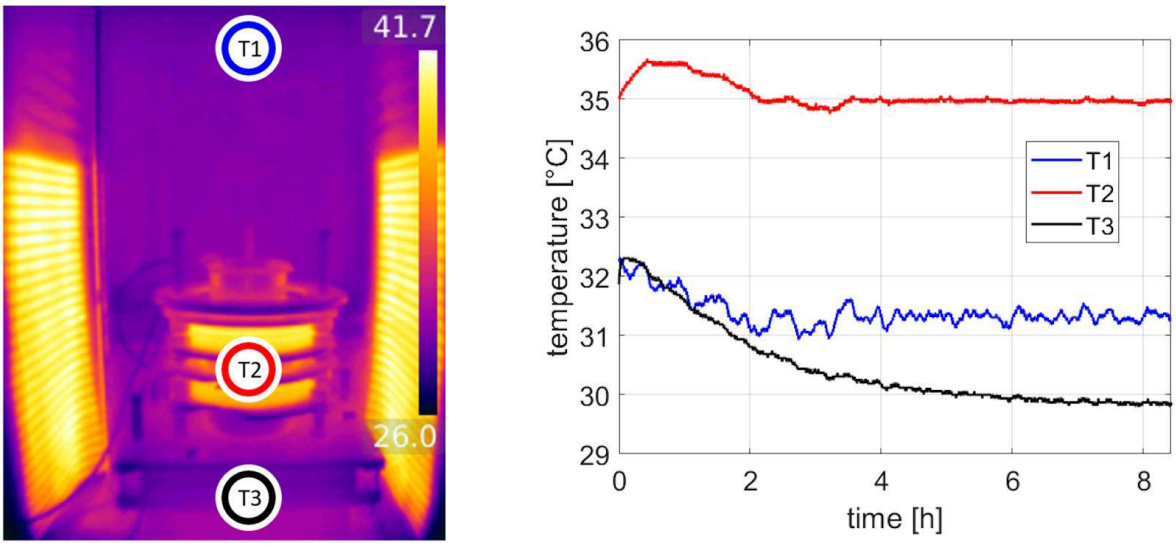

(a) (b)

Fig. 16: (a) thermal image of the Helmholtz coil system placed inside the cultivation chamber
(b) Temperature stability test in the chamber with the PID controller set to 35 °C. T1 – top of the cultivation chamber, T2 – water bath in the beaker, T3 – bottom of the cultivation chamber.

5.6 In-situ Temperature Monitoring of Samples

To monitor thermal stability during experiments, a simple yet effective temperature logging system was developed using an Arduino Uno and three DS18B20 digital temperature sensors (Fig. 17). These sensors were positioned to measure the temperature of the samples inside Chamber 1, Chamber 2, and the ambient room temperature. The sensors were wired using the OneWire protocol and supported by pull-up resistors, allowing for simultaneous and accurate data acquisition from all three points. Real-time temperature values were displayed on an LCD module, offering visual feedback during operation. This setup enabled tight environmental control, crucial for isolating potential biological effects caused by weak low-frequency magnetic fields, while minimizing confounding variables such as temperature drift.

Temperature was monitored using a digital temperature data logger equipped with a K-type thermocouple as mentioned in previous section. While initially sufficient for basic measurements, the device suffered from several drawbacks: the software interface was outdated, the output format required manual conversion for analysis, and the thin K-type sensor wires were fragile and prone to breakage. In contrast, the DS18B20 sensors offered more robust performance, higher reliability, and seamless integration with the Arduino based digital platform, making them better suited to our experimental needs.

For data acquisition, the Arduino system was configured to send timestamped temperature values from all three sensors via its serial interface. These outputs were read using the Arduino IDE's Serial Monitor and automatically logged into a text file. Each line of the file contained the timestamp and the corresponding temperatures from Chamber 1, Chamber 2, and the room. The logged data was subsequently imported into spreadsheet software (such as Excel) for visualization, plotting, and further analysis. This simple pipeline enabled continuous long-term monitoring without the need for expensive commercial equipment and proved sufficient for evaluating temperature regulation performance throughout the experimental runs.

Following data acquisition, the recorded temperature values were post-processed to evaluate stability and ensure comparable environmental conditions across tests. The spreadsheet analysis included calculating the mean and standard deviation of each temperature channel, identifying fluctuations, and highlighting outliers. Special focus was placed on the temperature difference between the two cultivation chambers, computed as the absolute difference between their mean values (ΔT). This parameter was used to filter experimental runs and ensure thermal symmetry between conditions. Only experiments where the temperature difference between chambers stayed within ±0.3 °C were accepted for further biological interpretation. This strict inclusion criterion reflects the sensitivity of cell cultures to temperature deviations and ensures that any observed effects can be reliably attributed to magnetic field exposure rather than thermal imbalance.

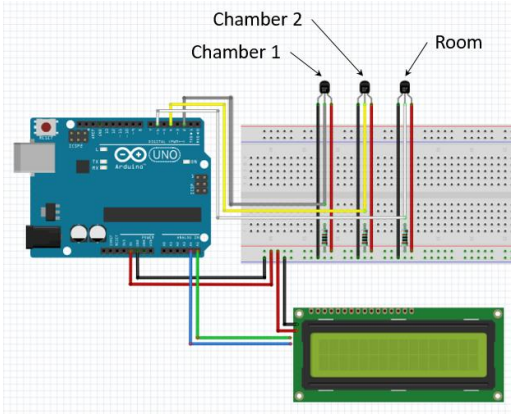

2024-10-07 20:56:53	34.06	34.00	21. 81
2024-10-07 20:57:08	34.00	34.00	21. 81
2024-10-07 20:57:18	34.06	34.00	21. 81
2024-10-07 20:57:27	34.00	34.00	21. 81
2024-10-07 20:57:33	34.00	34.00	21. 81
2024-10-07 20:57:43	34.06	34.00	21. 81
2024-10-07 20:57:53	34.00	34.06	21. 81
2024-10-07 20:57:58	34.06	34.00	21. 81
2024-10-07 20:57:58	34.06	34.06	21. 81
2024-10-07 20:58:08	34.00	34.00	21. 81
2024-10-07 20:58:23	34.06	34.06	21. 81
2024-10-07 20:58:33	34.06	34.00	21 81
2024-10-07 20:58:48	34.06	34.06	21. 81
2024-10-07 20:58:58	34.06	34.00	21. 81
2024-10-07 20:59:43	34.06	34.00	21. 81
2024-10-07 20:59:58	34.06	34.06	21. 81
2024-10-07 20:59:58	34.06	34.00	21. 81
2024-10-07 20:59:38	34.06	34.06	21. 81
2024-10-07 20:59:43	34.06	34.13	21. 81
2024-10-07 20:59:48	34.06	34.13	21. 81
2024-10-07 20:59:53	34.06	34.06	21. 81
2024-10-07 20:59:58	34.06	34.13	21. 81
2024-10-07 20:00:03	34.06	34.13	21. 81
2024-10-07 21:00:12	34.06	34.13	21. 81
2024-10-07 21:00:18	34.06	34.13	21. 81
2024-10-07 21:00:28	34.06	34.13	21. 81
2024-10-07 21:00:37	34.06	34.13	21. 81
2024-10-07 21:00:37	34.06	34.13	21. 81

(a) (b)

Fig. 17: (a) Schematic of the Arduino-based temperature monitoring system. Three DS18B20 digital sensors are used to measure the temperature of the samples inside Chamber 1, Chamber 2, and the ambient room. The system includes real-time data display on an LCD module and data logging via serial communication. (b) Logged data includes timestamped temperature values, later processed for thermal stability evaluation.

5.7 Completed Experimental Platform

The comprehensive experimental platform in Fig. 18 represents the complete system for low-frequency magnetic field exposure studies. Fig. 18 shows the full laboratory setup, including two temperature-regulated and monitored cultivation chambers, Helmholtz coils connected to a signal generation and amplification unit, digital oscilloscopes for waveform verification. Central control is facilitated through a data acquisition unit. An optical microscope with a digital imaging system supporting evaluation of cell cultures. A key design feature is the capability of supporting pair experiments, where both chambers operate in parallel under near-identical conditions. This allows flexible configurations such as test vs. control, test vs. test, or control vs. control, enhancing internal consistency. The synchronized infrastructure ensures stable environmental parameters, reproducible magnetic exposure, and high-fidelity data capture enabling statistically robust biological assessments.

To support experimental reproducibility, a standardized procedural workflow was established. This includes clearly defined pre-cultivation and main experiment protocols to ensure that every step is executed precisely since skipping even a single step may critically impact the results. Special attention was given to maintaining sterility throughout the long hour duration experiments, as contamination (e.g., bacterial overgrowth in YPD medium) was found to significantly affect measurement accuracy. The detailed procedure (Appendix A - Experimental procedure) mitigates such risks and ensures consistent conditions across experiments.

Fig. 18: The complete experimental platform setup for low-frequency magnetic field exposure studies.

6 Cell Concentration Monitoring Based on Impedance Spectroscopy

After the experimental platform was properly built and the system started to operate as designed, multiple verifications and adaptations were performed before we started to analyze the concentration estimation methods.

To perform impedance spectroscopy measurements for monitoring cell concentration, a high-resolution impedance analyzer was integrated into the experimental setup. The analyzer supports a wide frequency range and provides precise complex impedance data, enabling real-time tracking of dielectric properties in biological samples. It was configured with a 4-wire electrode system to reduce the impact of electrode polarization and improve measurement accuracy across a spectrum of 10 Hz to 10 MHz. Further technical specifications and hardware details of the impedance spectroscopy analyzer used in this research are provided in Appendix B - Impedance Spectroscopy Analyzer.

The very first measurement was to verify the impedance measurement spectra of different cell concentration samples. According to our expectations, two different cell concentration samples which were counted via hemacytometer using microscopic images of the Bürker counting chamber, displayed different impedance spectra (Fig. 19).

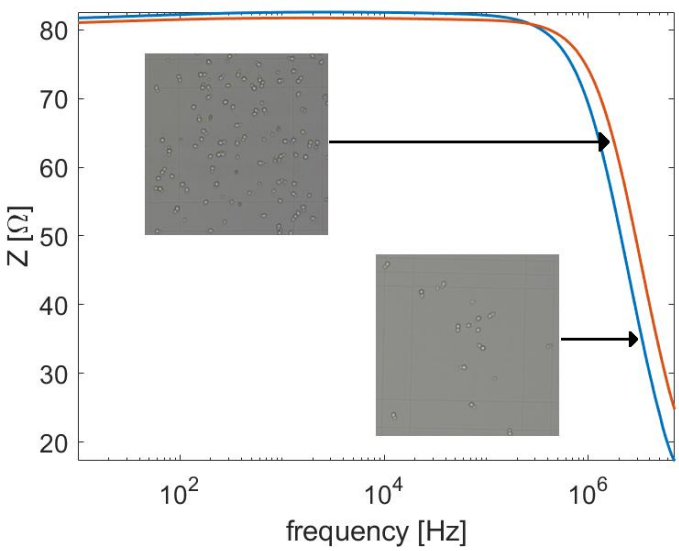

Fig. 19: The cell samples with different cell concentrations display different impedance spectra

From the obtained impedance spectra, cell concentration was calculated. Several approaches for concentration estimation were considered. After a series of thorough testing,

two estimation approaches were considered to be taken into further study. The first estimation approach was proposed by Asami and Yonezawa (see 4.3) [64] and the second approach is described in a study by Soley (see 4.3) [66].

In order to collect impedance spectra serving as data for the concentration estimation approaches, we executed multiple testing experiments. We experimented with different factors, e.g., different speed of stirrer, cultivation temperature in the chamber, and medium solution (YPD, distilled water, salted water), attachment of impedance probe or beaker cover, etc. Afterwards, pair tests in a “control vs control” mode provided us a comparison of the growth condition for yeasts inside both chambers. And finally, we performed tests and adjustments in “test vs control” mode during which the cell sample in one cultivation chamber was set to be exposed to the MF while in the other chamber MF was not applied.

The outcome of one “test vs control” experiment is shown in Fig. 20 where MF with the magnetic induction of 3 mT at the frequency of 800 Hz was applied in the chamber (box) 1 while the chamber 2 was without the application of MF. The result displays the estimated cell concentrations of the measurement calculated by using both approaches I and II. The result on the left was received from the calculation using approach II by Soley A., et al. Impedance of the HF at 10 Mhz, and impedance of the LF at 1 kHz was selected to apply in Eq. 4.11. As displayed, curves of both samples have a downward trend suggesting the cell concentration was decreasing during the experiment, which is not matched with the result from hemacytometer and microscopic captured pictures. Under current circumstances, these questions are the application of this method in our experiment. Further investigation is needed to understand and eliminate this problem. The result retrieved using estimation approach I by Asami and Yonezawa (Fig. 20b) was on the other hand more promising. The selected frequency for the calculation of Eq. 4.1 was 3.2 Mhz. The calculated concentrations of both samples have an upward trend, where a period from min. 400 to approximate min. 650 indicates the exponential growth phase of both samples. Due to the differences between the two Orion conductivity probes (one is older, and one is newly acquired), there is an offset in the measured spectra, resulting also in the obtained concentrations. The curves in Fig. 20b are thus calibrated by 2-point calibration method, where the starting and ending points are set according to the real concentrations obtained by hemocytometer method.

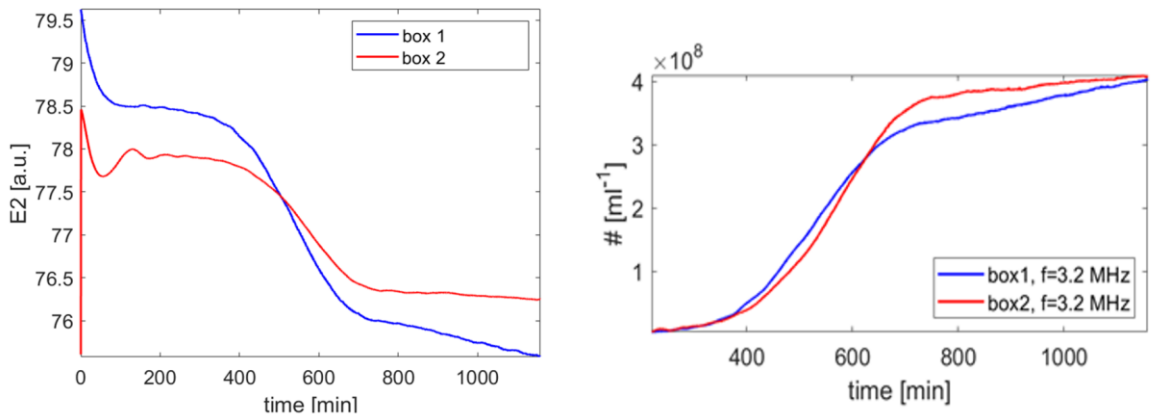

(a) (b)

Fig. 20: Comparison of calculated yeast cell concentration trends using two impedance-based estimation approaches. (a) Results based on the method by Soley et al., using frequency points from 1 kHz and 10 MHz, display a decreasing concentration trend inconsistent with the expected cell growth behavior. (b) Results based on the method by Asami and Yonezawa, using 3.2 MHz as the optimal frequency for concentration estimation, show an increasing trend matching expected biological growth, supporting better reliability for further analysis

We took a closer look at the result calculated from Asami and Yonezawa's estimation approach and applied different frequencies (20 kHz, 400 kHz, 3.2 Mhz, 10 Mhz) for concentration calculation using Eq. 4.11. Fig. 21. displays various results obtained from these calculations. Different choices of frequency result in either minor adjustments in the concentration trend or level of noise. It follows that choosing the appropriate frequency for concentration calculation is important to this method.

Further analysis of the calculation using the frequency of 3.2 MHz in Fig. 22 shows the resulting multiplication rate of cells in the two samples (primary y-axis). From min. 600, there is a visible sign of inhibition of the cell sample in chamber number 1 which was exposed to MF with the magnetic induction of 3 mT at the frequency of 800 Hz. The ratio between the two samples (secondary y-axis) reached 1,14 at its maximum, meaning the concentration of the sample which was not exposed to MF is about 14% higher than the one that was placed in the chamber with the active MF. It is to be noted that in the beginning, the ratio between the two multiplication rates has a high level of noise mainly due to the stabilization of cell concentration during the lag phase and the stabilization of temperature inside the cultivation chamber.

This is one of the promising results of our study. However, more experiments and calculations must be performed in order to collect enough data for proper analysis and conclusions.

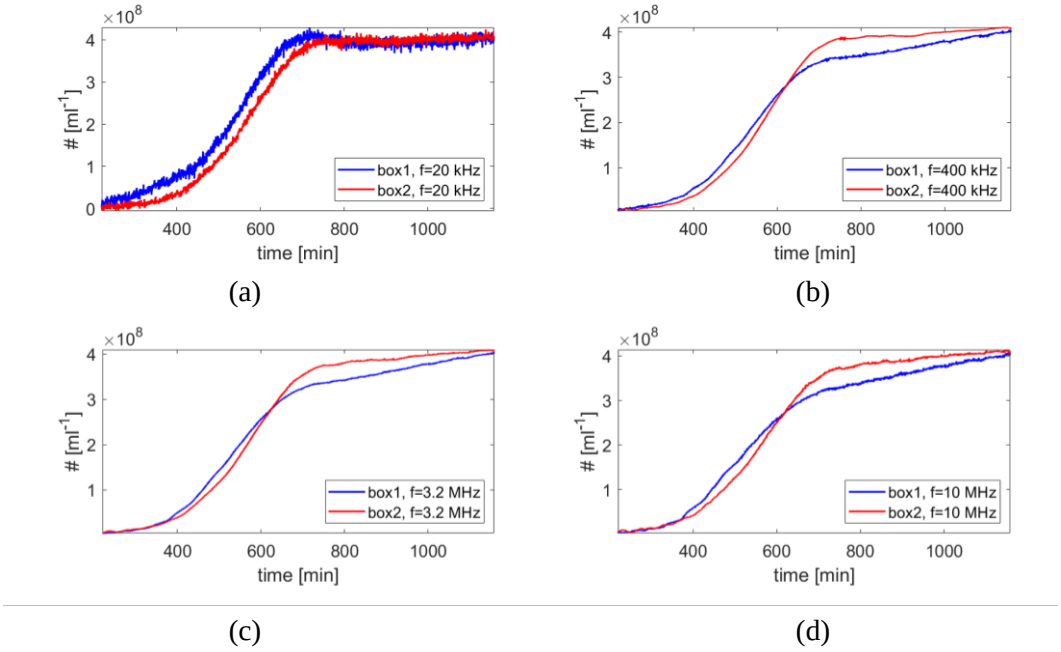

Fig. 21: Calibrated cell concentration curves calculated using the Asami and Yonezawa approach at different frequencies. (a) 20 kHz, (b) 400 kHz, (c) 3.2 MHz, and (d) 10 MHz. The frequency of 3.2 MHz (c) shows the most stable and biologically consistent growth pattern with minimized noise. Comparison across plots highlights how frequency selection significantly influences the accuracy and noise level of impedance-based cell concentration estimations.

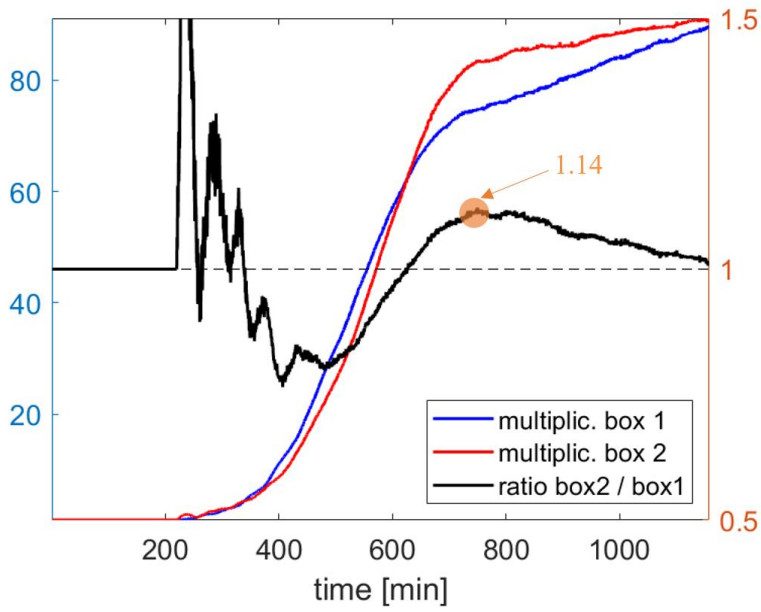

Fig. 22: Comparison of multiplication rates and growth ratio between MF-exposed and control yeast cultures based on impedance-derived concentration at 3.2 MHz. The primary y-axis shows the estimated multiplication rate for the exposed sample (blue, chamber 1) and the control sample (red, chamber 2). The secondary y-axis (black curve) represents the ratio of control to exposed concentrations (chamber 2/chamber 1), highlighting the relative growth advantage of the control sample. A noticeable inhibition of growth appears after 600 minutes, with the ratio peaking at approximately 1.14 indicating a ~14% higher concentration in the control. The initial fluctuations are attributed to stabilization delays in temperature and cell concentration during the early lag phase. Magnetic field parameters were 3 mT at 800 Hz.

Several experimental parameters were optimized to improve reliability and reduce measurement artifacts. This included evaluating the effects of electrode geometry and environmental stability, particularly temperature fluctuations and medium conductivity, on impedance readings. This section describes the systematic approach taken to identify and minimize sources of error, ensuring that the observed impedance changes more accurately reflect biological processes rather than external interference.

6.1 Interference of Mechanical Vibration with Impedance Measurement

The presence of any external magnetic field source around the experimental platform during the main measurement could introduce significant artifacts, compromising the accuracy of impedance data. Consequently, a magnetic stirrer cannot be used during the main experiments. To avoid this issue, a mechanical stirring system was employed, constructed entirely from non-magnetic materials—specifically aluminum and glass. These materials ensure that the stirrer does not interfere with the generated magnetic field. This setup allows for continuous mixing of the culture medium without introducing electromagnetic noise. Nevertheless, under the assumption that the stirrer and the stirring mechanism are entirely non-electrical and non-magnetic, they are considered to have no direct influence on the magnetic field generated during the experiment, this choice introduces another challenge, identified as mechanical vibrations.

To investigate the effect of steering on the impedance measurements, the experiment commenced with the mechanical stirrer set at 0 rpm, and the stirring speed was subsequently increased in steps, each held for a duration of approximately 5 minutes. The relationship between the measured impedance and the stirrer rotation speed is depicted in Figure 25. It is clearly visible that with the increase in stirrer speed (100 rpm, 260 rpm, 600 rpm), the measured impedance increased up. In addition, impedance noise also intensified with the increase in stirring speed. Notably, a significant increase in signal noise occurred at 260 rpm, which was originally selected as the mechanical stirrer speed during experiments due to its effectiveness and consistency in mixing the cell culture and medium, and became extreme at 600 rpm, confirming that the mechanical agitation had a direct influence on impedance stability. These observations suggest that the vibrations added noise to the measured impedance and systematically influenced the impedance readings.

To balance effective mixing with signal stability, we set the mechanical stirrer speed to 200 rpm. This speed provided a practical trade-off: it maintained homogeneous mixing of the experimental solution while minimizing mechanical noise and impedance drift during data acquisition.

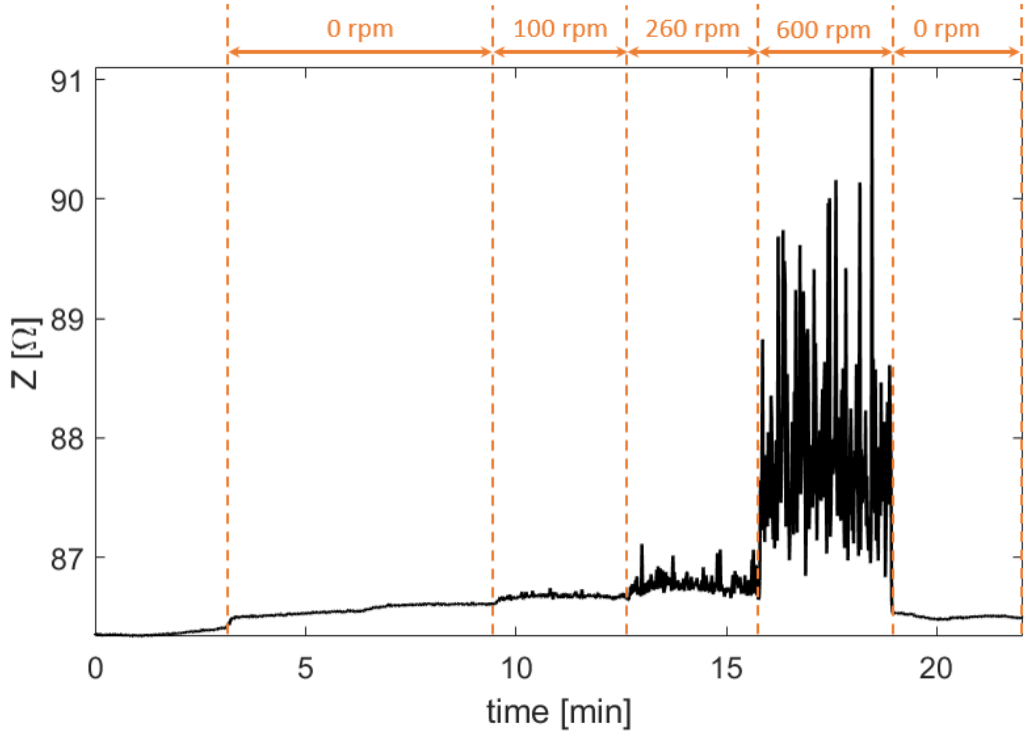

Fig. 23: Influence of the stirring on measured impedance. The black curve shows the measured impedance (Z) over time. The vertical orange dashed lines indicate transitions in stirrer speed: 0 rpm → 100 rpm → 260 rpm → 600 rpm → 0 rpm. The initial sudden jump in impedance at the beginning of the plot corresponds to the moment the measurement probe was submerged into the sample; prior to that, the probe was not in contact with the medium. An apparent increase in the impedance and uncertainty (noise) correlate with higher rotational speeds, demonstrating mechanical vibration interference.

6.2 Improvement of the Measurement Conditions Using Bioreactor

During early experimental runs, we observed an unexpected linear increase in the impedance signal over time, which was initially interpreted as a potential indicator of cell growth. However, in order to verify whether this signal truly reflected biological changes or was instead an artifact, we designed and performed two control experiments without cells.

In the first experiment, we measured saltwater prepared to match the conductivity of fresh YPD medium, using two Orion probes simultaneously. As shown in the Fig. 24 , the measured effective conductivity increased linearly over time in both chambers. Similarly,

permittivity measured also showed a steady increase. Since no biological processes were present, this trend could not be attributed to cell growth.

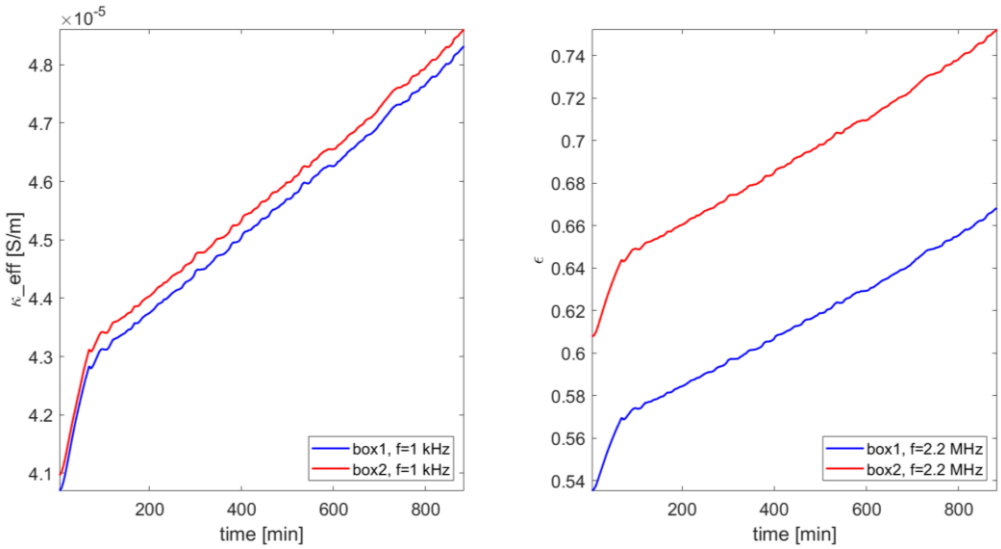

(a) (b)

Fig. 24: Control measurement using saltwater without cells. Both effective conductivity (a) and permittivity (b) increase linearly over time in both chambers, indicating the presence of a physical artifact unrelated to biological activity.

In the second experiment, we measured only fresh YPD medium, again without any added cells. As illustrated in Fig. 25, the resulting conductivity and permittivity curves closely mirrored those observed in the saltwater test—both rising gradually and linearly with time. The strong similarity between these two control experiments confirmed that the observed impedance signal increase was not due to changes in cell concentration, but rather a physical artifact.

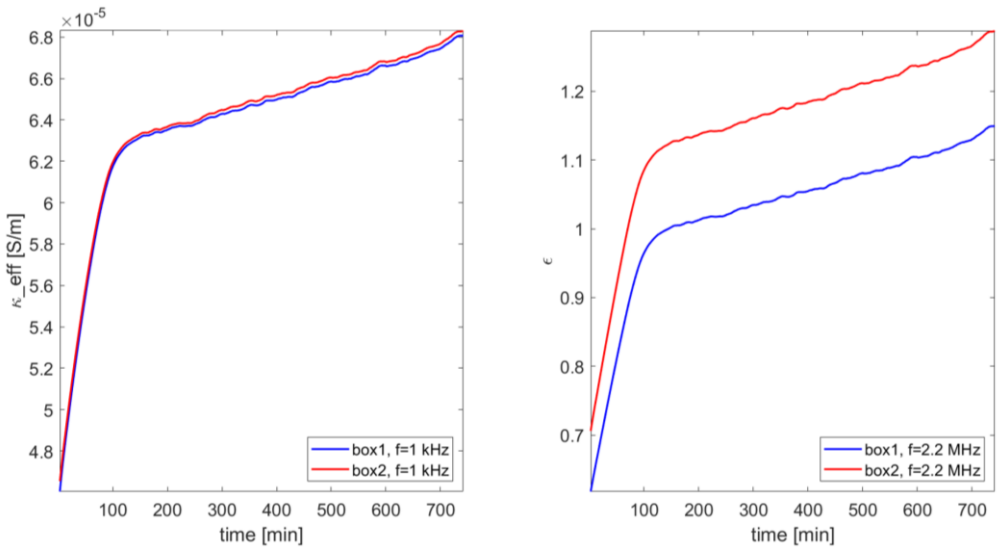

(a) (b)

Fig. 25: Control measurement using fresh YPD medium without cells. Effective conductivity (a) and permittivity (b) curves again show a steady increase over time, mirroring the saltwater test results and confirming that the observed signal rise is not due to cell growth.

We hypothesized that the primary cause of this artifact was evaporation of the medium during long-term measurement. As water evaporates, the concentration of salts and solutes in the remaining volume increases, leading to higher conductivity and dielectric properties. This explanation was consistent with both the data and environmental conditions in our system.

To eliminate the evaporation effect and achieve stable, closed-system cultivation, we developed a custom bioreactor system, as shown Fig. 26. The bioreactor consists of a sealed glass cultivation vessel (resembling a jar) fitted with a metal lid through which multiple components are integrated: a 4-electrode Orion probe for impedance spectroscopy, an internal glass stirring bar driven by a stirrer to ensure homogenous mixing

The jar is sealed using a silicone ring, screw lid, including one isolation foam layer, minimizing air exchange while maintaining sufficient sterility. The vessel is then placed inside a custom 3D-printed cylindrical holder for thermal insulation and fixation. The complete setup is integrated into the Helmholtz coil structure for magnetic field experiments and maintained in a thermostatically controlled environment with PID regulation.

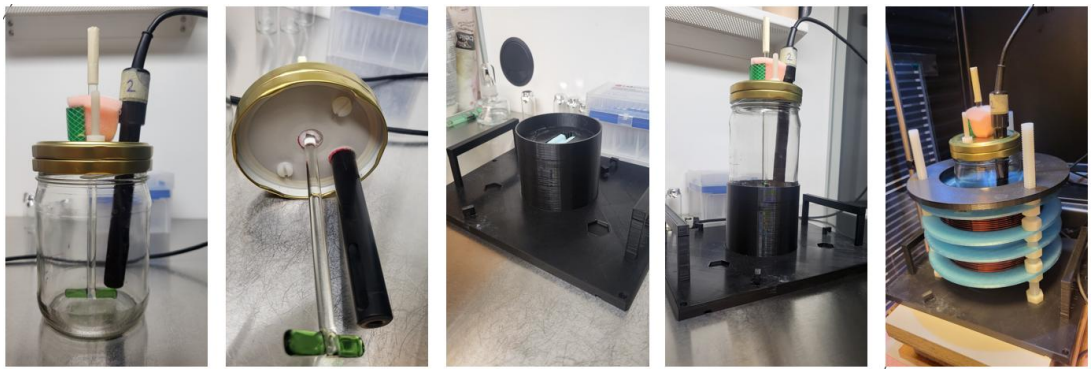

(a) (b) (c) (d) (e)

Fig. 26: Assembly of the custom-designed sealed bioreactor system for long-term impedance spectroscopy experiments under magnetic field exposure. (a) Sealed cultivation bioreactor with integrated 4-electrode Orion probe and stirring mechanism. (b) View of the lid showing electrode insertion and sealing components. (c) Custom 3D-printed base. (d) Final bioreactor setup positioned inside the base. (e) Full integration of the sealed bioreactor inside the Helmholtz coil system with temperature control for stable measurements.

After implementation, we re-evaluated the system using fresh YPD medium in the newly developed bioreactor. The results, shown Fig. 27, demonstrated a significant improvement in signal stability. The previously observed linear increase in both effective conductivity and permittivity was no longer present. Instead, the curves quickly stabilized after an initial transient phase, followed by minor fluctuations that correlate with subtle temperature changes, likely due to thermal regulation cycles. These fluctuations are minimal and do not suggest any cumulative drift.

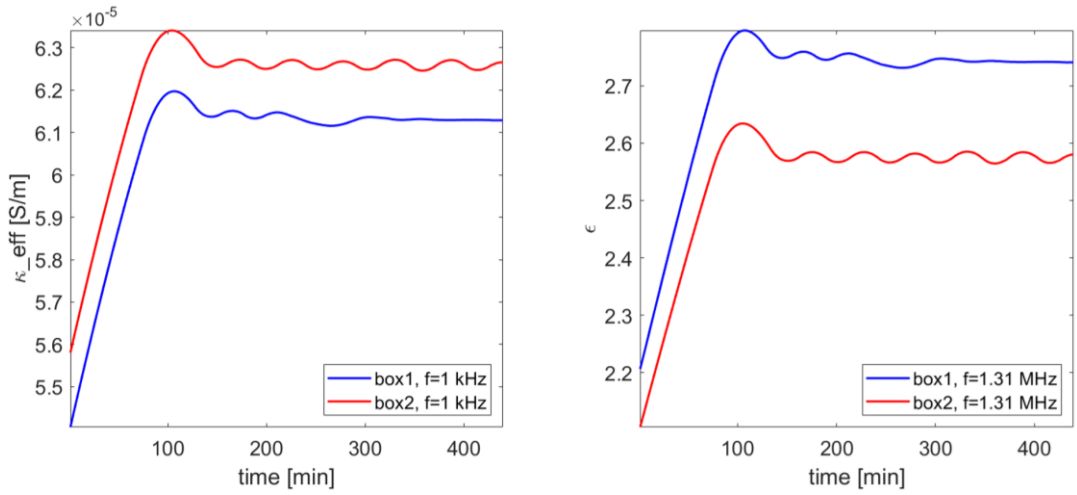

(a) (b)

Fig. 27: Impedance measurements in the newly developed sealed bioreactor using fresh YPD medium. Both effective conductivity (a) and permittivity (b) curves rapidly stabilize after an initial transient, demonstrating effective elimination of evaporation artifacts and enabling stable, reproducible long-term measurements.

The bioreactor successfully eliminates evaporation-driven artifacts, enhances sterility, which enhances the accuracy, precision, and reproducibility of impedance measurements, enabling stable and reliable long-term monitoring. It ensures that any changes observed in future biological experiments are more likely to represent true physiological phenomena rather than environmental interference. This advancement was a critical step in improving the reliability and interpretability of our experimental platform.

6.3 Challenges in Impedance-Based Real-Time Concentration Monitoring

During the development and testing of the experimental platform, significant challenges were encountered in using impedance spectroscopy for reliable estimation of yeast cell concentration. Although the system was conceptually designed around known theoretical models (such as those by Soley et al. and Asami & Yonezawa), our experimental findings consistently pointed to serious limitations of this approach under our specific conditions.

One of the earliest and persistent issues was related to the two Orion impedance probes used throughout the experiments. These probes, although of the same model, were not identical in performance. One was newer and intact, while the other, originally used in our lab, had visible signs of surface degradation due to frequent use in previous experiments. When both were used to measure the same medium under the same conditions, the resulting impedance values differed significantly in absolute terms, although the overall trends were similar. This forced us to implement offset corrections between the probes, highlighting a key limitation in reproducibility and trustworthiness of absolute impedance values without rigorous recalibration.

As part of a separate validation test, we performed an experiment where salt was gradually added to distilled water, and the system measured both actual and calculated effective conductivity. In this case, results were consistent and showed a strong correlation, confirming that the analyzer correctly reflects effective conductivity changes in stable media. This demonstrated that the device itself functions as expected when not confounded by biological complexity or electrode effects.

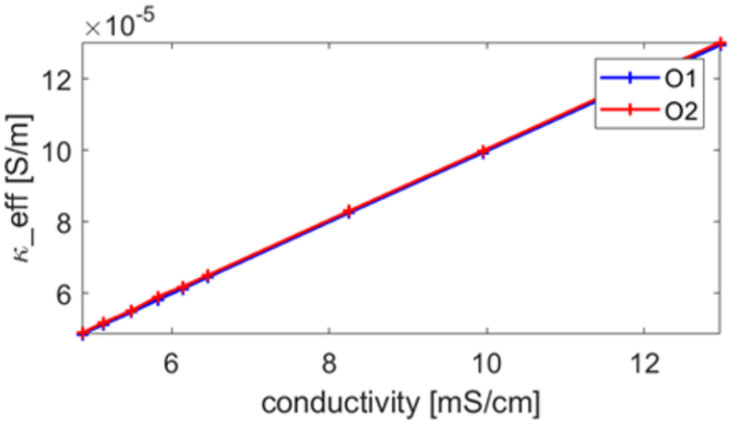

Fig. 28: Validation of the impedance analyzer using stepwise salt addition to distilled water. The strong correlation between measured conductivity and calculated effective conductivity for both Orion probes (O1 and O2) confirms that the system accurately reflects conductivity changes in stable cell-free media.

In the next validation step, we aimed to establish a calibration curve between cell concentration and permittivity. 14 concentration points were prepared, spanning from 100% down to 0%, and the corresponding permittivity values were recorded. As shown in Fig. 29, while the overall trend suggests an increase in permittivity with higher concentrations, the measurements at lower concentrations (especially below 20%) exhibit notable fluctuations. In fact, some of these lower concentration readings show unexpectedly high permittivity values exceeding those at 60% concentration indicating poor reliability in this range and undermining the interpretability of the calibration curve.

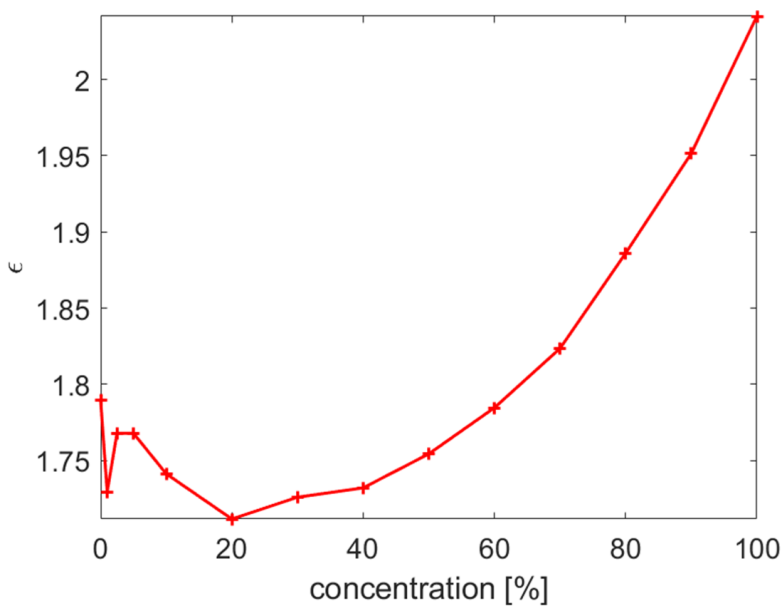

Fig. 29: Permittivity, derived from impedance measurements using Asami & Yonezawa model at frequency 1.31 MHz, across 14 discrete concentration levels ranging from 100% to 0%. While higher concentrations follow a general increasing trend, permittivity values at lower concentrations (<20%) exhibit significant fluctuations and inconsistencies, with some values exceeding those recorded at 60%, indicating unreliable calibration in this range.

A central experiment designed to validate impedance as a concentration estimator involved gradual, discrete addition of yeast cells into fresh YPD medium across nine increments. To maintain consistent environmental conditions, the temperature stabilized using an ice bath at 0 °C, pH remained steady, and conductivity showed minimal variation throughout the experiment. Despite these ideal conditions, the impedance readings failed to exhibit a monotonic or interpretable trend that aligned with the increasing number of cells. The E2 parameter, calculated using low frequency (LF = 1 kHz) and high frequency (HF = 2 MHz), and the permittivity, derived from impedance measurements at 2 MHz, both were able to indicate some changed and displayed slight increases over time appeared to follow changes related to actual biomass input (Fig. 30). However, these apparent changes were highly fluctuated and were only visible under a highly zoomed-in scale, making them unlikely to represent meaningful or reliable signals. These minor and inconsistent variations raise concerns about the suitability of the method for real-time concentration monitoring in medium with biological complex.

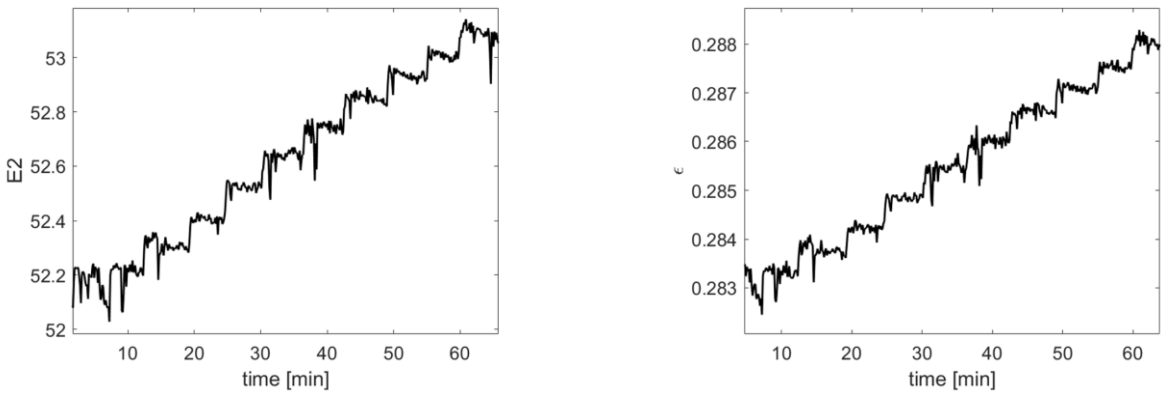

(a) (b)

Fig. 30: Gradual addition of yeast cells into fresh YPD medium across 9 steps, with impedance monitored using two estimation approaches. (a) E2 calculated using dual-frequency (1 kHz and 2 MHz), (b) permittivity calculated at 2 MHz. Although a subtle increasing trend is observed in both signals, the changes are minimal. The inconsistent and low-magnitude variations highlight the limited suitability of this method for real-time concentration monitoring.

To further explore the effects of electrode configuration, we conducted experiments in which the active surface area of the electrodes was deliberately reduced by covering part of the Orion probe (Fig. 31). These geometry manipulation tests confirmed that impedance and conductivity readings were heavily influenced by electrode surface area, which needs to be strictly controlled in any comparative study. Even small alterations in geometry had measurable effects, supporting the view that physical probe parameters are critical to data interpretation.

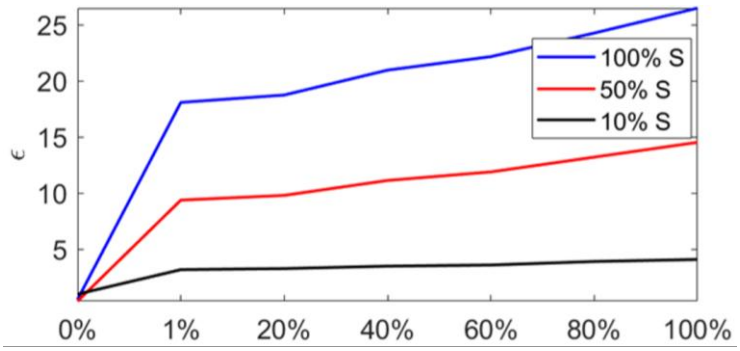

Fig. 31: Influence of electrode surface area on permittivity calculated from impedance at 400 kHz. Data are shown for three levels of exposed electrode area: 100%, 50%, and 10% surface (S). A clear drop in measured permittivity is observed with decreasing electrode area, highlighting the sensitivity of dielectric measurements to electrode geometry.

To rule out probe-specific bias, we extended the discrete cell addition experiment to five different electrode types: Orion, Sanxi, Gravity, Metrohm, and a custom T-shaped flow-cell electrode (Fig. A8). These probes varied significantly in their wiring configurations (including 2-, 3-, and 4-wire setups), construction materials, and geometric designs. In each case, yeast cells were incrementally added five times into fresh YPD medium, with real-time impedance measurements taken between additions.

Fig. 32 displays the permittivity, derived from impedance measurements of different probes at a frequency of 1.31 MHz. Due to the distinct physical configurations of the electrodes, each probe produced permittivity values on different absolute scales. Notably, some probes even displayed anomalous results such as apparent negative permittivity values an artifact likely stemming from geometrical or signal processing limitations.

Despite these discrepancies in scale and range, the primary goal of this test was not to compare permittivity values, but to evaluate whether any of the electrodes could reliably detect changes in permittivity corresponding to increasing biomass. Across all electrodes tested, no consistent or interpretable signal trend was observed in response to rising cell concentration. This consistent failure across diverse probe types suggests that the limitation lies not in the hardware or electrode construction, the principles of impedance-based measurement.

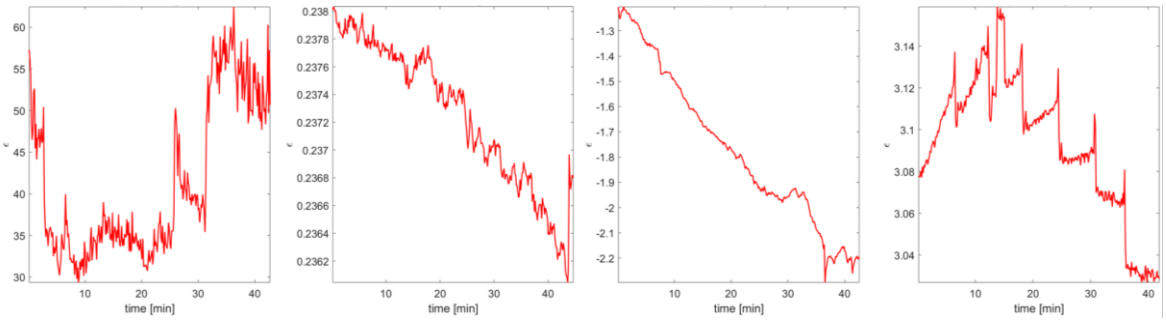

(a) (b) (c) (d)

Fig. 32: Permittivity measurements derived from impedance data at 1.31 MHz using four different electrode types: (a) Sanxi, (b) Metrohm, (c) Gravity, and (d) custom T-shaped flow-cell, during stepwise addition of yeast cells into YPD medium. Each probe displays unique permittivity scales due to differences in wiring, geometry, and material composition. Despite these variations, none of the electrodes exhibited a clear or consistent permittivity trend corresponding to increasing cell concentration, underscoring the challenge of using impedance-based methods for cell concentration estimation.

It is also important to note that impedance measurements are inherently temperature dependent. Even small variations in temperature can lead to noticeable changes in the measured impedance and derived parameters such as permittivity. Although we've significantly improved temperature regulation in our bioreactor system using an insulated chamber and PID-controlled environment, complete temperature uniformity across all experimental runs could not be guaranteed. Minor thermal fluctuations still occurred within individual measurements, and slight differences in starting conditions or ambient influences led to variability between runs. This temperature sensitivity introduces an additional layer of complexity when interpreting impedance data.

One possible explanation for the inconsistencies observed in biological experiments is linked to issues with calibration. While basic system calibration with standard resistive and capacitive loads was successful, calibration with the Orion probe was problematic. The probe, originally designed for DC conductometry, behaved unpredictably when used for broadband impedance measurements. Attempts at custom recalibration using open/short configurations with saltwater often resulted in distorted spectra, particularly at low resistances, where reliable calibration was no longer achievable. So, the default calibration setting of the impedance spectroscopy analyzer was applied. Despite this, we would still expect at least monotonic response curves with increasing concentration, which were not consistently observed even after applying relative formulas from the literature. This further indicates that the issue is not purely a calibration error but may be due to deeper limitations of the method in this specific experimental platform setting.

Although the impedance signal may partially or indirectly reflect an increase in cell concentration, the relationship remains ambiguous and not reliably quantifiable under the tested conditions. One hypothesis suggests that metabolic activity during cell growth leads to the release of extracellular compounds particularly ions that alter the conductivity of the medium. Consequently, growth might be indirectly reflected in the conductivity curve through these secondary effects on extracellular ion levels. As a result, we are currently unable to accurately quantify cell concentration based on impedance measurements alone.

7 Static Cultivation with Turbidimetry-Based Concentration Measurement

This experiment was designed as a simplified setup to minimize external influences and improve sterility. It involved:

- A minimalist configuration: no stirring and no impedance probe were used.
- Improved sterility control, achieved by using sealed vials and avoiding unnecessary instrumentation.
- A total of 10 vials (Fig. A9):
    - 5 test samples exposed to low-frequency magnetic field
    - 5 control samples not exposed to LF MF
- Additionally, 2 dilution control vials were prepared with a 10× dilution to serve as a reference for lower biomass concentration.

To allow efficient approximation of yeast cell concentration, a calibration curve was constructed by correlating turbidity measurements (in NTU) with manual cell counts using a Bürker counting chamber. A dilution series of yeast culture in YPD medium was prepared, and each dilution was measured both by a turbidimeter and manually under a microscope. The resulting dataset (Fig. A10) showed a strong linear relationship between turbidity and cell concentration across the tested range with a coefficient of determination of 0.9913 indicating an excellent fit and high predictive accuracy of the model. This strong correlation validates the use of turbidity as a proxy for estimating cell concentration, particularly in the mid-to-high density range.

It is important to note that both turbidimetric and manual Bürker chamber measurements exhibit reduced precision at lower concentrations. At low cell densities, the spatial distribution of cells is significantly less uniform, which introduces variability. In Bürker chamber counts, some counting squares may contain no cells while others may contain one or two, leading to high relative error. Similarly, in turbidimetric measurements, the lower probability of light rays encountering cells causes greater signal fluctuation and underrepresentation of actual concentration. These limitations should be considered when interpreting results in the low-concentration regime.

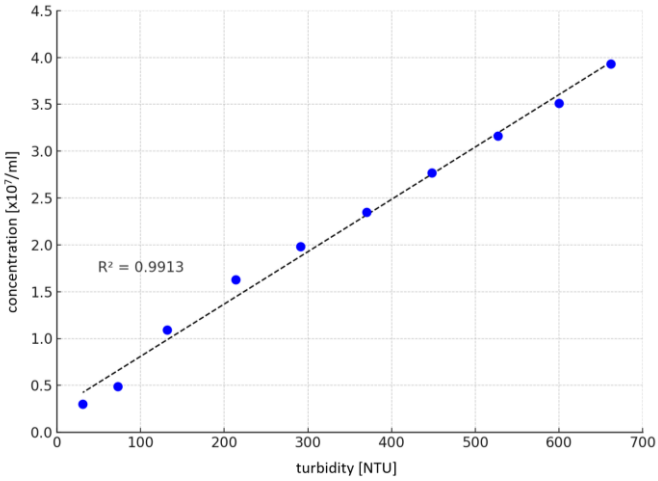

Fig. 33: Calibration curve showing the linear relationship between turbidity (NTU) and yeast cell concentration ($\times 10^7$ cells/ml). Deviations at low concentrations may occur due to non-uniform cell distribution and the reduced likelihood of cell-light interactions during turbidimetric measurements.

7.1 Optimal Starting Microbial Concentration

For the optimal experimental setup, it was necessary to identify two interdependent parameters: the initial cell concentration and the total cultivation time. Because these parameters could not be established simultaneously, they were determined iteratively. On one hand, extending the experiment's duration increases the likelihood of detecting the MF effect. On the other hand, practical considerations, such as limiting each run to a single day (24 h), impose a maximum cultivation window of about 20 hours after accounting for at least 2 hours needed for preparation and post-experiment procedures. Knowing this approximate time frame, the subsequent step involved exploring appropriate dilution levels that would allow cells to remain in the desired growth phase during the available cultivation period.

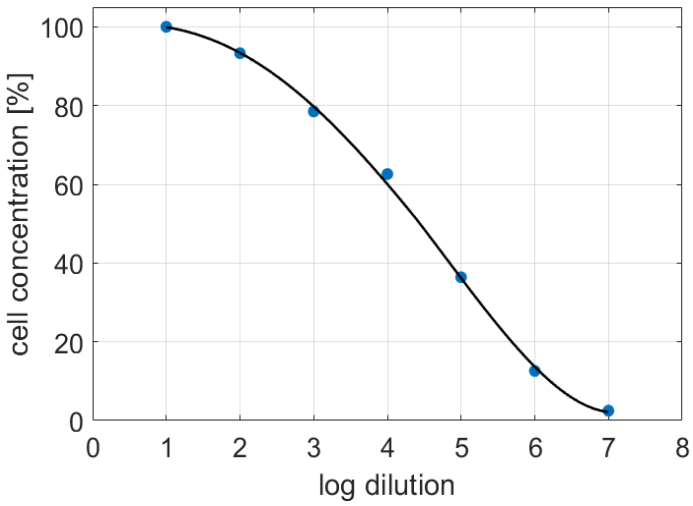

Fig. 34: Cell concentration (●) after 20 hours of cultivation as a function of the initial inoculum (5.5×10^7 cells/ml) dilution.

In the search for the optimal initial concentration of *Saccharomyces cerevisiae* CCY 21-4-99, biomass growth was first assessed after 20 hours of stationary cultivation at 35 °C as a function of the starting cell density. Biomass growth, measured turbidimetrically, was expressed as a percentage relative to the 24-hour pre-culture (Fig. 34). The data show that only the sample containing 10% of the pre-culture (i.e., a 1:10 dilution) reached a biomass equivalent to 100% of the pre-culture. By contrast, biomass growth of 50% or less was observed at dilutions exceeding $1:3.2x10^4$, indicating a marked decrease in growth. At a dilution of $1:10^7$, biomass growth was already negligible (2.2%), illustrating the sensitivity of growth to reduced initial cell density.

Our target window for final biomass growth was between 20–60%, as detecting differences in pair experiments becomes more challenging when final concentrations are either too low or too high (see explanation below and Fig. 35b). To further refine this range, we tested pre-culture dilutions from $5x10^4$ to $2x10^5$. Based on these trials, the final pre-culture concentration corresponded to a $1.8x10^5$-fold dilution of the original pre-culture (results not shown), equivalent to a calculated value of 306 cells/ml.

7.2 Modelling of Optimal Duration of Biological Experiment

To model and determine the optimal duration of biological experiments, a large-scale cultivation was performed using 84 vials of yeast culture. The vials were fully submerged in a water bath to ensure uniform temperature conditions throughout the experiment (Fig. A11).

The water bath was temperature-controlled, maintaining stable conditions for optimal yeast growth while minimizing thermal variation between samples.

For the selected initial cell concentration (306 cells/ml), the culture was cultivated in parallel in two identical thermostatic chambers, and biomass growth was monitored over time. Yeast cell concentrations were measured turbidimetrically starting at the 12th hour, with a total of 14 measurement time points. At each point, samples were collected from three vials per chamber. In this way, two growth curves were obtained simultaneously, one in each chamber. The data shown represents mean values from these two curves, fitted with a sixth-order polynomial, including an extrapolation to a single point at 36 hours (Fig. 35a).

The cell growth curve demonstrates that biomass levels remained below half of the fully developed biomass observed at 37 hours until the 19th hour. In particular, data show that the exponential growth phase extended up to the 19th hour, with biomass levels staying

below 50% of the stationary phase maximum (Fig. 35). During this early growth period, biomass doubling occurred within approximately 2 hours or less. Such a growth curve is characteristic of stationary cultivation, where cells grow at the bottom of the vials without mixing or agitation.

Next, it was necessary to determine a specific time point at which to halt the experiment. For this purpose, mathematical modeling was employed. The primary criterion was to select a time providing the best chance to observe differences between growth under the MF condition and the control. The MF effect was simulated by shifting the entire growth curve in time, either to the left (stimulation) or to the right (inhibition); however, the direction is not crucial in this context. In Fig. 35b, the blue curve illustrates the inhibition scenario, with the growth process delayed by 2 hours compared to the original red curve.

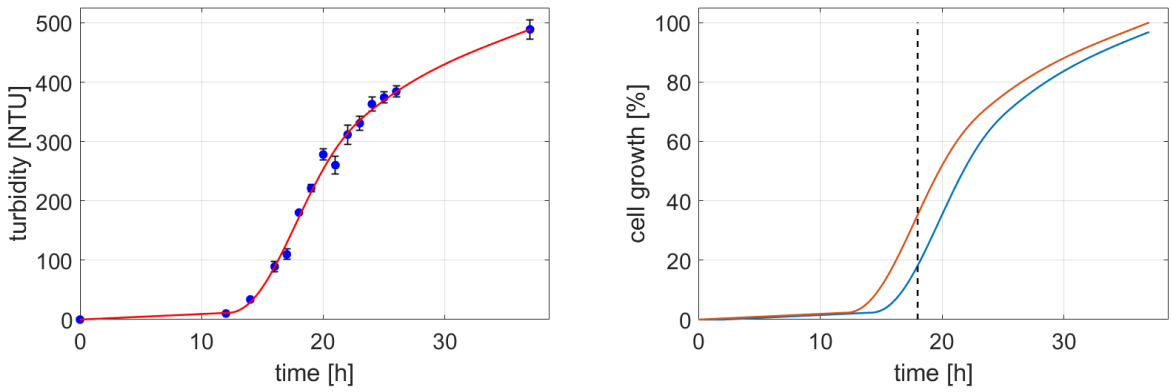

(a) (b)

Fig. 35: (a) Growth curve illustrating the increase in cell concentration of Saccharomyces cerevisiae CCY 21-4-99 over time at 35 °C. (b) Simulation of MF impact by delaying growth by 2 hours (blue curve). The vertical line at 18 h indicates the moment of maximum difference between the two growth curves

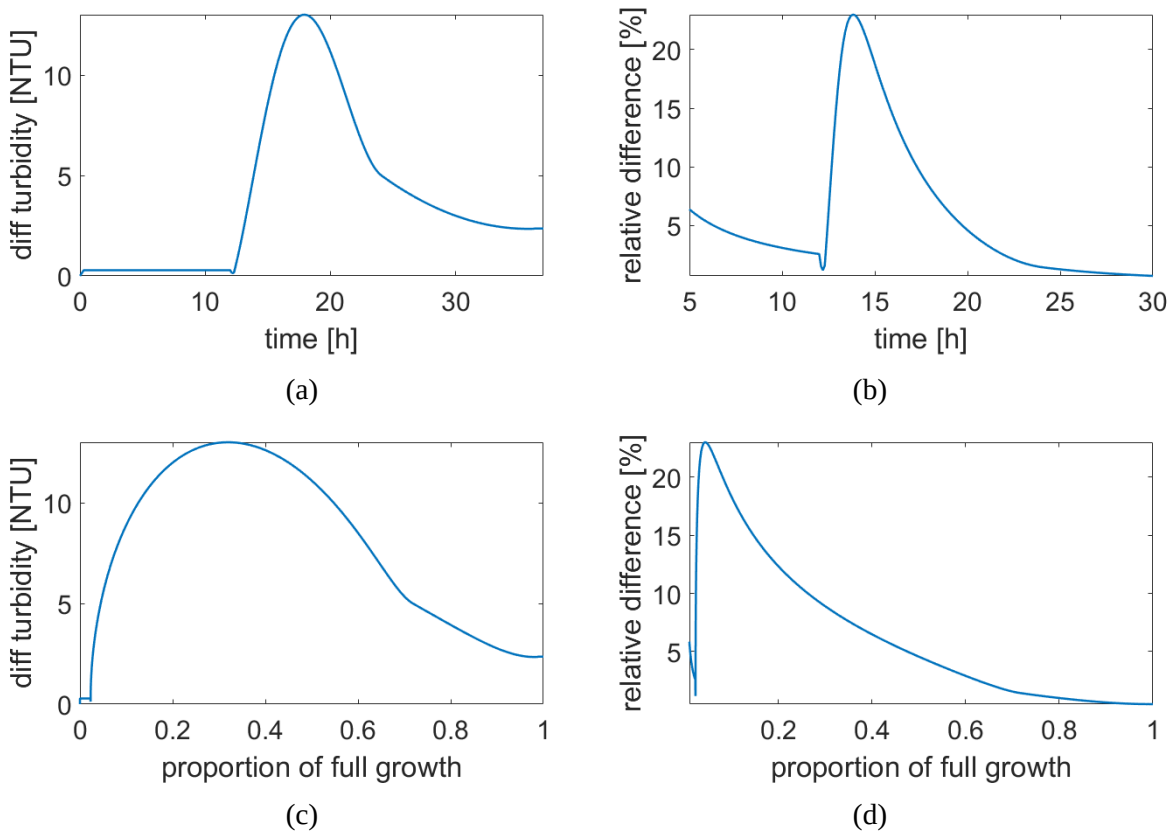

Fig. 36: (a) Absolute difference in turbidity over time between the original and MF-shifted growth curves. (b) Relative difference in turbidity over time. (c) Absolute difference in turbidity as a function of normalized growth progression. (d) Relative difference in turbidity as a function of normalized growth progression.

To determine the most appropriate time point for assessing the impact of low-frequency magnetic fields on yeast growth, a simulation was performed based on temporal shifts of the growth curve. Fig. 36 presents a detailed analysis of the difference between the original (red) and simulated MF-affected (blue) growth curves shown in Fig. 35b. The absolute difference in turbidity between the two curves is plotted over time (Fig. 36a), revealing a peak at approximately 18 hours. Fig. 36b shows the relative difference over time, calculated as the ratio of the absolute difference to the value of the control (red) curve. Although the relative difference reaches its maximum earlier, the absolute difference at 18 hours is more relevant for practical measurements.

The bottom panels reframe this comparison against the normalized proportion of maximum cell concentration. In Fig. 36c, the absolute difference peaks at around 33% of the full growth level, while Fig. 36d shows that the relative difference is highest at an even lower growth fraction. However, due to the limitations of measurement precision at very low concentrations, especially in the early lag phase, these early time points are less suitable for

reliable quantification. At early stages, the cell distribution is highly uneven in both Bürker chamber counts (e.g., sometimes 0 or 1 cell per square) and turbidimetric readings (as light may pass through without encountering cells).

Therefore, selecting 18 hours corresponding to ~33% of the maximum concentration as the measurement point balances the need for significant detectable differences with practical measurability. This corresponds to an estimated concentration of approximately 1.82×10^7 cells/ml after undergoing approximately 16 doubling events, a range suitable for both turbidimetric and manual cell count methods.

7.3 Verifying Pair Experimental Design

A key objective during the development of our experimental platform was to address the methodological limitations identified in the literature review, as summarized in Tab. 2. These included the lack of precise temperature control and monitoring, absence of cross-over or pair control designs, and inconsistent environmental regulation between test and control groups. In response, we successfully implemented a system that incorporates dual, independently monitored cultivation chambers, cross-over capability, and real-time temperature tracking for both samples. This section presents the validation of these design features through a series of pair experiments that confirm their robustness and reproducibility.

In this section, we present the proof of concept for the developed experimental platform. The pair experiment was conducted over 18 hours, with five test sample vials placed in each chamber and operated under two modes: (1) both chambers under control conditions without MF, and (2) both chambers exposed to a 50 Hz MF of 3.5 mT, driven by an electrical current of 4.5 A. Throughout the experiment, the temperature in both cultivation chambers was maintained at 35 °C.

From each experimental run, environmental conditions were evaluated using three parameters: the mean temperature in chamber 1, the mean temperature in chamber 2, and the mean temperature difference between the two chambers. Only experimental runs that met the following three temperature criteria were included in further analysis: the mean temperature in chamber 1 and in chamber 2 had to remain within 35±0.3 °C, and the mean temperature difference between the chambers had to be within ±0.3 °C.

In Fig. 37: Boxplots for cell concentration difference between cultivated cultures in two chambers.

C-C: both chambers in control mode without MF (N = 5). T-T: both chambers in test mode with MF (N = 5). Combined: merged data from the two previous sets (N = 10)., the cell concentration difference between cultures in the two chambers in a pair experimental setup is illustrated using boxplots for three data sets: simultaneous operation of both chambers in control mode with MF switched off (N = 5), both chambers in test mode with MF switched on (N = 5), and a combined set merging the previous two (N = 10). In all three cases, the mean difference in cell growth between the two chambers remained below 1%. Statistical analysis using a one-sample t-test did not reject the hypothesis that the mean values of these sets were equal to zero (p-values = 0.56, 0.78, and 0.52, respectively). These findings indicate that the two chambers provide sufficiently consistent conditions for cell growth within the given experimental settings.

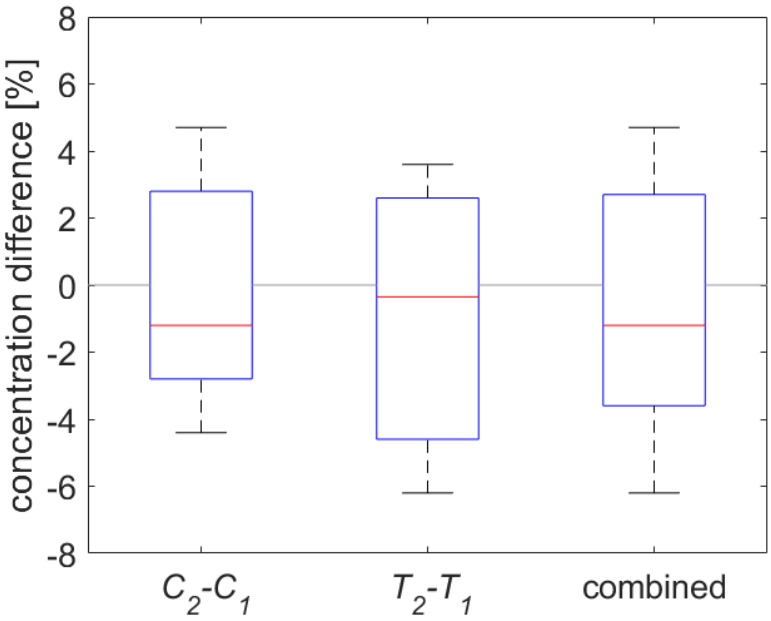

Fig. 37: Boxplots for cell concentration difference between cultivated cultures in two chambers.
C-C: both chambers in control mode without MF (N = 5). T-T: both chambers in test mode with MF (N = 5). Combined: merged data from the two previous sets (N = 10).

The experimental platform was specifically designed to overcome critical challenges commonly encountered in studies investigating LF MF effects on biological systems. A cornerstone of the platform design is the ability to maintain tightly controlled and reproducible experimental conditions through the integration of standardized or customized components.

Temperature regulation and monitoring are particularly important, as even minor fluctuations can significantly affect biological responses regardless of MF exposure. A deviation of as little as 1 °C can significantly affect biological growth and potentially lead to the effects being misattributed to MF exposure. In contrast to the detailed temperature management protocols presented in this study, most previous research has paid insufficient attention to this critical variable.

To ensure accurate temperature control in the present study, the sensors were directly immersed in the water bath containing the biological samples, allowing for real-time, localized temperature measurement. This configuration also helps to mitigate the thermal gradients generated by active components such as Helmholtz coils and heating elements, which could otherwise affect the environmental uniformity. Careful optimization of the chamber architecture further minimized these thermal disturbances.

Although the authors of numerous studies speak of satisfactory thermal control, they often lack quantitative evidence, such as a statistical characterization of the temperature time series or direct comparisons of measured temperatures between test and control locations. Of the relevant studies that investigated the effects of 50/60 Hz MF on biological systems ([2]-[4], [8], [14], [25], [45]), only two ([2], [44]) monitored temperature at both test and control sites. Of these studies, only one ([2]) provided quantification, and even this was limited to reporting a temperature range with no mean values or standard deviations. As a result, none of the reviewed studies reported the actual measured temperature differences between the experimental groups. In addition, none of the studies performed internal consistency checks, such as control-control or test-test comparisons, to confirm that the pair setups provided equivalent conditions. Similarly, no crossover design was used in any study to eliminate potential site-specific biases between the pair systems.

The temperature monitoring integrated into our experimental platform also showed exceptional thermal stability throughout the experimental runs. Variations within and between chambers remained minimal, ensuring a consistent and uniform environment for all biological samples. The simultaneous operation of both chambers further confirmed their suitability for high-precision, reproducible pair experiments.

In our study, we used a single-wrapped coil design, which results in an asymmetry in heat generation due to the active coils in the test chamber. However, we ensured thermal symmetry between both chambers through PID temperature regulation, precise temperature

monitoring, and the exclusion of experimental runs that did not meet strict temperature uniformity criteria. In principle, a double-wrapped coil configuration could mitigate heating by balancing the current flow, with both the control and test conditions carrying the same current but in opposite directions (anti-parallel in one case, parallel in the other), resulting in equivalent heat generation.

The operation of electromagnetic coils is often associated with mechanical vibrations that can affect sensitive biological experiments. Both coil configurations, single- and double-wrapped, are subject to this vibration phenomenon [47]. In both cases, the vibrations occur when a non-zero resulting MF is present, i.e. during exposure of the test sample. When a double-wrapped coil is fed with antiparallel currents, resulting in a zero magnetic field (which corresponds to our "control" condition), no vibrations are observed [47], similar to our system's control state, where the coils are turned off. This shows that we are not able to create identical vibration conditions for the "magnet on" and "magnet off" states.

In agreement with the above, a faint buzzing noise was observed during coil operation in our setup, indicating the presence of low-level vibrations. However, the microbial culture vials were located in water baths housed in larger beakers, which helped to partially attenuate the mechanical vibrations transmitted by the coils. In addition, the yeast cells used in the experiments consistently settled at the bottom of the vials during incubation, regardless of whether MF was switched on or off. This indicates that the vibrations were not sufficient to resuspend the cells and noticeably improve their access to nutrients and oxygen, factors that could otherwise have a noticeable effect on biomass growth.

The yeast strain Saccharomyces cerevisiae CCY 21-4-99 was selected as the model organism for this study due to its unique and advantageous characteristics. This non-pathogenic, thermotolerant strain thrives at an optimal growth temperature of 35 °C, which coincides with the operating temperature range of the experimental platform. Its eukaryotic cell structure provides a relevant model for the study of biological processes similar to those in higher organisms, offering distinct advantages over prokaryotic models such as bacteria.

Mathematical modelling and growth rate analyses were used to determine the optimal duration and initial cell concentration of Saccharomyces cerevisiae CCY 21-4-99, ensuring that cells remained in the growth phase during MF exposure. Keeping the cells in a physiologically active state is critical for two reasons: it increases their responsiveness to

MF exposure and minimizes confounding factors such as cellular aging and deceasing viability.

In the final tests, growth differences between the Saccharomyces cerevisiae CCY 21-4-99 cultures in the two chambers were minimal and statistically insignificant, demonstrating the technological readiness of the platform for precise and reliable pair experiments. In addition, the platform allows simultaneous exposure of multiple samples in a single run. However, the use of stationary cell cultures is a potential limitation, as these conditions differ from stirred or agitated cultures and potentially affect nutrient distribution and aeration.

Although we used a specific yeast strain in this study, the platform can be similarly applied to various prokaryotic or eukaryotic microorganisms, as well as subcellular components such as enzymes. Furthermore, the whole approach can be technically adapted to different experimental requirements, including modifications to different electro-magnetic field sources (such as permanent magnets), temperature regulation, stirring, or cell concentration monitoring.

8 Effect of 50 Hz Magnetic Field on Saccharomyces Cerevisiae Growth

The results presented in this chapter originate from the experimental setup described in chapter 7, which used static cultivation in sealed vials combined with turbidity-based cell concentration measurement.

Data from four types of pair experimental setups were collected for analysis: control vs. control, test vs. test, test vs. control, and control vs. test, with chamber assignment order relevant in the latter two cases. In total, 58 experiments were conducted, each with a duration of 18 hours. To ensure reliable comparisons, only those experiments that met strict thermal criteria were included in the final analysis.

For each experimental run, environmental conditions were evaluated based on three parameters: the mean temperature in cultivation chamber 1, the mean temperature in cultivation chamber 2, and the mean temperature difference between the two chambers. Only runs meeting all of the following criteria were included in the final analysis: the mean temperature in both chambers had to be within 35 ± 0.3 °C, and the inter-chamber temperature difference had to remain within ±0.3 °C. These thresholds were essential, as the complete dataset included temperature deviations of up to 1.35 °C, levels at which the results could no longer be considered reliable due to the known temperature sensitivity of yeast cell growth.

The $\pm$ 0.3 °C limit was chosen as a practical trade-off between the stability capabilities of the experimental platform and the need to retain a sufficient number of datasets for meaningful statistical analysis. Of the 58 total experimental runs, 24 fulfilled these criteria: 12 under control conditions (6 control vs. control and 6 test vs. test) and 12 under test conditions (6 test vs. control and 6 control vs. test). While the results presented in this paper are based on the strictest threshold ($\pm$ 0.3 °C), we also examined alternative cutoffs of $\pm$ 0.4 °C and $\pm$ 0.5 °C. These produced comparable outcomes with respect to the statistical findings discussed below.

Fig. 38 presents a comparison of temperature conditions in the two cultivation chambers as time series for all four experimental setup variants: control vs. control, test vs. test, test vs. control, and control vs. test. The time evolution of the mean temperature difference between the chambers, accompanied by SEM error bars, reveals oscillations

fluctuating around or near zero. Notably, during the initial 2–3 hours of the experimental runs, the temperature differences were slightly elevated compared to the remainder of the cultivation period, due to thermal stabilisation processes following sample insertion.

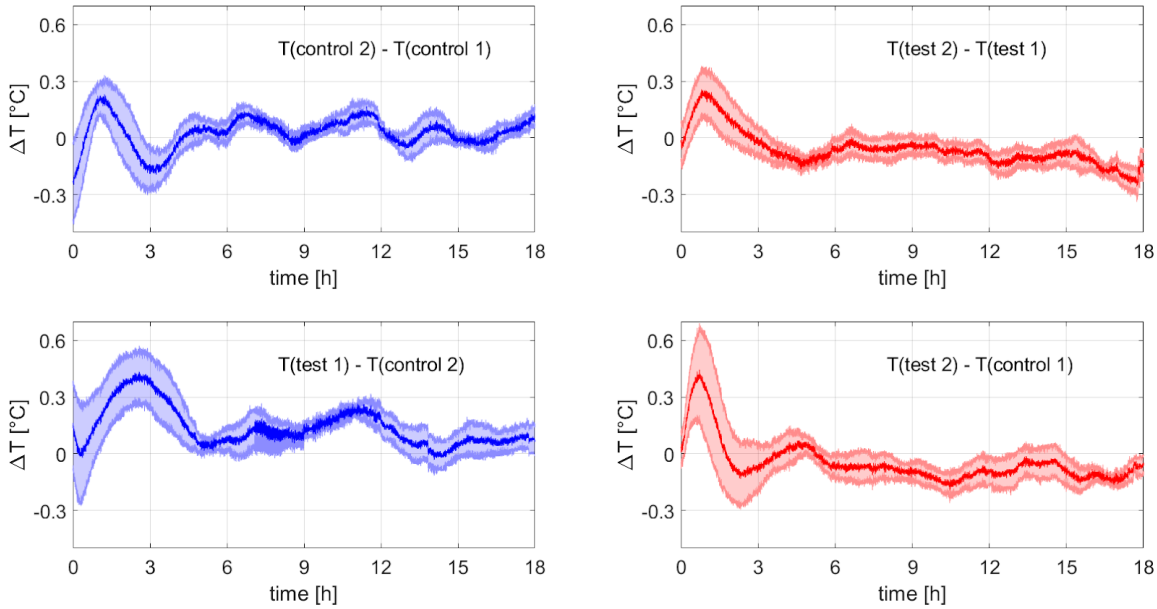

Fig. 38: Mean temperature differences with shaded error bars (±SEM) between two cultivation chambers during 18-hour pair experiments. Four different setups are presented (all with N = 6): (a) both chambers under control conditions (MF off), (b) both chambers under test conditions (MF on), (c) test conditions in chamber 1 while control in chamber 2 (d) test conditions in chamber 2 while control in chamber 1

The outcome of each of the four types of experimental setups was calculated as follows:

$$C_2 - C_1: \frac{turbidity(C_2) - turbidity(C_1)}{(turbidity(C_1) + turbidity(C_2))/\,2} \qquad \text{Eq. 8.1}$$

$$T_2 - T_1: \frac{turbidity(T_2) - turbidity(T_1)}{(turbidity(T_1) + turbidity(T_2))/\,2} \qquad \text{Eq. 8.2}$$

$$T_1 - C_2: \frac{turbidity(T_1) - turbidity(C_2)}{turbidity(C_2)} \qquad \text{Eq. 8.3}$$

$$T_2 - C_1: \frac{turbidity(T_2) - turbidity(C_1)}{turbidity(C_1)} \qquad \text{Eq. 8.4}$$

In this notation, C_2 - C_1 refers to an experimental setup with both chambers unexposed to the MF, T_2 - T_1 represents both chambers exposed to MF, T_1 - C_2 indicates MF exposure in chamber 1 while chamber 2 remains unexposed, and T_2 - C_1 represents MF exposure in chamber 2 while chamber 1 remains unexposed.

Fig. 39a shows boxplots of the relative differences in cell concentration between cultures grown in the two chambers for each of these four experimental configurations. Each condition includes six independent experimental runs, with each run comprising five dependent replicates (vials).

Cells exposed to the MF in chamber 1 (T_1 - C_2) exhibited, on average, a 1.4 % higher growth compared to the corresponding chamber under control conditions, based on merged data from C_1 - C_2 and T_1 - T_2 setups (Fig. 3b). In contrast, when the MF was applied in chamber 2 (T_2 - C_1), cell growth decreased on average by 2.8 % relative to the reversed control conditions (derived from C_2 - C_1 and T_2 - T_1) (Fig. 3c). These comparisons were based on 12 measurements for control conditions (6 for *C vs. C* and 6 for *T vs. T*) and 6 measurements for each of the test conditions (T_1 - C_2 and T_2 - C_1, respectively).

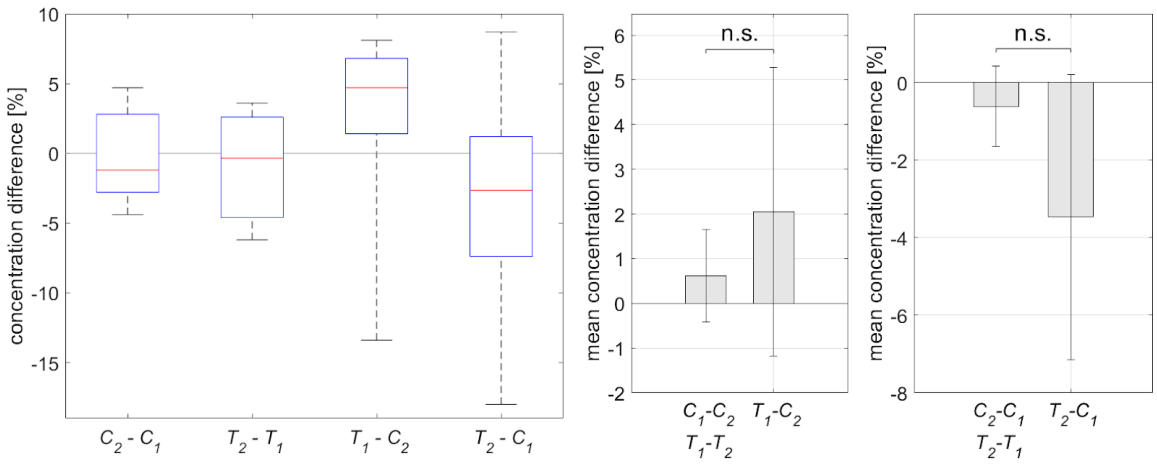

(a) (b) (c)

Fig. 39: (a) Boxplots showing the relative differences in cell concentration between cultures grown in the two cultivation chambers across four different experimental setups (N = 6 for each setup). (b) Mean cell concentration difference between chambers in the pair experimental setup for the case of combined control conditions (C_1 - C_2 and T_1 - T_2) and MF applied in chamber 1 (T_1 - C_2). (c) Mean cell concentration difference for the case of combined control conditions (C_2 - C_1 and T_2 - T_1) and MF applied in chamber 2 (T_2 - C_1, N = 6). Error bars represent ± SEM

To address whether the observed differences could reflect genuine MF-induced effect or merely represent negligible statistical variation in the absence of any real effect, statistical analysis was conducted. Even without formal testing, it is apparent that no consistent effect

was present - stimulation in one chamber accompanied by inhibition in the other would contradict itself and thus cannot indicate a reliable MF response.

The statistical analysis approach was not straightforward and involved several variants. For the pair experimental design used in this study, standard two-sample comparisons between MF exposure and control conditions required careful consideration. Specifically, MF exposure occurred in two distinct configurations: chamber 1 (T_1 - C_2) and chamber 2 (T_2 - C_1). Similarly, two types of control configurations were used: control-control (C_2 - C_1) and test-test (T_2 - T_1). These two control datasets could be merged into a single control group due to their structural similarity.

However, this was not the case for the MF exposure conditions. T_1 - C_2 data had to be compared only to C_2 - C_1 and T_2 - T_1, as did T_2 - C_1, but with opposite ordering of chamber data: C_1 - C_2 and T_1 - T_2. This distinction was essential because the controls rarely produced an exact zero difference in cell growth between chambers. Thus, both T_1 - C_2 and T_2 - C_1 comparisons involved control data with small but non-zero mean values. In such cases, the sign (i.e., directionality) of these mean differences becomes important for statistical testing. Consequently, although the same control dataset is used in both cases, the comparisons must preserve the correct chamber assignment and ordering.

As a result, it is not statistically valid to apply a single two-sample t-test across the combined MF dataset (T_1 - C_2 and T_2 - C_1) because their associated control comparisons have opposing signs and directional implications. Each MF configuration must be evaluated separately against appropriately ordered controls.

However, there does exist a way that enables combining all the data together. By shifting T_1 - C_2 and T_2 - C_1 data by their respective control means. By constructing T_1 - C_2 - mean (C_1 - C_2, T_1 - T_2) and T_2 - C_1 - mean (C_2 - C_1, T_2 - T_1) one accounts for possible small effects arising from box differences. Then, a one-sample t-test can be applied to test whether the mean of such adjusted MF samples differs significantly from zero.

The choice between parametric and nonparametric testing was guided by normality assessment. In cases where the assumption of normality was rejected, the Wilcoxon rank-sum test (for two-sample comparisons) or the Wilcoxon signed-rank test (for one-sample comparisons) was used instead of the corresponding t-tests. As shown in Tables 2 and 3, normality was rejected only for the MF in the chamber 1 dataset, along with its temperature-

corrected version. However, the validity of normality tests for small sample sizes ($N = 6$ and 12 in our case) is debatable, as their low statistical power may make it difficult to reject the normality assumption. Therefore, Tab. 8 and Tab. 9 report *p*-values for both parametric and nonparametric tests to provide a more comprehensive view. Temperature-corrected cases that are also present in these tables are addressed in the following section.

In all statistical tests, whether parametric or nonparametric, the effect of MF was found to be insignificant, both in the two-sample comparisons (Tab. 8, last two rows) and the one-sample approach (Tab. 9, last two rows). Specifically, all *p*-values ranged from 0.15 to 0.91, with none falling below the conventional significance threshold of 0.05. This consistent outcome across different testing strategies supports the conclusion that, under the conditions of this study, exposure to a 50 Hz, 3.5 mT low-frequency MF within the temperature of 35 ± 0.3 °C, had no measurable effect on yeast cell growth.

Tab. 8: Statistical analysis of MF effects using both parametric and nonparametric methods for the two-sample comparison. The control group combines *C* vs. *C* and *T* vs. *T* conditions (as shown in Fig. 3), while test groups represent asymmetric MF exposure in pair setups. The last three columns present test outcomes after adjustment based on temperature correction.

p-value	control	MF in chamber 1	MF in chamber 2	temperature-corrected		
				control	MF in chamber 1	MF in chamber 2
Shapiro-Wilk normality test	0.60	0.019	0.95	0.71	0.016	0.92
Independent two-sample t-test	-	0.6	0.34	-	0.55	0.32
Wilcoxon rank sum test	-	0.17	0.49	-	0.15	0.44

Tab. 9: Statistical analysis of MF effects using both parametric and nonparametric methods for the one-sample comparison. In this approach, MF-exposed conditions (T_1 - C_2 and T_2 - C_1) were adjusted by subtracting the corresponding control means to account for baseline chamber differences and tested against zero mean

	MF in chamber 1 + MF in chamber 2	MF in chamber 1 + MF in chamber 2, temperature corrected
Shapiro-Wilk normality test	0.22	0.21
One-sample t-test	0.78	0.78
Wilcoxon signed rank test	0.91	0.91

Subsequently, we conducted a more detailed investigation to determine whether certain experimental factors may have had a significant influence on the outcomes. For this purpose, we employed correlation analysis. The results (Fig. 40a) indicate that strong correlations were observed only among naturally related variables, specifically, temperatures with each other and turbidities with each other. However, both temperatures T1 and T2 were weakly anticorrelated with their respective turbidity measurements, suggesting that the strain's optimal growth temperature may lie below 35 °C.

These findings prompted a closer examination of temperature corrections related to cell growth. Aside from this, it is well established that yeast cell growth is strongly dependent on temperature. We verified this temperature sensitivity curve and found out that our working temperature of 35 °C is close to the optimal growth temperature for this strain. Under such conditions, a temperature difference of 0.3 °C or even 0.5°C between the chambers may not have a significant effect. Nevertheless, it was reasonable to test this possible dependence, and in the case of even a small effect, to apply a temperature correction and assess whether it would alter the results.

Since the effect appeared to be absent or negligible, we applied a linear temperature correction using the entire dataset - including both control and test runs. The correction was performed within two temperature ranges: a narrow range of 35 ± 0.3 °C and a broader range 35 ± 1.5 °C based on all experimental runs after exclusion of outliers (Fig. 40b). In Tab. 10, these corrections are expressed per temperature unit and per 0.3 °C, as the value of 0.3 °C was a natural temperature scale in this experiment. It was a trade-off between maximally

controllable and reproducible environmental conditions influenced by technological limitations for temperature stabilization, while remaining a sufficient number of experimental runs satisfying these temperature criteria for statistical analysis.

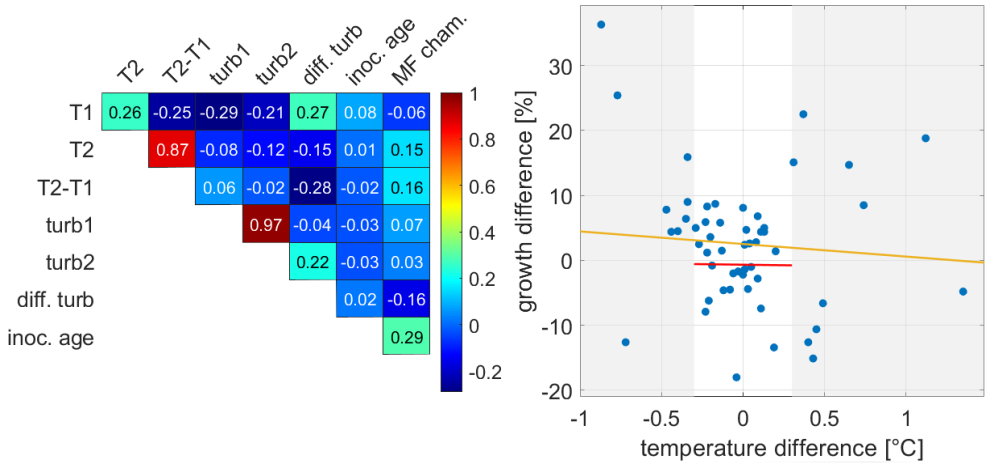

(a) (b)

Fig. 40: (a) Correlation heatmap. T1, T2 - temperature in cultivation chambers 1 and 2, turb1, turb2 - turbidity in chamber 1 and 2, diff. turb - turbidity difference, inoc. age - inoculum age. (b) Dependence of cell growth difference between chamber 2 and 1 on the temperature difference between chamber 2 and chamber 1. Two regression lines are depicted: yellow - from all data points, with a slope -1.94 % / °C, red - only from data points satisfying strict criteria on temperature (mean T in chambers 1 and 2 equalled to 35 ± 0.3 °C, and mean T difference between chambers equalled to 0 ± 0.3 °C) with temperature correction of -0.33 % / °C

While a temperature correction of −0.33 % / °C was obtained for the narrow temperature range, this value increased to −1.94 % / °C when a broader interval was considered. However, the corresponding regression models exhibited low coefficients of determination (R^2), indicating limited explanatory power. Moreover, the slopes in both cases were statistically indistinguishable from zero, suggesting no significant temperature-dependent trend. Next, the statistical analysis was recalculated with these two temperature corrections. As no significant shifts appeared within the data, the statistical outcomes remained still insignificant (Tab. 8 and Tab. 9, the last columns).

Tab. 10: Correction of MF effect obtained by linear regression from two different datasets (in columns). Rows: Correction expressed per unit temperature and per 0.3 °C

temperature correction of MF effect [%]	subset satisfying strict temperature criteria	whole dataset
correction per 1 °C	-0.33	-1.94
correction per 0.3 °C	-0.1	-0.58

We observed no measurable effect, in contrast to a number of previous studies that have reported both positive and null outcomes. Although the majority of published research suggests some influence of ELF magnetic fields, the reported effects are highly variable and often contradictory, making it difficult to identify consistent patterns. Furthermore, many of these findings have not been independently verified, and replication attempts frequently produce conflicting results, underscoring the inherent challenges in reproducing subtle biological responses to ELF magnetic field exposure.

It is well established that studies reporting positive findings are more likely to be published than those reporting null results (i.e., absence of effects) [9]. In addition, various forms of bias may influence research outcomes, collectively indicating that the true frequency of null findings is likely underrepresented in the literature. Our study contributes to this ongoing discussion by prioritizing methodological rigor, strict environmental control, and a carefully designed experimental protocol. Drawing from our direct experience with the challenges of reproducibility and sensitivity to uncontrolled variables, we suspect that a substantial portion of previously reported effects may reflect experimental artefacts rather than genuine biological responses. According to our qualified guess, unnoticed temperature differences might be one of the main sources leading to reporting false positive effects.

9 Pulsed Electric Field Effect on Yeast Cells Measured by Autoluminescence and Impedance Measurements

In contrast to the inconclusive results obtained in chapter 6, where impedance spectroscopy did not yield consistent or monotonic trends for cell concentration estimation in our published study, see Bereta et al.(2024) [43], demonstrates a successful application of impedance methods. Conducted in collaboration with the Faculty of Health Sciences, Catholic University in Ruzomberok (Slovakia); the Institute of Measurement Science, Slovak Academy of Sciences (Bratislava, Slovakia); the WPI Nano Life Science Institute, Kanazawa University (Japan); and particularly with the BIOEM team led by Michal Cifra at the Institute of Photonics and Electronics, Czech Academy of Sciences (Prague, Czechia), this research employed a carefully optimized setup tailored for electroporation experiments in yeast. These findings highlight that, while our system faced limitations due to environmental and instrumental constraints, impedance spectroscopy remains a powerful technique under well-controlled experimental conditions.

Introduction

Pulsed electric fields (PEFs) are gaining traction as a valuable technique in biotechnology and the food industry. Nevertheless, real-time assessment of PEF efficiency remains a major hurdle, particularly under continuous production and large-scale conditions.

To address this issue, we designed a simple experimental system enabling real-time monitoring of biological autoluminescence (BAL) emitted by Saccharomyces cerevisiae during PEF application. The yeast suspension was subjected to 8 electric pulses, each lasting 100 µs, across a range of electric field strengths from 2 to 7 kV/cm (Fig. 41).

To evaluate the detection sensitivity of our approach, we benchmarked it against several established techniques: impedance spectroscopy, propidium iodide (PI) staining, fluorescence microscopy, and post-treatment growth assays.

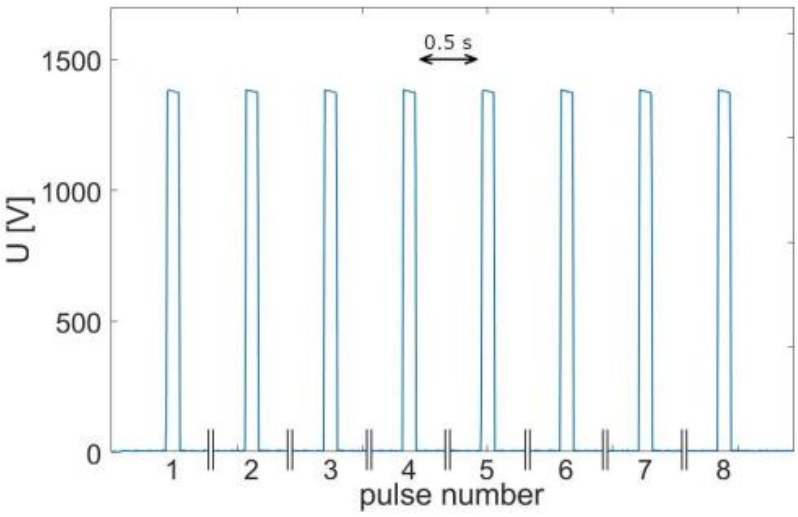

Fig. 41: Shape of voltage signal pulses (1400 V) for the case of electric field strength equal to 7 kV/cm. Axis breaks between the neighbouring pulses indicate cut time windows to see pulses more clearly. The pulses were separated by 0.5 s

Methods

The specialized measurement system setup shown in Fig. 42 consists of a PEF chamber placed within a light-tight housing to allow sensitive detection of biological autoluminescence. The chamber includes a sample holder between two electrodes (anode and cathode), with electrical pulses applied via a voltage pulse generator. A photomultiplier tube (PMT) is positioned above the sample to detect light emission, and the signal is subsequently processed through a counting unit and recorded on a PC. Simultaneously, current and voltage probes allow for real-time monitoring of pulse parameters using an oscilloscope.

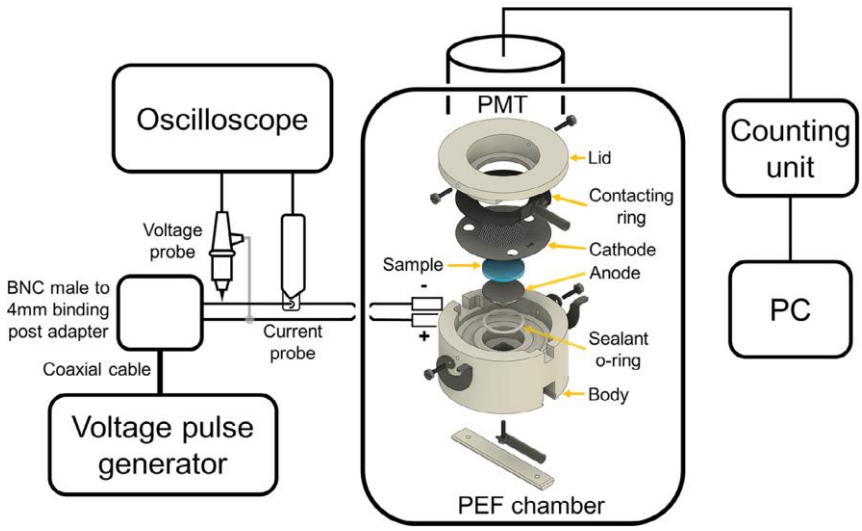

Fig. 42 A schematic diagram of the experimental setup for measuring luminescence during and after PEF treatment in the dedicated chamber. The PEF chamber is enclosed in a light-tight chamber to enable detection of the luminescence using PMT.

Impedance analysis

To assess the electrical properties of yeast suspensions before and after pulsing, impedance was measured over the frequency range of 30 Hz to 300 kHz using a two-electrode setup (BK891, BK PRECISION). Measurements were performed directly within the same chamber used for PEF application. Simultaneously, we recorded the amplitude of current pulses delivered by the ELECTROcell B15 pulse generator (Leroy-Biotech) to characterize the energy input into the samples.

For further analysis, we focused on the absolute impedance values at 50 kHz, a frequency chosen to represent the effective conductivity of the sample while avoiding the influence of electrode polarization, which dominates at lower frequencies in two-electrode systems. The change in impedance due to electroporation was quantified by subtracting the post-pulse values from the pre-pulse measurements.

Assessment of membrane permeabilization

Cell membrane permeabilization was evaluated through propidium iodide (PI) uptake, assessed by two complementary methods: fluorescence microscopy for qualitative visualization and fluorescence intensity quantification using a microplate reader for quantitative analysis.

Absorbance-based cell growth monitoring

Cell proliferation was tracked by measuring optical density at 600 nm in a 96-well plate format over a 24-hour period at 30 °C using a Tecan Spark microplate reader. For quantitative comparison of growth kinetics, we defined the time point at which each absorbance curve reached 95% of its peak value as a characteristic indicator of growth progression.

Results

Detection of Electroporation Threshold and Evaluation by Complementary Methods

Biological autoluminescence (BAL) measurements indicated a threshold for electroporation between 6 and 7 kV cm^{-1} (Fig. 43). Fluorescence analysis revealed a significant increase in the proportion of PEF-affected cells starting at 5 kV cm^{-1} (Fig. 44). The impedance data (Fig. 45A) show the difference between measurements taken before and

after a sequence of eight PEF pulses. All three methods exhibited a consistent trend of increased electroporation with rising electric field strength. Notably, a marked alteration in membrane permeability was consistently observed around 5 kV cm^{-1}. The observed increase in impedance changes correlates with enhanced effective conductivity of the medium, attributed to electroporation of the cell membrane and wall, followed by the release of intracellular ions into the surrounding medium.

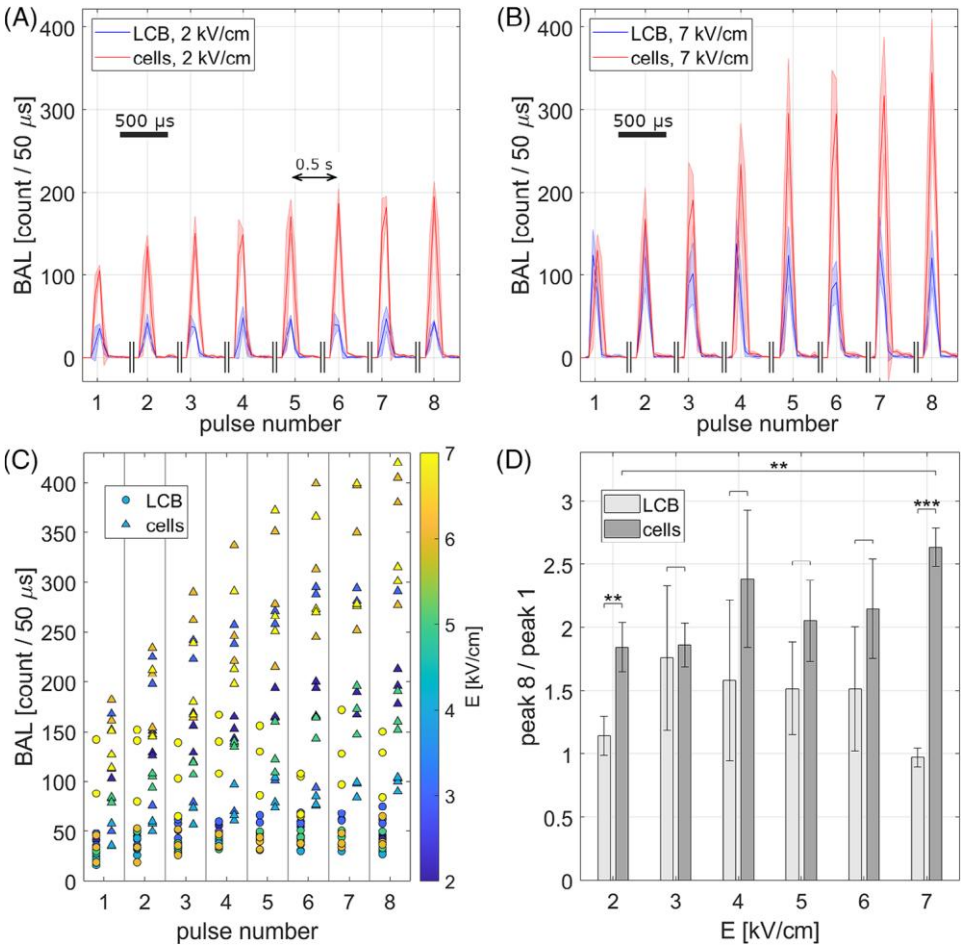

Fig. 43: BAL signal during yeast electroporation. (A), (B) BAL signal during the sequence of pulses with 2 and 7 kV cm−1 electric field strength (means from 3 repetitions together with colored intervals formed by ± SD). Thewidth of each pulsewas 100 µs, and the gaps between the successive pulses were 0.5 µs. Between the neighboring pulses time windows were cut to see pulses more clearly. (C) Scatter plot of BAL for six electric field strengths during a sequence of 8 pulses for both cells and only LCB buffer. (D) The ratio of BAL obtained during the last 8th pulse with respect to the value measured during the first pulse. Two types of statistical comparison: (1) the condition with the lowest electric field strength to all the other conditions, separately for LCB and cells (only a significant pair is linked), (2) cells versus buffer for each condition (all pairs are linked). Data are presented in the form of means ± SD; t-test: **$p < 0.01$, ***$p < 0.001$.

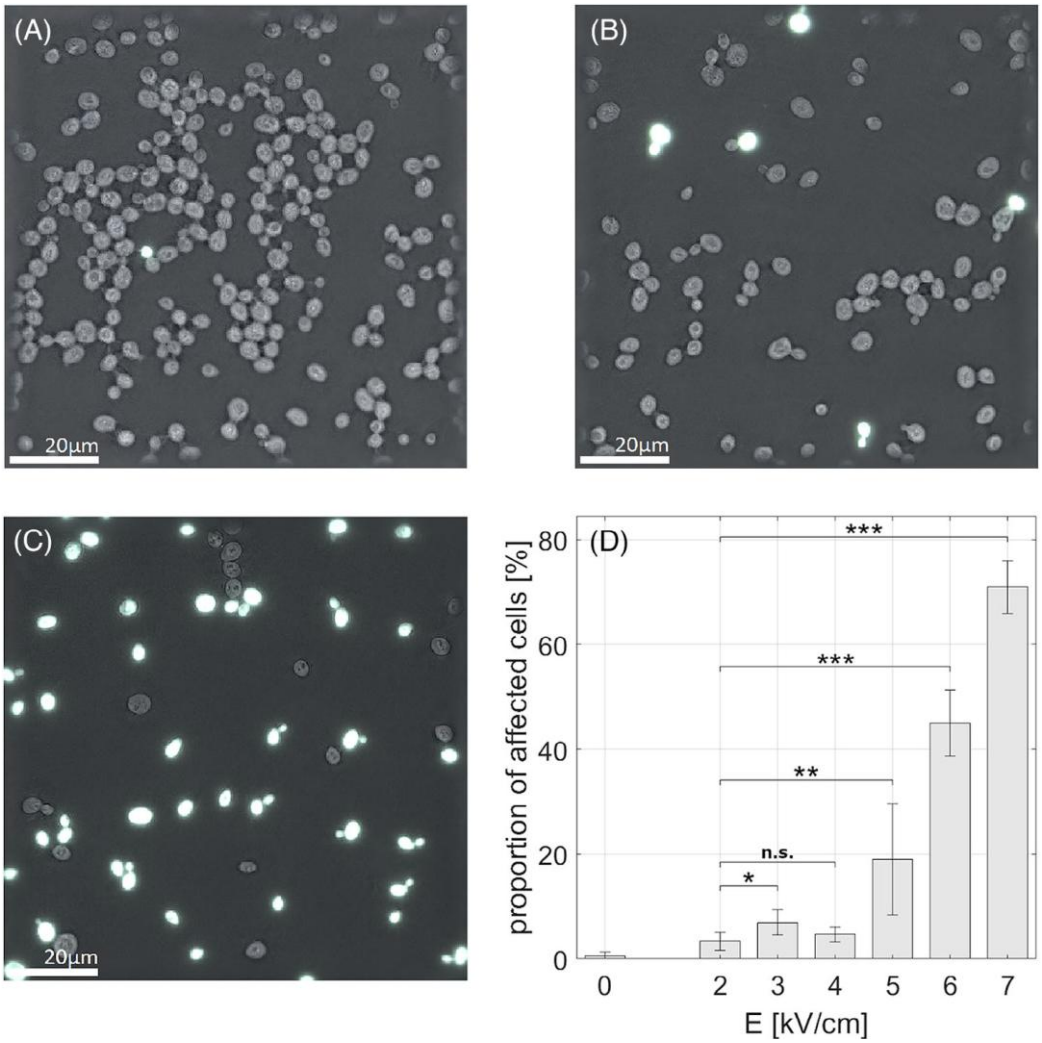

Fig. 44: Propidium iodide uptake – combined PI fluorescence image and single plane from holography (refractive index contrast-based image): (A) control sample, (B) sample with 4 kV cm−1 PEF strength, (C) sample with 7 kV cm−1 PEF strength, and (D) proportion of affected cells for the control (0 kV cm−1) and different PEF strength values. Statistical comparison of the condition with the lowest electric field strength to all the other higher strength values; data are presented in the form of means ± SD; t-test: *$p < 0.05$, **$p < 0.01$, and ***$p < 0.001$. Numbers of all, as well as only PI fluorescent cells, were manually counted. For each of the seven conditions, six microscopic samples were analyzed with over 560 cells on average for a single condition.

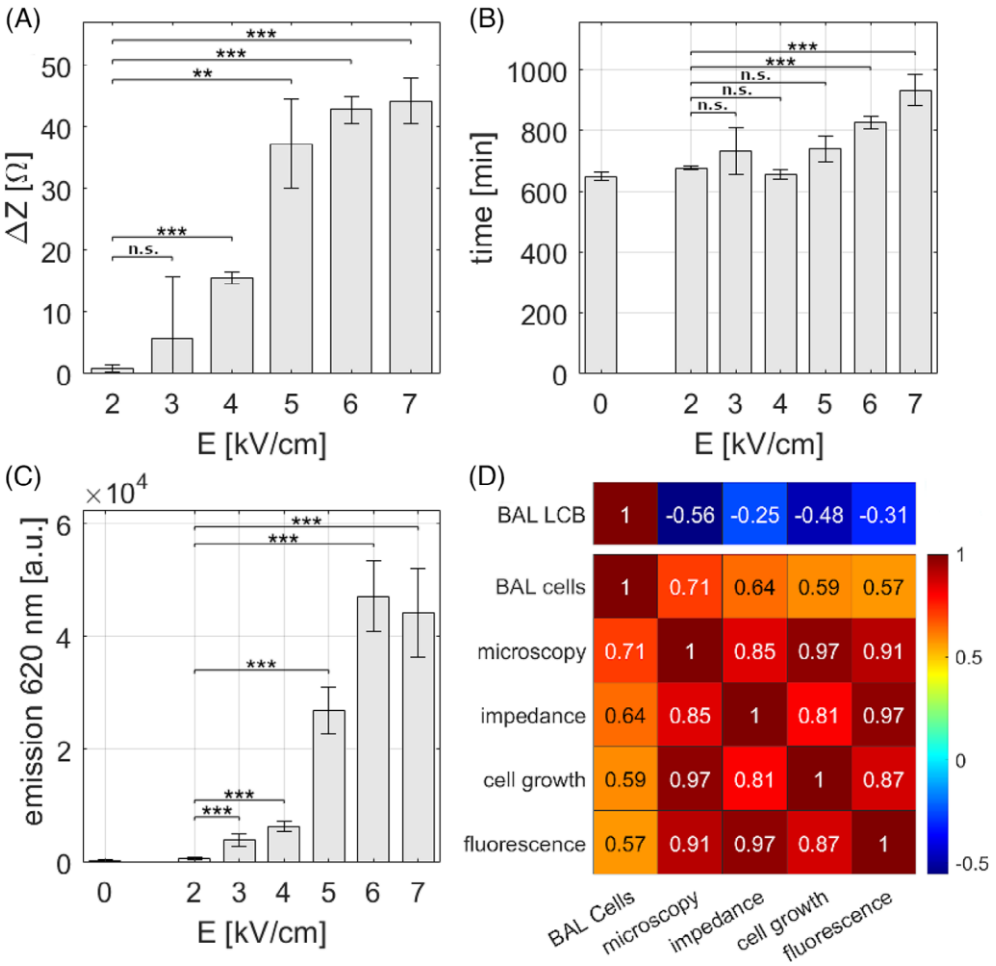

Fig. 45: Validation and correlation analysis: (A) Difference of the impedance before-after the application of all eight successive PEF pulses, (B) cell growth curves (time to reach 95% of the growth curvemaximum), and (C) cell permeabilization assayed by PI uptake measured by fluorescence emission. Statistical comparison of the condition with the lowest electric field strength to all the other PEF strength values. Data are presented in the form of means ± SD; t-test: **$p < 0.01$, ***$p < 0.001$. (D) Pearson's correlation heat map depicting relations between PEF strength dependencies from five different approaches applied to cells (microscopy denotes fluorescence microscopy approach from Figure 3). Correlation for two variants of BAL was applied: BAL cells and BAL LCB medium in order to assess the impact of cells.

Correlation Analysis of BAL Signal with Electroporation Markers

To further evaluate the relevance of the BAL signal, we performed a correlation analysis comparing the outcomes from all five methods applied in this study. For cells suspended in LCB buffer, Pearson's correlation coefficients between BAL and other indicators of electroporation ranged from 0.57 to 0.97 (Fig. 45D), indicating moderate to strong linear relationships. These findings suggest that BAL reliably reflects cell electroporation dynamics and can serve as a suitable real-time indicator of membrane permeabilization.

Our results show that electroporation events can be detected in real time, concurrently with pulse application, underscoring the method's potential for direct industrial use. Moreover, due to its simplicity, the system can be readily integrated into continuous-flow processing pipelines. We also developed quantitative performance metrics based on rigorous statistical evaluation, which can be implemented via a dedicated machine interface to provide real-time feedback on treatment effectiveness.

10 Conclusions and Main Contributions

The objective of the research presented in this thesis was the development of a measurement platform for experimentally investigating the effects of weak low-frequency magnetic fields on living biological systems utilizing both established and experimental techniques for cell concentration estimation. This work also seeks to establish a methodological framework for the systematic and accurate investigation of such effects, building upon experiments carried out on a newly developed experimental platform.

The initial phase of the work involves a comprehensive review of the state-of-the-art in LF MF bioeffects research. Existing studies were analyzed in terms of biological outcomes, magnetic field parameters, and experimental design strategies. A structured comparison was presented (see Tab. 1 and Tab. 2), highlighting the diversity of results, inconsistencies in control conditions, and the frequent lack of critical features such as temperature monitoring, temperature different between test and control samples, validating C/C and T/T pair experiments, and cross-over design. Despite the frequent reporting of significant biological effects, many of the reviewed studies lacked sufficient environmental control or statistical validity to distinguish LF MF specific responses from thermal or positional artifacts. These observations clearly demonstrated the need for a newly designed platform capable of conducting pair LF MF exposure experiments under well-regulated conditions with high reproducibility. The identified shortcomings directly informed the design criteria of the experimental system developed in this research.

A core achievement of this dissertation is the successful design, realization, and testing of a comprehensive experimental platform for pair LF MF exposure studies under controlled environmental conditions. The platform integrates multiple subsystems:

- Helmholtz coils are designed for uniform magnetic field generation with verified lateral homogeneity. The relative standard deviation from the nominal magnetic field density, measured across 15 spatial points within the working volume determined by the diameter of the beaker of 76.50 mm and height of 12 mm, remained well below 2.6%.

- The magnetic field generation system incorporates a waveform generator and high-power amplifier supporting dual and bridge configurations. In current configuration, the system allows generation of magnetic fields of up to 5 mT at frequencies ranging from 2 Hz to 2 kHz in the working volume.

- The platform includes accurate in-situ monitoring and regulation of sample's temperature. Initially unstable under an on-off controller (±1.5 °C), temperature stability was improved by using a PID controller and by optimized placement of external heaters. Final stability was ±0.3 °C, ensuring reproducible cultivation conditions.

The finalized experimental platform allows precise comparison between test and control samples using two parallel cultivation chambers, with the magnetic field and temperature in the working volumes kept at the same levels, within determined uncertainties. The modularity and internal consistency of the system support a wide variety of LF MF configurations and biological models, making the platform well-suited for extended biological investigations. Notably, the design addresses nearly all the methodological weaknesses identified in the earlier literature survey: it includes pair experimental capability, thermal monitoring for both test and control samples, support for C/C and T/T validation and can accommodate cross-over designs.

Multiple methods were evaluated to assess their suitability for ex-situ or in-situ real-time monitoring of cell growth using the developed experimental platform. Both optical turbidimetry and impedance spectroscopy approaches were focused, selected for their potential to capture dynamic changes in cell concentration. The evaluation included not only for their measurement performance, but also practical aspects such as ease of implementation, sensitivity to environmental factors, and compatibility with the developed experimental platform.

Impedance spectroscopy was explored extensively for its potential to provide real-time; in-situ estimates of cell concentration. Two estimation methods were tested: one based on the ratio of impedance at low and high frequencies, and the other based on permittivity dispersion using a characteristic frequency. For these experiments, a fully function real-time impedance spectroscopy system was successfully integrated into the measurement platform. The system uses a high-resolution frequency spectrum impedance analyzer operating between 10 Hz and 10 MHz in 4-wire configuration to reduce parasitic artifacts. Real-time impedance spectra were recorded during yeast cultivation to estimate cell concentration.

Despite the high-quality instrumentation and improved thermal stability, impedance-based biomass estimation was not consistently reliable in the current setup. The Soley-based estimation method frequently resulted in biologically implausible growth trends. The Asami model showed better alignment with reference data, particularly at 3.2 MHz. However,

sensor variability, environmental sensitivity, and electrode inconsistencies limit the broader applicability of the impedance-based cell concentration estimation. Despite these challenges, the impedance method was later applied successfully in our other study (Bereta et al., 2024 [43]), demonstrating applicability of impedance-based measurement of biological structure. This confirms that while not yet fully robust in this specific platform, the methodology itself is sound and worth further development.

Turbidimetry was selected as the reference method due to its simplicity, non-invasive nature, and strong correlation with hemocytometry-based cell counts. Using the developed experimental platform, the effects of 50 Hz and 3 mT magnetic field exposure on the growth of *Saccharomyces cerevisiae* were investigated in a fully controlled, pair experimental setup. Cell concentration was measured using optical turbidimetry. The results showed no statistically significant differences in growth curves between exposed and control groups. Across multiple independent replicates, the maximum deviation in optical density was negligible. However, due to the biological complexity and limitations of detection sensitivity, subtle or long-term effects cannot be fully excluded.

Thus, the thesis cautiously concludes that no robust biological effect of weak LF MF was detected under the tested conditions. However, the potential for subtle or frequency-specific interactions cannot be excluded. Further studies are recommended with improved sensor calibration, more replicates, and possibly more sensitive biological endpoints.

In summary, the dissertation offers substantial technical and methodological contributions to the field of MF bioeffects research. It delivers:

- A validated experimental platform for LF MF exposure
- An integrated real-time monitoring system
- Experimental protocols emphasizing thermal and magnetic symmetry
- A critical assessment of impedance-based biomass estimation

While no reliable evidence of biological effects was found, the infrastructure and protocols developed form a solid foundation for future investigations. In the long term, this work may provide exposure guidelines or enable novel MF-based biotechnological applications, including diagnostic and therapeutic technologies involving electromagnetic stimulation.

Author's Publications

Publications in scientific journals:

Vu Viet H., Kremnicky L., Bereta M., Teplan M. (2025). Experimental Platform for Investigation of Low-Frequency Magnetic Field Effects on Cells. *Measurement Science Review*, 25 (2), 83-92. http://doi.org/10.2478/msr-2025-0011

Berate M., Teplan M., Zakar, T., **Vu Viet H.**, Cifra M., Chafai D.E. (2024). Biological Autoluminescence Enables Effective Monitoring of Yeast Cell Electroporation. *Biotechnology Journal*, 19 (4), 2300475, https://doi.org/10.1002/biot.202300475

Publications in conference proceedings:

Teplan, M., **Vu Viet, H.**, Kremnicky, L., Bereta, M. (2025). Growth of Saccharomyces Cerevisiae in a 50 Hz Magnetic Field. *MEASUREMENT 2025*: *Proceeding of the 15th International Conference on Measurement*, 19-22, ISBN 978-80-69159-01-3, https://doi.org/10.23919/MEASUREMENT66999.2025.11078695

Vu Viet H., Teplan M., Kremnicky L., Bereta M. (2025). Optimization of Physical and Biological Parameters for Studying Microorganism Responses to Low-Frequency Magnetic Fields. *MEASUREMENT 2025*: *Proceeding of the 15th International Conference on Measurement*, 245-248, ISBN 978-80-69159-01-3, https://doi.org/10.23919/MEASUREMENT66999.2025.11078721

Vu Viet, H., Teplan, M. (2023). Development of An Experimental Platform for The Measurement of Biological Response of Low-Frequency Magnetic Fields. *MEASUREMENT 2023*: *Proceeding of the 14th International Conference on Measurement*, 113-116, ISBN 978-80-972629-7-6, https://doi.org/10.23919/MEASUREMENT59122.2023.10164326

Bereta, M., Teplan, M., Chafai D.E., Zakar T., **Vu Viet H.**, Cifra M. (2023). Assessment of Yeast Cells Electroporation by Autoluminescence and Impedance Measurements. *MEASUREMENT 2023*: *Proceeding of the 14th International Conference on Measurement*, 109-112, ISBN 978-80-972629-7-6, https://doi.org/10.23919/MEASUREMENT59122.2023.10164612

Vu Viet H., Teplan M. (2021). Impact of Magnetic Field on Yeast Cells Monitored by Impedance Spectroscopy. *IWIS 2021: Proceeding of International Workshop on Impedance Spectroscopy*, 85-88, ISBN 978-1-6654-9472-4, https://doi.org/10.1109/IWIS54661.2021.9711789

Teplan M., **Vu Viet H.**, Bereta M., Bajla I. (2021). Measurement System for Monitoring of Magnetic Field Effects on Yeast Cells by Impedance Spectroscopy. *MEASUREMENT 2021: Proceeding of the 13th International Conference on Measurement*, 198-201, ISBN 978-80-972629-5-2, http://doi.org/10.23919/Measurement52780.2021.9446776

Abstracts in scientific conferences:

Berate M., Teplan M., Zakar, T., **Vu Viet H.**, Cifra M., Chafai D.E. (2025). Biological Autoluminescence as a Real-Time Monitoring Tool for Yeast Electroporation, BioEM 2025, Rennes, France

Vu Viet H., Teplan M. (2023). Development of An Experimental Platform for the Measurement of Low-Frequency Magnetic Field Effect on Yeast Cells. *ZBORNÍK ABSTRAKTOV: XLIV. DNÍ LEKÁRSKEJ BIOFYZIKY*, 44th Conference Day of Medical Biophysics, Stara Lesna, Slovakia, 84-85 https://www.44dlb.sk/pre_autorov/zbornik-abstraktov/

Teplan M., **Vu Viet H**. (2021), Impedance Spectroscopy Monitoring of Magnetic Field Effects on Yeast Cells. *Abstract Book International Workshop on Impedance Spectroscopy*, 14th International Workshop on Impedance Spectroscopy, Chemnitz, Germany, 151-154, ISBN 978-3-949744-00-6

Participation in congresses and conferences:

14th International Conference on Measurement, May 29th – May 31st, 2023, Institute of Measurement Science SAS, Smolenice Castle, Smolenice, Slovakia

44th Conference Day of Medical Biophysics, May 31st – June 2nd, 2023, Faculty of Medicine Comenius University Bratislava, Congress center of SAS academia, Stara Lesna, Slovakia

14th International Workshop on Impedance Spectroscopy, September 29th – October 1st, 2021, Technische Universität Chemnitz, Chemnitz, Germany

13th International Conference on Measurement, May 17th – May 19th, 2021, Institute of Measurement Science SAS, Bratislava, Slovakia

References

[1] Tota, M., Jonderko, L., Witek, J., Novickij, V., Kulbacka, J. (2024). Cellular and molecular effects of magnetic fields. *International Journal of Molecular Sciences*, 25 (16), 8973. https://doi.org/10.3390/ijms25168973

[2] Lee, H. C., Hong, M.-N., Jung, S. H., Kim, B. C., Suh, Y. J., Ko, Y.-G., Lee, Y.-S., Lee, B.-Y., Cho, Y.-G., Myung, S.-H., Lee, J.-S. (2015). Effect of extremely low frequency magnetic fields on cell proliferation and gene expression. *Bioelectromagnetics*, 36 (7), 506-516. https://doi.org/10.1002/bem.21932

[3] Zhang, M., Li, X., Bai, L., Uchida, K., Bai, W., Wu, B., Xu, W., Zhu, H., Huang, H. (2013). Effects of low frequency electromagnetic field on proliferation of human epidermal stem cells: An in vitro study. *Bioelectromagnetics*, 34 (1), 74-80. https://doi.org/10.1002/bem.21747

[4] Pasi, F., Sanna, S., Paolini, A., Alquati, M., Lascialfari, A., Corti, M. E., Di Liberto, R., Cialdai, F., Monici, M., Nano, R. (2016). Effects of extremely low-frequency magnetotherapy on proliferation of human dermal fibroblasts. *Electromagnetic Biology and Medicine*, 35 (4), 343-352. https://doi.org/10.3109/15368378.2016.1138123

[5] Radil, R., Carnecka, L., Judakova, Z., Pobocikova, I., Bajtos, M., Janousek, L. (2024). Exploring non-thermal mechanisms of biological reactions to extremely low-frequency magnetic field exposure. *Applied Sciences*, 14 (20), 9409. https://doi.org/10.3390/app14209409

[6] Tang R., Xu Y., Ma F., Ren J., Shen S., Du Y., Hou Y., Wang T., (2016). Extremely low frequency magnetic fields regulate differentiation of regulatory T cells: Potential role for ROS-mediated inhibition on AKT, *BioElectroMagnetics*, 37 (2), 89-98. https://doi.org/10.1002/bem.21954

[7] Lai, H. (2021). Genetic effects of non-ionizing electromagnetic fields. *Electromagnetic Biology and Medicine*, 40 (2), 264-273. https://doi.org/10.1080/15368378.2021.1881866

[8] Duong, C. N., Kim, J. Y. (2016). Exposure to electromagnetic field attenuates oxygen-glucose deprivation-induced microglial cell death by reducing intracellular Ca2+ and ROS. *International Journal of Radiation Biology*, 92 (4), 195-201. https://doi.org/10.3109/09553002.2016.1136851

[9] Wertheimer N., Leeper, E. (1979). Electrical Wiring Configurations and Childhood Cancer, *American Journal of Epidemiology*, 109 (3), 273-284. https://doi.org/10.1093/oxfordjournals.aje.a112681

[10] Turner M. C., Benke G., Bowman J. D., Figuerola J., Fleming S., Hours M., Kincl L., Krewski D., McLean D., Parent M. E., Richardson L., Sadetzki S., Schlaefer K., Schlehofer B., Schüz J., Siemiatycki J., van Tongeren M., Cardis E. (2014). Occupational Exposure to Extremely Low-Frequency Magnetic Fields and Brain Tumor Risks in the INTEROCC Study, *Cancer Epidemiology Biomarkers and Prevention*, 23 (9), 1863-1872. https://doi.org/10.1158/1055-9965.epi-14-0102

[11] Savitz D. A., Liao D., Sastre A., Kleckner R.C., Kavet R. (1999) Magnetic Field Exposure and Cardiovascular Disease Mortality among Electric Utility Workers, *American Journal of Epidemiology*, 149 (2), 135-142. https://doi.org/10.1093/oxfordjournals.aje.a009779

[12] Caliogna, L., Medetti, M., Bina, V., Brancato, A. M., Castelli, A., Jannelli, E., Ivone, A., Gastaldi, G., Annunziata, S., Mosconi, M., Pasta, G. (2021). Pulsed electromagnetic fields in bone healing: Molecular pathways and clinical applications. *International Journal of Molecular Sciences*, 22 (14), 7403. https://doi.org/10.3390/ijms22147403

[13] Gualdi, G., Costantini, E., Reale, M., Amerio, P. (2021). Wound repair and extremely low frequency-electromagnetic field: Insight from in vitro study and potential clinical application. *International Journal of Molecular Sciences*, 22 (9), 5037. https://doi.org/10.3390/ijms22095037

[14] Xu, A., Wang, Q., Lin, T. (2020). Low-frequency magnetic fields (LF-MFs) inhibit proliferation by triggering apoptosis and altering cell cycle distribution in breast cancer cells. *International Journal of Molecular Sciences*, 21 (8), 2952. https://doi.org/10.3390/ijms21082952

[15] Wang, S., Zhou, X., Huang, B., Wang, Z., Zhou, L., Wang, M., Yu, L., Jiang, H. (2016). Noninvasive low-frequency electromagnetic stimulation of the left stellate ganglion reduces myocardial infarction-induced ventricular arrhythmia. *Scientific Reports*, 6 (1), 30783. https://doi.org/10.1038/srep30783

[16] Rick, O., von Hehn, U., Mikus, E., Dertinger, H., Geiger, G. (2017). Magnetic field therapy in patients with cytostatics-induced polyneuropathy: A prospective randomized placebo-controlled phase-III study. *Bioelectromagnetics*, 38 (2), 85-94. https://doi.org/10.1002/bem.22005

[17] Sun, J., Tong, Y., Jia, Y., Jia, X., Wang, H., Chen, Y., Wu, J. Jin, W., Ma, Z., Cao, K., Li, X., Chen, Z., Yang, G. (2023). Effects of extremely low frequency electromagnetic fields on the tumor cell inhibition and the possible mechanism. *Scientific Reports*, 13 (1), 6989. https://doi.org/10.1038/s41598-023-34144-5

[18] Barbault A., Costa F.P., Bottger B., Munden R.F., Bomholt F., Kuster N., Pasche B. (2009). Amplitude-modulated electromagnetic fields for the treatment of cancer: Discovery of tumor-specific frequencies and assessment of a novel therapeutic approach. *Journal of Experimental and Clinical Cancer Research*, 28, 51. https://doi.org/10.1186/1756-9966-28-51

[19] Brabant, C., Geerinck, A., Beaudart, C., Tirelli, E., Geuzaine, C., Bruyere, O. (2023). Exposure to magnetic fields and childhood leukemia: A systematic review and meta-analysis of case-control and cohort studies. *Reviews on Environmental Health*, 38 (2), 229-253. https://doi.org/10.1515/reveh-2021-0112

[20] Baaken, D., Dechent, D., Blettner, M., Drießen, S., Merzenich, H. (2021). Occupational exposure to extremely low-frequency magnetic fields and risk of amyotrophic lateral sclerosis: Results of a feasibility study for a pooled analysis of original data. *Bioelectromagnetics*, 42 (4), 271-283. https://doi.org/10.1002/bem.22335

[21] Dasdag, O., Adalier, N., Dasdag, S. (2020). Electromagnetic radiation and Alzheimer's disease. *Biotechnology & Biotechnological Equipment*, 34 (1), 1087-1094. https://doi.org/10.1080/13102818.2020.1820378

[22] Tian, H., Zhu, H., Gao, C., Shi, M., Yang, D., Jin, M., Wang, F., Sui, X. (2023). System-level biological effects of extremely low-frequency electromagnetic fields: An in vivo experimental review. *Frontiers in Neuroscience*, 17, 1247021. https://doi.org/10.3389/fnins.2023.1247021

[23] Sincak, M., Luptakova, A., Matusikova, I., Jandacka, P., Sedlakova-Kadukova, J. (2023). Application of a magnetic field to enhance the environmental sustainability and efficiency of microbial and plant biotechnological processes. *Sustainability*, 15 (19), 14459. https://doi.org/10.3390/su151914459

[24] Liu, J., Wang, D., Wang, H., Yang, N., Hou, J., Lv, X., Gong, L. (2024). Low frequency magnetic field assisted production of acidic protease by Aspergillus niger. *Archives of Microbiology*, 206, 273. https://doi.org/10.1007/s00203-024-04004-5

[25] Novák J., Strašák, L., Fojt, L., Slaninová, I., Vetterl, V. (2007). Effects of low-frequency magnetic fields on the viability of yeast Saccharomyces cerevisiae. *Bioelectrochemistry*, 70 (1), 115-121. https://doi.org/10.1016/j.bioelechem.2006.03.029

[26] Adey W.R. (1980). Frequency and power windowing in tissue interactions with weak electromagnetic fields. *Proceedings of IEEE*, 68 (1), 119–125. https://doi.org/10.1109/PROC.1980.11591

[27] Liboff, A. R., (1985). Geomagnetic cyclotron resonance in living cells. *Journal of Biological Physics*, 13, 99-102. https://doi.org/10.1007/BF01878387

[28] Lednev V. V. (1991). Possible mechanism for the influence of weak magnetic fields on biological systems. *BioElectroMagnetics*, 12 (2), 71-75. https://doi.org/10.1002/bem.2250120202

[29] Belova N. A., Panchyeluga, V. A. (2010). Lednev's model: Theory and experiment. *Biophysics*, 55 (4), 661-674. https://doi.org/10.1134/S0006350910040263

[30] Steiner U. E. and Ulrich T. (1989). Magnetic field effects in chemical kinetics and related phenomena, *Chemical Reviews*, 89 (1), 51-147. https://doi.org/10.1021/cr00091a003

[31] Woodward J. R. (2002). Radical Pairs in Solution, *Progress in Reaction Kinetics and Mechanism*, 27 (3), 165-207. https://doi.org/10.3184/007967402103165388

[32] Barnes F. S. and Greenebaum, B. (2015). The effects of weak magnetic fields on radical pairs, *BioElectroMagnetics*, 36 (1), 45-54. https://doi.org/10.1002/bem.21883

[33] Rochev Y. A., Narimanov A. A., Sosunov E. A., Kozlov A. N., Lednev V. V. (1990). Effects of Weak Magnetic-field on the Rate of Cell-Proliferation in Culture. *Studia Biophysica*, 135 (1-2), 93-98.

[34] Yost M. G., Liburdy, R. P. (1992). Time-varying and static magnetic fields act in combination to alter calcium signal transduction in the lymphocyte, *FEBS Letters*, 296 (2), 117-122. https://doi.org/10.1016/0014-5793(92)80361-j

[35] Bodewein, L., Schmiedchen, K., Dechent, D., Stunder, D., Graefrath, D., Winter, L., Kraus, T., Driessen, S. (2019). Systematic review on the biological effects of electric, magnetic and electromagnetic fields in the intermediate frequency range (300 Hz to 1 MHz). *Environmental Research*, 171, 247-259. https://doi.org/10.1016/j.envres.2019.01.015

[36] Buchachenko, A. (2016). Why magnetic and electromagnetic effects in biology are irreproducible and contradictory? *Bioelectromagnetics*, 37 (1), 1-13. https://doi.org/10.1002/bem.21947

[37] International Commission on Non-Ionizing Radiation Protection (ICNIRP). (2025). Gaps in knowledge relevant to the "ICNIRP guidelines for limiting exposure to time-varying electric, magnetic and electromagnetic fields (100 kHz TO 300 GHz)". *Health Physics*, 182 (2), 190-202. https://doi.org/10.1097/HP.0000000000001944

[38] Makinistian, L., Vives, L. (2025). Devices, facilities, and shielding for biological experiments with static and extremely low frequency magnetic fields. *IEEE Journal of Electromagnetics, RF and Microwaves in Medicine and Biology*, 9 (2), 141-156. https://doi.org/10.1109/JERM.2024.3419232

[39] Ronniger, M., Aguida, B., Stacke, C., Chen, Y., Ehnert, S., Erdmann, N., Eschenburg, G., Falldorf, K., Pooam, M., Wing, A., Ahmad, M. (2022). A novel method to achieve precision and reproducibility in exposure parameters for low-frequency pulsed magnetic fields in human cell cultures. *Bioengineering*, 9 (10), 595. https://doi.org/10.3390/bioengineering9100595

[40] Bereta, M., Teplan, M., Chafai, D. E., Radil, R., Cifra, M. (2021). Biological autoluminescence as a noninvasive monitoring tool for chemical and physical modulation of oxidation in yeast cell culture. *Scientific Reports*, 11, 328. https://doi.org/10.1038/s41598-020-79668-2

[41] Vu Viet, H., Teplan, M. (2023). Development of an experimental platform for the measurement of biological response of low-frequency magnetic fields. MEASUREMENT *2023: 14th International Conference on Measurement*. IEEE, 113-116. https://doi.org/10.23919/MEASUREMENT59122.2023.10164326

[42] Bajla, I., Teplan, M. (2022). Yeast cell detection in color microscopic images using ROC-optimized decoloring and segmentation. *IET Image Processing*, 16 (2), 606-621. https://doi.org/10.1049/ipr2.12376

[43] Bereta, M., Teplan, M., Zakar, T., Vuviet, H., Cifra, M., Chafai, D. E. (2024). Biological autoluminescence enables effective monitoring of yeast cell electroporation. *Biotechnology Journal*, 19 (4), 2300475. https://doi.org/10.1002/biot.202300475

[44] An G.-Z., Xu, H., Zhou, Y., Du, L., Miao, X., Jiang, D.-P., Li, K.-C., Guo, G.-Z., Zhang, C., Ding, G.-R. (2015). Effects of long-term 50Hz power-line frequency electromagnetic field on cell behavior in Balb/c 3T3 cells. *PLoS One*, 10 (2), e0117672. https://doi.org/10.1371/journal.pone.0117672

[45] Song K., Im, S. H., Yoon, Y. J., Kim, H. M., Lee, H. J., Park, G. S. (2018). A 60 Hz uniform electromagnetic field promotes human cell proliferation by decreasing intracellular reactive oxygen species levels. *PLoS One*, 13 (7), e0199753. https://doi.org/10.1371/journal.pone.0199753

[46] Cifra M, Fields J.Z., Farhadi A. (2011).Electromagnetic cellular interactions. *Progress in Biophysics Molecular Biology*, 105(3), 223-246. https://doi.org/10.1016/j.pbiomolbio.2010.07.003

[47] Jones, R. A., Walleczek, J., Adey, W. R. (1996). Mechanical vibration in "double-wound" magnetic field exposure coils. *Bioelectromagnetics*, 17 (6), 516-518. https://doi.org/10.1002/(SICI)1521-186X(1996)17:6%3C516::AID-BEM14%3E3.0.CO;2-I

[48] Radil R., Barabas J., Janousek L., Bereta, M. (2020). Frequency-dependent alterations of S. Cerevisiae proliferation due to LF EMF exposure. *Advances in Electrical and Electronic Engineering*, 18(2), 99-103. https://doi.org/10.15598/aeee.v18i2.3461

[49] Wang J.D., Levin P.A. (2009). Metabolism, cell growth and the bacterial cell cycle. *Nature Reviews Microbiology*, 7 (11), 822–827. https://doi.org/10.1038/nrmicro2202

[50] Cooper G. M. (2000). The Eukaryotic Cell Cycle. *The Cell: A Molecular Approach. 2nd edition*, Sunderland (MA): Sinauer Associates. ISBN-10: 0-87893-106-6. https://www.ncbi.nlm.nih.gov/books/NBK9876/

[51] *ECACC Laboratory Handbook 4th Edition (2018)*. Fundamental Techniques in Cell Culture, Cell Types & Culture Characteristics, 12-14. https://www.sigmaaldrich.com/deepweb/assets/sigmaaldrich/marketing/global/documents/177/566/ecacc-handbook-br2808en-mk.pdf?srsltid=AfmBOopYYNBGXCfvr9Oy-W8o6HEjsMnY_EHT-f3m8FqrJALEzRVo4MhW

[52] Alberghina L., Coccetti P., Orlandi I. (2009). Systems biology of the cell cycle of Saccharomyces cerevisiae: From network mining to system-level properties, *Biotechnology Advances*, 27 (6), 960-978. https://doi.org/10.1016/j.biotechadv.2009.05.021

[53] Breitenbach, M., Ralser M., Perrone G. G., Iglseder B., Rinnerthaler M., Dawes I. W. (2013). Oxidative stress and neurodegeneration: the yeast model system, *Frontiers in Bioscience* 18, 1174-1193. https://doi.org/10.2741/4171

[54] Pereira C., Coutinho I., Soares J., Bessa C., Leão M., Saraiva L. (2012). New insights into cancer-related proteins provided by the yeast model, *The FEBS journal* 279, 697-712. https://doi.org/10.1111/j.1742-4658.2012.08477.x

[55] Available online: https://upload.wikimedia.org/wikipedia/commons/8/80/Laboratoorne_pagarip%C3%A4rm_%28Saccharomyces_cerevisiae%29_agariplaadil..JPG

[56] Available online: https://upload.wikimedia.org/wikipedia/commons/thumb/9/95/Saccharomyces_cerevisiae_SEM.jpg/1920px-Saccharomyces_cerevisiae_SEM.jpg

[57] Radil R. (2012). Analýza netepelných účinkov nízkofrekvenčného elektromagnetického poľa na vybrané biologické štruktúry, *Ph.D. Dissertation*. University of Zilina, Slovakia, 4-9.

[58] Liu M., Chu W., Guo T., Zeng X., Shangguan Y., He F., Liang X. (2024) Challenges of Cell Counting in Cell Therapy Products. *Cell Transplantation*, 33. https://doi.org/10.1177/09636897241293628

[59] Bick J., (2021) Cell Counting Best Practices. Available online: http://www.fount-med.com/view-id-337.html

[60] Freund M., and Carol B., (1964) Factors affecting hemocytometer counts of sperm concentration in human semen, *Reproduction*, 149-155. https://doi.org/10.1530/jrf.0.0080149

[61] Chauncey W. Anderson (2005). Turbidity: U.S. Geological Survey Techniques of Water-Resources Investigations, book 9, chap. A6.7. https://doi.org/10.3133/twri09A6.7

[62] Cell Signaling Technology, Overview of Flow Cytometry. Available online: https://www.cellsignal.co.uk/applications/flow-cytometry/flow-cytometry-overview

[63] Whitman T. A., Forrest J.C., Morgan M. T., Okos M. R. (1996). Electrical Measurement for Detecting Early Postmortem Changes in Porcine Muscle, *Journal of Animal Science*, 74 (1), 80-90. https://doi.org/10.2527/1996.74180x

[64] Asami K., Yonezawa T. (1995). Dielectric analysis of yeast cell growth, *Biochimica et Biophysica Acta*, 1245, 99-105. https://doi.org/10.1016/0304-4165(95)00074-L

[65] Foster K. R., Schwan H. P. (1989). Dielectric Properties of Tissues and Biological Materials: A Critical Review, *Critical Reviews in Biomedical Engineering*, 17 (1), 25-104. PMID: 2651001

[66] Soley A., Lecina M., Gámez X., Cairó J.J., Riu P., Rosell X., Bragós R., Gòdia F. (2005). On-line monitoring of yeast cell growth by impedance spectroscopy. *J Biotechnol*, 118(4), 398-405. https://doi.org/10.1016/j.jbiotec.2005.05.022

[67] Cole, K.S. and Cole, R.H. (1941). Dispersion and Absorption in Dielectrics I. Alternating Current Characteristics. *The Journal of Chemical Physics*, 9, 341-351. https://doi.org/10.1063/1.1750906

[68] Bragos, R., (1997) Contribution to the characterization of biological systems using electrical impedance spectroscopy. Ph.D. Dissertation. Polithecnic University of Catalonia, Barcelona

[69] García-Farieta J., Hurtado Al., (2020). Exploring the magnetic field of Helmholtz and Maxwell coils: a computer-based approach exploiting the superposition principle. *Revista Brasileira de Ensino de Física*, 42. http://dx.doi.org/10.1590/1806-9126-RBEF-2020-0282

[70] Wikipedia: Helmholtz coil, Available online: https://en.wikipedia.org/wiki/Helmholtz_coil

[71] H. A. Wheeler (1928). Simple Inductance Formulas for Radio Coils. *Proceedings of the Institute of Radio Engineers*, 16 (10), 1398-1400. https://doi.org/10.1109/JRPROC.1928.221309

Appendix A - Experimental procedure

The whole experimental setup together with procedures was issued to keep a fixed workflow. This is to ensure every single step of the process will be executed because one missing step would cause a vital effect on the final result. Following are instructions for the pre-cultivation process and the main experiment.

Pre-cultivation

1. Clean laboratory glassware, stirring rod, pipetting tips, and any other tools that could come into direct contact with biological material with spring and ethanol. Next, submerge them in hot water at 80° ~ 100°C for 5 minutes. Afterward, place them in the polymerase chain reaction (PCR) cabinet.

2. Prepare a water tank, setup heater, and magnetic stirrer to be ready for the pre-cultivation.

3. Turn on the UV lamps of the PCR cabinet and the laboratory for 30 minutes.

4. Inoculation of yeast from a petri dish into a beaker with fresh YPD medium.

    a. When inoculating, do not forget to cool the eye in agar.

    b. Keep the petri dish open for a minimum amount of time.

    c. Always cover the dish with new parafilm after work.

    d. Petri dish must be stored upside down in the refrigerator (yeast and agar turned up so that the condensed drops remain at the bottom).

    e. It is necessary to monitor the condition of the yeast on the Petri dishes and after several weeks to months provide new yeast or inoculate the old yeast on new agar.

5. Put magnetic bean into the beaker with yeast cells and YPD. Cover the top of both beakers with one layer of parafilm and one layer of aluminum foil.

6. Put both beakers in the prepared water tank and start the magnetic stirrer.
   The minimum pre-cultivation time is at least 12 hours.

Main Experiment

1. Before starting, warm up two cultivation chambers to 35°C.
2. Disinfect laboratory tools that could come into direct contact with biological material with spring and ethanol then submerge them in hot water at 80° ~ 100°C for 5 minutes and place them in the polymerase chain reaction (PCR) cabinet.
3. Turn on the UV lamps of the PCR cabinet and of the laboratory for 30 minutes
4. Inside the PCR cabinet, prepare 2 beakers with 100ml of fresh YPD medium.
5. Pipette 1 ml of the precultured yeast solution into each prepared beaker.
6. Insert stirring rods and impedance probes into the beakers and cover them with their lids. Place the beakers into the cultivation chambers, and start mixing, set 200 rpm on digital stirrers.
7. Start operation and measurement of platform devices: temperature monitoring, impedance, and magnetic systems.

Laboratory maintenance

1. The PCR cabinet needs to be cleaned and disinfected once a month. Spray all the walls and the stand under the UV lamp in with ethanol, then wipe with a disposable paper towel. Afterward, turn on its UV lamp for 20 minutes.
2. Turn on the UV lamp in the whole laboratory once every two weeks.

Maintaining Sterility

As our laboratory is not a certified lab for work with microbiological materials at the level of sterility assurance level (SAL) of 10^{-4} or lower thus keeping sterility was quite an issue in our situation. During the main experiment of 15-hour duration, bacteria might easily evade and massively reproduce inside YPD solutions. **Error! Reference source not found.**

left) shows the affected solution mixing between cultivated cells and bacteria and (right) a clean solution after over 15 hours of cultivation.

This problem of sterility caused a significant effect on our measurement, especially during the 15-hour-long experiment. Bacteria will consume the supplement in the YPD medium, which is intended for yeast cells, causing changes in the condition of the environment inside the cultivation chambers. Mass reproduction of bacteria will occur not only in the reduction of yeast cells' concentration but also in changes in yeast's growth phase duration. Thus, the final measurement outcomes would be distorted.

Thus, the strict process of the experimental procedure for maintaining and keeping sterility was issued to cover the solution to this problem

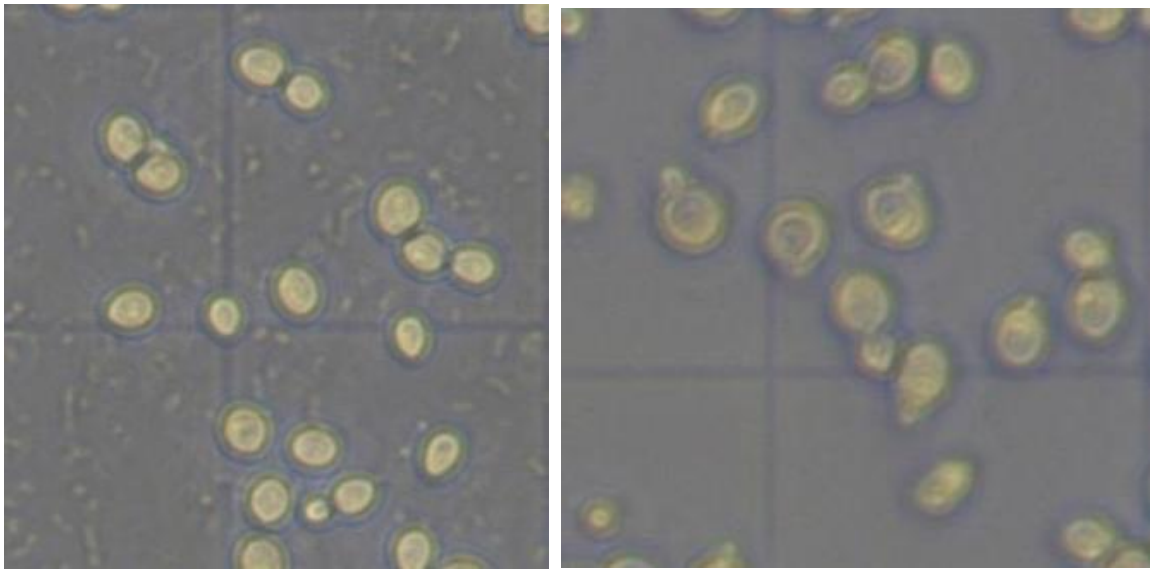

(a) (b)

Fig. A1: Comparison of two cultivation results after 15 hours of cultivating experiment, with bacteria (a), and without bacteria (b).

Appendix B - Impedance Spectroscopy Analyzer

Impedance analyzer ISX-3v2 from Sciospec (Fig. A2) was selected to perform impedance spectroscopy measurements. The instrument offers a 4-wire measurement with a measuring frequency range of up to 10 MHz (Fig. A3). As displayed in Fig. A4, the system topology of the impedance analyzer in the 4-wire configuration includes one current injecting COUNTER electrode port (C-port), one high impedance REFERENCE (R) port, one high impedance WORKING SENSE (WS) port and one WORK (W) port. Voltage measurement is performed by measuring the R-port potential against the potential of the WS port giving in result the potential drop/difference from REFERENCE to WORKING SENSE. This configuration gives the most accurate results because the error introduced by the wires is reduced to a minimum due to the high impedance characteristic of the voltage measurement path.

The instrument's 4-wire configuration is compatibly utilized with the 4-cell Orion conductivity probe from ThermoFisher Scientific. The geometry of the probe's electrodes is circular with outer rings for the injection of probing current and an inner circle for voltage sensing (Fig. A5).

The continual impedance measurement mode allows looping one measuring setup over any required time. One measuring setup performs one impedance measurement of the whole spectrum from 10 Hz to 10 MHz divided into 350 logarithmically distributed frequency points and usually takes around 60 s duration depending on its precision and delay setup.

The kinetic measurement mode of the instrument allows tracking impedance at up to 16 different frequency points of choice at the same time. This future feature will be for us to develop our real-time impedance monitoring setup.

Fig. A2: Impedance analyzer ISX-3v2 from Sciospec

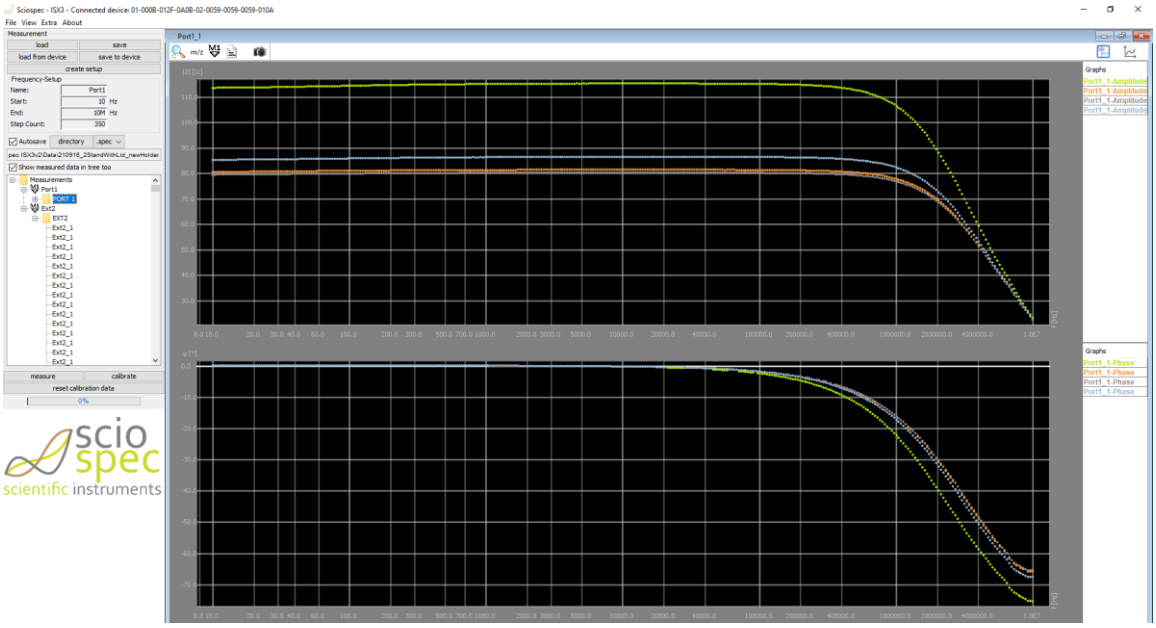

Fig. A3: Example GUI of ScioSpec controlling software.

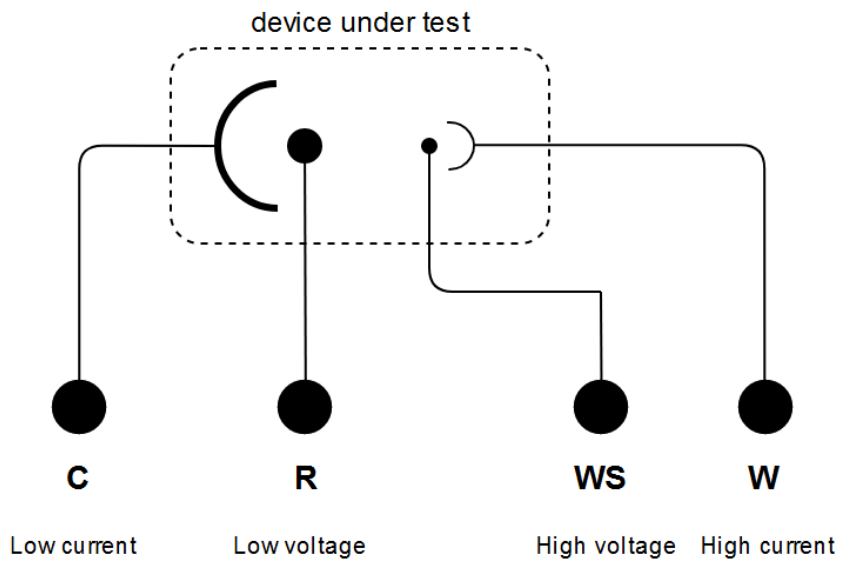

Fig. A4: 4-wire configuration measurement setup of the Impedance analyzer ISX-3v2

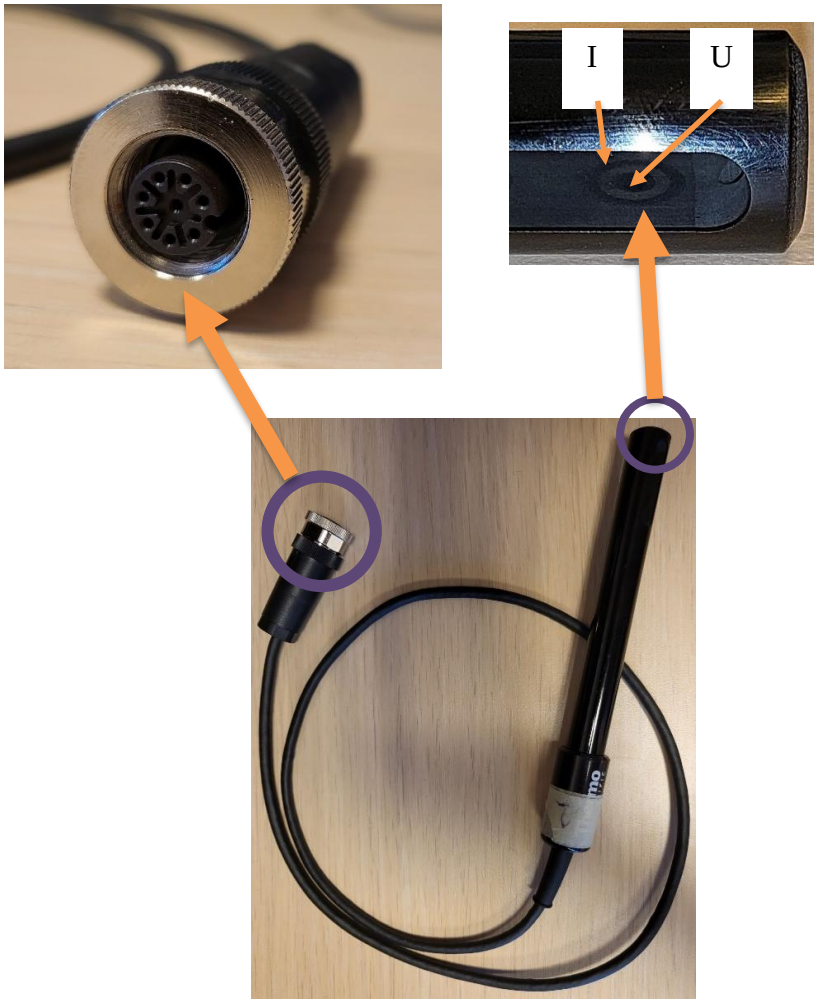

Fig. A5: Orion probe from ThermoFisher Scientific with outer rings for injection of probing current and inner circles for sensing voltage.

Appendix C - Helmholtz Coil's Parameters

Direct current resistance of the designed Helmholtz coil:

$$R = \rho \frac{l}{A}$$

Where:

ρ is the resistivity of copper, $\rho = 1.67 * 10^{-8}\ \Omega.m$

l is the total wire length, $l_{per\ turn} = 2\pi r \approx 0.3456\ m\ (r = 0.055\ m)$

total wire length $l = 50 * l_{per\ turn} \approx 17.28\ m$

A is the wire's cross-sectional area $A = \pi * (\Phi/2) \approx 3.80 * 10^{-6}\ m^2\ (\Phi = 0.0022\ m)$

Total resistance for both coils in series:

$R_{total} = 2 * R \approx 2 * 0.076\ \Omega \approx 0.152\ \Omega$

Uncertainty calculation detail

According to the Keithley 2000 datasheet (https://download.tek.com/datasheet/2000-DMM-Data-Sheet-1KW612970.pdf), the typical accuracy for the 1 Ω range is specified as, which was used to estimate the uncertainty of the measurement:

Accuracy = ±(0.010% of Reading + 0.004% of Range)

Fig. A6: Measuring the direct current resistance of the designed Helmholtz coil using Keithley 2000 multimeter.

Inductance calculation via Wheeler's formulas:

$$L = 31.6 * 10^{-6} * \frac{N^2 r^2}{6r + 9w + 10(r_2 - r)}$$

Where:

N is the total number of turns, *N = 50* (10 turns per layer, 5 layers)

r is the inner radius of the coil, *r = 0.055 m*

w is the thickness of the coil, *w = 5*Φ = 0.011 m (Φ = 0.0022 m) -0,009944*

r_2 is the outer radius $r_2 = r+5*\Phi = 0.066$ *m*

L ≈ 0.443 mH

The total inductance of the Helmholtz coil consisting of 2 coils in series is:

$L_{total} \approx 2*0.443$ *mH = 0.886 mH*

According to the Agilent 4284A Precision LCR Meter datasheet (https://www.unifr.ch/med/de/assets/public/professoren/rainerg/Documents/Manuals/AGILENT_4284A.pdf), the typical accuracy for the 2 mH range setting is specified as, which was used to estimate the uncertainty of the measurement:

Accuracy = ±(0.1% of Reading + 0.06% of Range)

Fig. A7: Measuring inductance of the Helmholtz coil using Agilent 4284A Precision LCR Mete

Appendix E – Supplement Figures

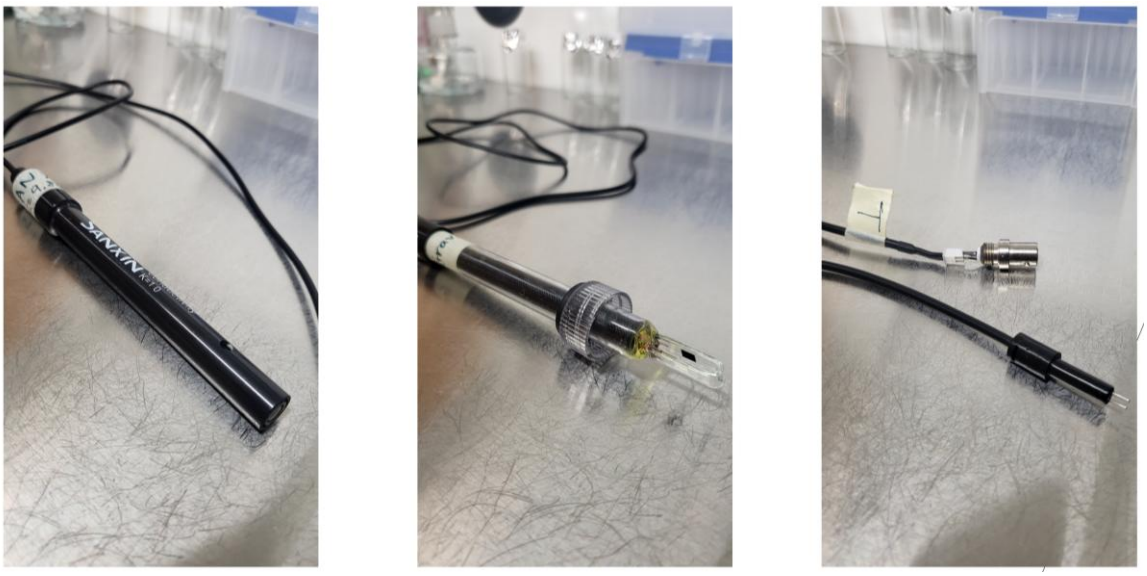

(a) (b) (c)

Fig. A8: Photographs of three representative electrode types used in impedance measurements: Sanxi (a), Gravity (b), and custom T-shaped electrode (c). These probes, along with Orion and Metrohm (not shown), were employed to assess probe-specific variability during discrete cell addition experiments

(a) (b)

Fig. A9: (a) Custom-designed 3D-printed base used to secure vials inside a beaker during the experiment. (b) Experimental setup with sealed vials containing yeast cultures placed in the base for magnetic field exposure and control conditions. A total of 10 vials were used (5 test, 5 control), along with 2 additional 10× dilution controls.

		Volume (ml)				Burker Concentration		
	Riedenie	Sample	Water	Turbidity	%	1/6.25nl	10^7/ml	%
100%	1.000	20.000	0.000	662	100.00	245.80	3.93	100.00
90%	1.111	18.000	2.000	600	90.64	219.20	3.51	89.18
80%	1.250	17.778	2.222	527	79.56	197.60	3.16	80.39
70%	1.429	17.500	2.500	448	67.66	173.00	2.77	70.38
60%	1.667	17.143	2.857	370	55.92	147.60	2.36	60.05
50%	2.000	16.667	3.333	291	43.93	123.80	1.98	50.37
40%	2.500	16.000	4.000	214	32.31	118.60	1.90	48.25
30%	3.333	15.000	5.000	123	18.63	89.20	1.43	36.29
20%	5.000	13.333	6.667	75	11.38	43.20	0.69	17.58
10%	10.000	10.000	10.000	31	4.65	19.00	0.30	7.73

Fig. A10: Data set of serial dilution used for turbidity and cell concentration calibration. Each dilution step shows the corresponding sample and water volumes, measured turbidity (NTU), and yeast cell concentration determined via Bürker chamber counting (expressed in cells per 6.25 nl, 10^7/ml, and as a percentage of the undiluted sample). These values form the basis for establishing the calibration curve between turbidity and cell concentration.

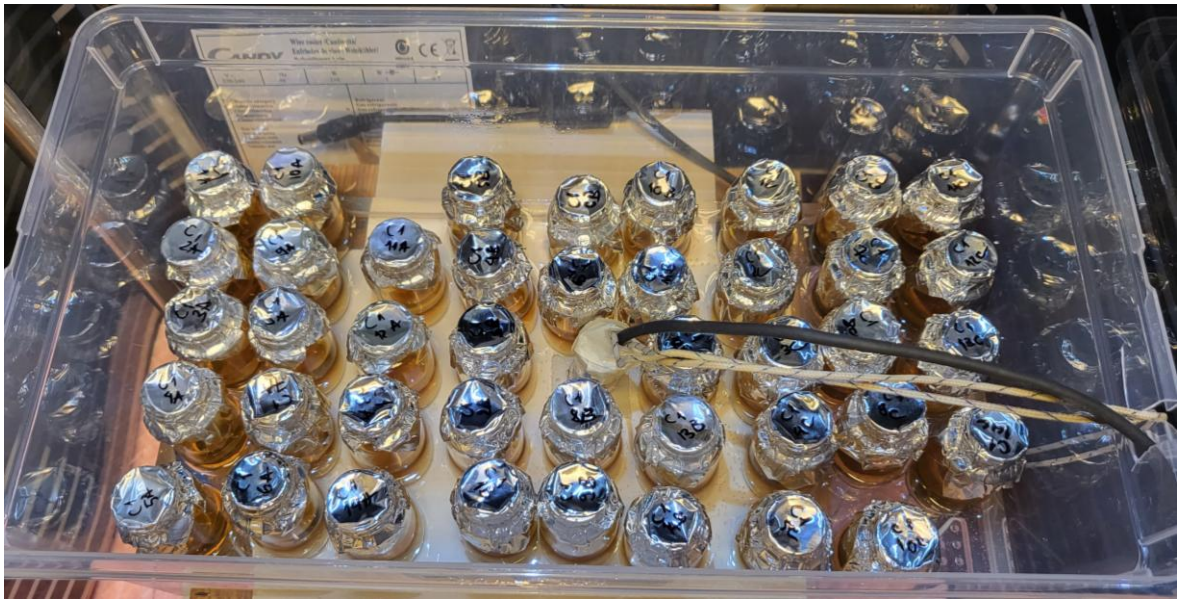

Fig. A11: Large-scale cultivation experiment with 84 sealed vials of yeast culture fully submerged in a temperature-controlled water bath. The setup ensured uniform thermal conditions across all samples to support consistent growth and reduce variability during experimental modelling of optimal cultivation duration.

Appendix F – Supplement Programing Codes

Programing code for Helmholtz Coil Modeling Matlab Code Temperature Monitor Ardruino Code are available on open public repository:
https://github.com/Sometimeic13/PhD.